UNIVERSITY OF CALIFORNIA SAN DIEGO

Physics and rate dependence of impact energy absorbing bistable mechanical metamaterials

A dissertation submitted in partial satisfaction of the
requirements for the degree
Doctor of Philosophy

in

Engineering Sciences (Aerospace Engineering)

by

Ryan Dean Fancher

Committee in charge:

Professor Nicholas Boechler, Chair
Professor Michael Frazier
Professor James Friend
Professor Alicia Kim
Professor Vitali Nesterenko

2022

The dissertation of Ryan Dean Fancher is approved, and it is acceptable in quality and form for publication on microfilm, and electronically.

University of California San Diego

2022

TABLE OF CONTENTS

LIST OF FIGURES

LIST OF TABLES

ACKNOWLEDGEMENTS

When I embarked upon this challenge approximately three years ago, I was rather naïve to what in many instances would later feel like an impossible task, particularly given the time constraints I was held to. I owe a good deal of gratitude to the individuals listed below for their help and encouragement through this challenging process.

To my family: your steadfast support has never wavered throughout my life, regardless of circumstance, time, or location– for this I am truly blessed.

To my best friend Will, for the last two decades I've always had a trusted friend to bounce ideas off of. I probably bent your ear more over the last three years than I have for quite some time, and you always took that in stride. Thanks.

To my graduate school colleagues, particularly Ian Frankel and Brianna Macnider, it's rather difficult for me to envision being successful, particularly through my first year of graduate courses, without the hundreds of hours cumulatively spent with each of you. I'm sincerely thankful both for your willingness to teach, and to learn alongside me—from the very first day of classes until today. Thank you.

To my Doctoral Committee, thanks for your support, flexibility in scheduling, and willingness to impart your wisdom on challenging topics.

To Prof. Nick Boechler, thanks for your willingness, patience, dedication, and optimism in agreeing to take on a (semi) crusty former fighter pilot for this challenging task. Your passion for teaching and research is obvious, and I've learned a ton as a result of your methods. Thanks.

Finally, to my employer, the US Air Force: thanks for the opportunity to go back to school and learn a new discipline. There are a rare few Air Force Officers in San Diego, and I was lucky enough to be one of them for three years.

Disclaimer: The views expressed in this dissertation are those of the author and do not reflect the official policy or position of the United States Air Force, Department of Defense, or the U.S. Government.

VITA

2006	B. S. in Aeronautical Engineering, *Distinguished Graduate*, United States Air Force Academy
2013	Master of Business Administration, Oklahoma State University
2016	Class A Experimental Test Pilot School Graduate, Number 75 Fixed Wing Course, Empire Test Pilots' School, Boscombe Down, UK
2021	Candidate in Philosophy in Engineering Sciences (Aerospace Engineering), University of California San Diego

ABSTRACT OF THE DISSERTATION

Physics and rate dependence of impact energy absorbing bistable mechanical metamaterials

by

Ryan Dean Fancher
Doctor of Philosophy in Engineering Sciences (Aerospace Engineering)
University of California San Diego, 2022
Professor Nicholas Boechler, Chair

Mechanical impact, long studied, has the power to be harnessed for the positive benefit of society, but clearly can also result in unwanted destruction. Despite centuries of study, there is still much to be learned, particularly as a result of novel materials requiring rigorous analysis to understand both strengths and shortfalls. Metamaterials are a class of material where generally abnormal properties are realized primarily as a result of their internal structure. The study herein focuses on the analysis of a particular mechanical metamaterial design, in which individual "unit cells" making up the broader material exhibit two stable states at zero force on a force versus displacement curve. These "bistable mechanical metamaterials" have received attention due to their ability to elastically "trap" energy, provid-

ing an additional and potentially complementary mechanism to more traditional processes to abate energy transmission. The author, through simulation and experiment, analyzed kinetic energy (KE) transmission after impact in a particular bistable mechanical structure, which was compared to the KE transmission of a control material, in order to assess performance. The analysis assumed operation within: the elastic regime, with sample strain rates less than 10^2 s^{-1} and no plastic effects; "wave-dominated" regimes, wherein the dominant wavelength of the impact pulse is smaller than the overall tested sample size; and regimes where continuum approximations are appropriate, such that the dominant wavelength is larger than the individual unit cell size. Nominal impactor conditions (mass and velocity), hypothesized to result in good performance were estimated, then the sample was subjected to multiple combinations of, primarily simulated, impactor mass and velocity to observe performance differences. Similar trials were conducted with varied unit cell size (in a finite sample size), damping, and unit cell constitutive response. The following novel points were discovered. Performance of the bistable mechanical metamaterial is highly dependent upon the: 1) impact conditions (both impactor mass and velocity), 2) amount of material damping, and 3) number of unit cells within a finite sample size. Additionally, it was observed that alteration of the force versus displacement curve (modeled as a continuous polynomial function) such that the post-buckled stiffness was less than the pre-buckled stiffness improved the maximum performance of this system further, as expected based on prior literature results. These key results, and others herein, represent a small advancement that provides further insight to the suitability and further design of bistable mechanical metamaterials for impact.

Chapter 1

Introduction

The local magnification of mechanical forces as a result of a dynamic collision (impact) has been known since ancient times [1]. Some of the first human tools harnessed this power in the form of hand axes to intentionally break objects [1], while energy transmitted as a result of mechanical impact can clearly also result in unwanted destruction. In either case, there is a compelling motivation for such phenomenon to be understood [2–4]. Impact physics has been studied for at least three centuries by scientists like Newton and Poisson, and with continued study thereafter [3–18].

Despite centuries of study within the field, there is still much to be learned, particularly as a result of novel materials and structures which continue to propel the field forward, thus requiring continually updated analysis and modeling. Benefits of this research are varied and ubiquitous, and include improved packaging to prevent damage during shipment [19], personal protection equipment for civilian and military application [2, 19, 20], crash mitigation for vehicles [19, 21, 22], and design of improved tools and sport equipment [23, 24]. For instance, in tools that experience regular impact it is necessary to determine a working velocity limit in order for these tools to be built with the necessary durability for long term and repeated use [23]. The improvement of sports equipment requires an understanding of the anticipated bounce direction, speed, and spin for items such as a tennis ball, baseball, or soccer ball after impact [24]. Unfortunately, automobiles, ships, and military a law enforcement personnel and equipment experience

impact from collisions which occur during their operations, and thus investigating the effects of collisions with objects of different masses, velocities, and materials is relevant [25–30]. Speaking within an even broader context, an understanding of hyper-velocity events is relevant for those inclined towards space, and earth dwellers alike. For example, impact cratering of planetary surfaces is widespread – a better understanding of these events ostensibly gives better insight into the shaping of our planet and others in the universe [31]. Additionally (as evidenced by recent impacts to both the international space station and the James Webb Space Telescope), micrometeorite and space debris pose a significant threat to space vehicles and personnel, thus a better understanding of the impact mechanics could lead to better designed equipment as missions to far off destinations such as Mars are planned [31–36]. It is clear that not only is mechanical impact a broad phenomena with a long history of study, but also one that is extremely complex and continually evolving with technological improvement and understanding both in terms of diagnostics and modeling. Therefore continued study of the subject is not only rich, but necessary for the progression of society.

Broadly speaking, impact regimes can be classified as elastic, plastic, and shock [3]. When an impact results in the maximum stress in a material below the yield (or fracture, in the case of brittle materials) stress, we are in the elastic regime. An undamped material impacted within this operating regime will deform according to the elastic constitutive relation of the material, then it will return to the previous state. When this limit is exceeded, we are in the plastic regime or have reached failure due to fracture [3]. A ductile material that enters into this regime via impact will have its yield stress exceeded and thus plastify, and energy will be absorbed (converted to heat) as a result of the permanent plastic deformation. A brittle material may plastify (to a lesser degree than a ductile material) or it may fracture or fragment. In either case, energy will be absorbed or dissipated as a result of these processes. At significantly higher amplitudes than those of the plastic regime, we go into a regime characterized by discontinuities in density, pressure, and temperature (or internal energy) within the material, known as the shock regime, where an "equation of state" approach is used to describe the material

response [3]. This equation of state regime is not studied or accounted for further in this dissertation. All of these cases will also be affected by viscous processes, which will remove additional energy from the material with each loading cycle in the form of heat [37].

The assumptions for the modeling and simulation in this work assume operation within the elastic regime, although damping is accounted for as a result of viscoelastic processes. The elastic regime of interest for the tests herein can be further quantified by strain rate, where the sample strain rate range is estimated to be less than 10^2 s^{-1}, which places this testing in the "dynamic-low" range in Meyers' classification [3]. This strain rate estimate was determined by calculating the displacement of top layer at approximately the maximum displacement after impact (for nominal impact conditions), then dividing this by the time from impact in order to get a strain rate estimate for the sample. It is important to note that due to the wavelike behavior studied herein there would be different strain values locally, at the unit cell level, and also at the material level (e.g. the material composing a given piece of the unit cell). The simulations do not account for any strain rate sensitivity of the constitutive material, although within this regime, the effect was not expected to significantly affect the results [3, 38, 39]. It is important to note that this methodology (only analyzing the elastic effects in simulation) is likely conservative, since, for instance, plastic effects would result in the dissipation of additional energy, thus improving impact mitigation performance above the predictions given in this work [3], and potentially mitigate any re-release of energy stored in a given bistable unit cell.

Within the context of impact, some of the most well known mechanisms of energy absorption include plastic deformation, fracture, fragmentation, viscous processes, and scattering. [2, 37, 40–42]. Notably, aside from viscous processes (which result in energy loss during an otherwise elastic loading cycle) and scattering, an impact resulting in stress below yield throughout the material (which is likely to occur within the "dynamic low" regime) will not dissipate energy through the other mechanisms listed above [3, 37]. Thus, there is significant motivation for an additional mechanism(s). Another approach to attenuating waves resulting from im-

pact is scattering, which can include concepts such as disordered materials [42–46], phononic crystals [47–49], and locally-resonant metamaterials [48, 49, 49, 50]. However these strategies rely on reflection of incident waves, which may present challenges for impact mitigation specific applications within the context of momentum conservation. Furthermore, in the case of phononic crystals and locally resonant metamaterials, while progress has been made in this area, the strategy typically targets narrow-band excitations, rather than the broadband frequency content induced by impact [48, 51].

An alternative strategy is the use of bi- or multistable structures, which have the potential to "trap" elastic strain energy, and thus prevent unwanted transmission after an impact, for instance, all while operating within the elastic regime of the constituent material [19, 52]. This concept will be introduced further, but the key point is that it is one of the few processes where elastic strain energy can be trapped, and later released in a controlled, non-destructive fashion, that's also functional within the elastic regime. Additionally, and perhaps even more exciting, is the potential for this mechanism to be used beyond the elastic regime as well, thus achieving an additive mechanism for impact mitigation even when operating within regimes where plastic deformation, fracture, and fragmentation are experienced. Furthermore, the author's research to date indicates optimal benefit from the bistable mechanism occurs at lower material loss coefficients than is typically seen with traditional viscoelastic materials (e.g. rubber, foams, and soft polymers), thus potentially offering a new and exciting additional impact mitigation strategy for lower loss angle constitutive materials like metals and high Young's Modulus polymers, where impact mitigation due to damping is inaccessible [37].

To further introduce the concept, we will discuss the idea of impact mitigation "systems", and composites, inspired in part by observation of biological systems. Within this context, let's start from the idea of mitigating an impact as a result of a projectile striking a protective material designed to stop the energy from transferring to any objects below it. One common method to do this (as stated by Meyers when discussing armor applications), "is to break the projectile with a very hard surface, and then absorb the energy of projectile and/or armor fragments by

using a soft, ductile backing material" [3]. From this statement, it is important to note the specific roles which generally dictate the use of multiple materials; a very hard material that's useful for the breaking of a projectile, then an ostensibly different, soft material that's useful in order to absorb the energy prior to the location where it meets the surface which is designed to be protected [3, 30]. To explain this a slightly different way, I'll use the example of a motorcycle helmet. Typically, this helmet is made of at least two separate parts; a stiff external shell, then a softer inner layer [53]. In a crash, the stiff outer shell mitigates concentrated loads at the point of impact (thus reducing the chance of penetration), and also dissipates impact energy as a result of shell deformation [53]. The softer inner foam layer is then designed to reduce the loading and energy (which may propagate in the forms of waves), that is transmitted to the head to a minimum [53]. Thus in both examples presented above, the impact is mitigated by a "system" of sorts, with one part of the system primarily designed to mitigate the concentration of force and potential for penetration, and the other designed to minimize the amount of damaging energy reaching the target of protection. In a similar manner, one likely use case for the material of this dissertation is a replacement for the softer backing material in a similar two part system. This, in addition to the fact that it simplified the modeling, and that these mechanisms are generally not present during elastic loading, is further reason my research did not focus on penetration, fracture, or fragmentation. Rather, the chosen goal was to minimize the kinetic energy transmitted through the material. This metric is convenient because it is easily measured both in simulation and also in high speed camera experiments, and because kinetic energy transmission is known to be closely related/causal to damaging effects [30,54]. For instance, the amount of kinetic energy transmitted to a person after bullet impact is highly correlated to known trauma, specifically due to behind armor blunt trauma (BABT), which is the result of both compression rate and total compression of internal organs, and prevalent even in cases where a bullet does not penetrate through the protective body armor being worn [30, 54]. It is noteworthy that choosing other metrics could provide additional insight. For instance, choosing peak pressure at a particular area of interest could be a useful

metric to understand how close the absorbing material was to failure (e.g. fracture or yielding) [55, 56]. Additionally, propagating stress waves at tissue boundaries after impacts in animal models showed that localized pressure peaks as a result of reflection and refraction of said stress waves were associated with more severe injury [57]. Separately, differing the impact pulse shape can greatly affect the resulting maximum strain rate, and therefor a study concerning this metric could also be relevant [58]. Thus, while KE was rationally chosen as the metric for this study, there are many opportunities for future work focusing on other metrics.

The biological world uses a similar system-based method for dealing with impact, such as in the case of bighorn sheep and mantis shrimp [56, 59, 60]. For instance, the shrimp's telson, a natural piece of abdominal armor, is able to withstand repeated hammer like impacts from adversaries, and dissipates close to seventy percent of the impact energy from a strike [59]. The big horn sheep's rigid, tapered, spiral horns in combination with an inner filling of a foam-like material have been found to reduce impact energy and brain cavity accelerations, which ostensibly mitigates injury to the animal as a result of frequent collisions with other sheep [60]. In both cases, a multi-material system is used to achieve results, and this biological inspiration is one such motivation for the use of composite materials; a class of material where often there's an intersection between design, function, and material selection [61, 62]. This class of material is made of more than one base material, and a key feature is that the individual base materials retain their own structures and properties, rather than combining into one, as occurs in alloys, for instance [63]. Among other benefits, the study and proper use of such materials allows for previously mutually exclusive properties to be realized—for instance; high strength, high stiffness, high fracture toughness, and high damping [62].

Metamaterials are a class of material that can be considered as a subset of composites, where specifically, an abnormal property can be attained due to the optimization of the material's internal structure rather than material composition [64, 64–66]. In other words, the geometry of the unit cell drives the bulk response, rather than the combinations of constitutive materials themselves [64, 66]. As highlighted by Kadic *et al.* in a recent review article, there isn't a definition

or specific classification of metamaterials consistently used [66]. Thus, the author's definition is adopted from Kadic's definition [66], described below, and it also encompasses other works on metamaterials described herein [56, 66–69]. This definition is that a metamaterial is a specific type of composite structure made of tailored building blocks which are deliberately and rationally designed in order to yield a particular response that is generally beyond the response understood to be possible of the constitutive material(s) alone [66]. It is also more suited to task than the response if the material(s) were/was combined in some random fashion, such as the case for construction of random foams, patterned materials, or mixtures [66]. Another way to think of this distinction of from the concept of "inverse design", where particular properties are sought, and from this requirement a microstructure is conceived [66]. This is distinctly different from analyzing a microstructure, calculating its properties, then using the analysis for the determination of suitability. Additionally, as Kadic *et al.* notes, the "bulk materials" used for the building blocks of metamaterials are made of millions of atoms or more and the individual atomic complexity is not generally considered to any large extent; thus making metamaterials distinct from ordinary crystals [66]. While this chosen distinction of metamaterials largely excludes the molecular and atomic scale, current research in the field does focus on so called "crystalline metamaterials" which does and will continue to blur this line [70, 71].

With this working definition of a metamaterial, further categorization is useful based on the general properties they are designed to alter: first, those metamaterials focused towards the electromagnetism spectrum [72]. Second, those metamaterials focused towards the acoustic and mechanical, and third, those focused towards transport [66]. Possible design goals of electromagnetic metamaterials include; the non-reciprocal propagation of electromagnetic waves, the design of an optical lens to overcome previously understood diffraction limits, or the pursuit of perfect absorbers that permit no light transmission or reflection [66]. Possible design aims of transport metamaterials include anisotropic thermal conductance, and enhanced thermoelectric power factors [66]. Both of these classes (electromagnetic and transport) are beyond the scope of this dissertation, and will not be discussed further.

The remaining category of acoustic and mechanical metamaterials however, is of great importance. Generally speaking, acoustic metamaterials are designed with the primary goal of manipulating sound waves in some way that is desirable to the designer. For instance, an acoustic metamaterial could be designed for unique properties regarding isolation, transmission, or storage of sound, and could for example be used for applications such as the soundproofing of a room [73, 74]. Similarly, mechanical metamaterials are often designed with the goal of manipulating mechanical properties in some way, such as the achievement of nonlinear material response using only linear elastic constituent materials [65, 75, 76]. These two concepts are closely linked, however. For instance, it is well known that the alteration of the stiffness of a mechanical metamaterial lattice would subsequently result in the alteration of the sound speed of the lattice. Similarly, metamaterials with negative stiffness can break a compression pulse without dissipation [77]. Thus the singular categorization for acoustic and mechanical metamaterials is appropriate for my currently intended study where the unit cell building block of the metamaterial is initially designed for bistability under quasi-static loading, but is then analysed under dynamic loading conditions.

With this background on metamaterials and their applicability to my research, I will now focus specifically on the history of acoustic and mechanical metamaterials designed for impact mitigation [78–80]. Of note, some of the source material used below may be classified by their authors' as "architected" or "cellular" materials, although for the purposes of this research they will be broadly considered "metamaterials". We further classify metamaterials for impact as either fully recoverable (single use), or re-usable. Specifically, reusable structures must have a fully recoverable mechanism of deformation, while single use structures generally take advantage of some sort of plastic deformation, and thus are not fully recoverable. Within the fully recoverable category for metamaterials we have the following: buckling, bistability, multistable structures, phononic crystals, and locally resonant acoustic metamaterials. Since bi- and multistable structures are the focus of my research, these are discussed in a later paragraph, and thus buckling and phononic crystals/locally resonant acoustic metamaterials are the remaining cate-

gories noted by the author for re-usable energy trapping metamaterials. Phononic crystals can attenuate energy, although their band gap is generally proportional to the lattice constant, and thus they are limited in their ability to attenuate broadband energy, and are difficult to size for smaller applications [47–49]. While locally resonant acoustic metamaterials are able to effectively attenuate at wavelengths less than their lattice size, they typically have a narrow band gap, or require layering (mass intensive) in order to widen the gap [81, 82]. Additionally, both of these strategies fundamentally rely on the reflection of incident energy, rather than its absorption. For these reasons, the use of phononic crystals or local resonant acoustic metamaterials for broadband impact absorption was not further explored in this work.

Within the buckling category, we have micro- and nanofabricated materials which take advantage of "bending-dominated mechanical behavior" [83, 84]. This behavior is promoted by designing with very low thickness ratios in order to achieve buckling prior to fracture, resulting in a structure that has energy absorption and low density [83, 84]. One notable instance was through the use of a three-dimensional octet-truss unit celled ceramic nanolattices, where an elastic response is seen as long as the nanolattice is dimensioned appropriately [83]. In another case, a nickle microlattice is constructed from an octahedral type geometry, where the energy loss coefficient as a result of a cycle of loading is shown to be an order of magnitude higher than a nickel foam [84–86]. This work is further characterized in order to model and manufacture lattices with a wide range of densities [87]. Within the single use category, there are far more examples, and there's also overlap with the previous category. For instance, when the lattices mentioned above are dimensioned differently (such as increasing the thickness to diameter ratio of truss elements within the metamaterial), larger amounts of non-recoverable deformation, but also a larger amount of energy trapping are observed [84, 85, 87]. Several examples are as follows. Mieszala *et al.* experimented with numerous metal and polymer hybrid structures and showed that they could achieve a higher energy absorption density than aluminum or polyethylene foam [88]. Lai *et al.* used ultrathin polymeric microlattices which showed high energy absorption capability

as a result of sideways buckling of the microlattices during the crushing stage of the impact, although, again, plastic deformation and fracture was occurring during the process [89]. Scaedler *et al.*, in their review article, discussed other similar examples of irreversible energy trapping using solid aluminum microlattices with an octahedral structure, thermoplastic polyurethane twin hemispheres, and hollow nickel microlattices with vertical posts, among others [56]. With inspiration from the hierarchical structure of some natural building blocks, Meza *et al.* produced structures fashioned from octet geometry and constructed in a fractal manner, and built from either polymer, hollow ceramic, or ceramic-polymer composite [90]. Depending on the material choice, these structures recovered up to 98% of their original height (although in the cases with high recovery percentages, significantly less energy was dissipated in the second cycle in comparison to the first cycle), thus while beyond-elastic region effects were seen in all cases, this example could be placed in either category [90]. Thus, excluding bi- and multistable materials, within the metamaterials for energy absorption category, while there are more options for single-use applications, there are very few when it comes to fully recoverable energy absorbers, which leaves the field ripe for the further exploration of novel ideas. Furthermore, it remains to be seen the relative performance between a buckling-based strategy and a multistable energy-trapping impact mitigation strategy.

In parallel to the concepts discussed above, instabilities have long been studied for their rich properties, including negative stiffness, unique dynamics, wrinkles in nature, energy trapping potential, and deployable structures, among other features and phenomenon [91–93]. Mechanical bistability, one particular type of instability, involves two stable states at zero force (as shown on a force versus displacement curve). One example of this system, seen in nature, is the Venus flytrap, which uses a snap-buckling instability to achieve the highest closure speed of all plants, allowing it to close in approximately 100 ms [94,95]. For a more detailed look at the analysis of bistable phenomena, we'll discuss some past works where theoretical, numerical, and experimental results have been presented. Previous quasi-static analysis included the study of two stable states of a curved beam under transverse loading [96], the force versus displacement and corresponding stability landscape

of an elastic two bar truss (Ref. [97] and references therein), an analysis in the context of bistable cylindrical shells [98], and bistable auxetics inspired from ancient motifs [99]. Other studies have focused on the dynamics of bistable structures, including the Venus flytrap (previously mentioned) [94]. But also, the bistable dynamics of a snapping beam or jumping popper [100], and the analysis of the snap through of a thin polymer strip loaded by the mass of a water droplet [101]. Additionally, bistable mechanisms, inspired by nature, have been used for soft robotics propulsion [102]. Other studies have explored the snap-through and transition wave analysis of periodic materials containing bistable elements. For instance, the wave dynamics of a bistable element moving from one potential energy well to another was explored, which showcased a robust capability to propagate a "transition wave" through a highly dissipative material [103]. This and other studies also showcased the tunability of the wave in velocity and direction in both 1D [19, 103] and 3D lattices [52]. Yet other examples feature bi- or multistable designs as a result of stacked origami geometries, with noted potential for wave propagation control [104]. All of this information is useful for a broad understanding of bistable metamaterials. However, these examples regarding bi- and multistable metamaterials have not yet focused specifically on impact mitigation.

Bringing the concepts of dynamic collision, impact mitigation, composite materials, metamaterials, and mechanical instability/bistability together, I define my research area to the study of impact, within the regime considered both "dynamic low" and wave-dominated, using bistable metamaterials. Previously mentioned, but expanded upon here, I'll define a wave-dominated regime as a regime where the dominant impact wavelength is smaller than the overall sample size (if we were to Fourier transform the impact pulse, the dominant wavelength would be the largest amplitude wavelength). We note to maintain a continuum description, the dominant wavelength is simultaneously much larger than the unit cell size. To give an example of why both the strain rate regime of "dynamic low" and the definition of a wave dominated regime are important, let's consider an impact into very small sample in comparison to the dominant impact wavelength. In this case, even if a strain rate sufficient for the dynamic low range is achieved, the test is not within

a wave dominated regime, and is instead effectively quasi-static because the long dominant wavelength of impact effectively communicates its information to the top and bottom of the sample on a very similar timescale. Thus both factors; appropriate strain rate, and dominant wavelength to both unit cell and sample size ratio are necessary for the defined regime of my research. To quantify this idea further, three ratios were used, where $R_L = V/c_0$, $R_C = \tau c_0/a$ and $R_W = H_S/\tau c_0$, where τ is temporal impact pulse duration, c_0 is the lattice linear sound speed estimate, V is chosen impactor velocity, a is the lattice constant, and H_S is the total lattice (or sample) length. By these metrics, R_L gives a dimensionless estimate for the impact rate in relation to the linear soundspeed of the material, R_C gives an indication of whether the unit cell is "seen" as a continuum, and R_W gives an indication as to whether the impact can be characterized in a wavelike regime. Higher values for all ratios represent higher rate, more like a continuum, and more wavelike regime, respectively. Ratio R_C values for the author's work ranged from approximately 1.3 to 12.7, R_W values ranged from approximately 7.9 to 75, and R_L maximum values were ≈ 1.2 for experiment and ≈ 1.5 for simulation. As one point of comparison, the highest R_C and R_W values estimated in the Shan *et al.* work (for which the author's unit cell design was inspired) were $R_C = 4$ and $R_W = 1$ [19]. Ratio R_L comparison values are included in the next paragraph.

Given this narrow context (*i.e.* impact mitigation using bistable metamaterials, but not necessarily in the same strain rate or wave dominated regime), several examples are highlighted for their relevance in the following. Shan *et al.* demonstrated trapping of elastic strain energy using architected materials containing bistable beam elements [19]. They stated that energy absorption through this method stemmed solely from structural geometry of the printed beam elements and was thus loading-rate independent, although their force displacement testing was at a low rate (ranging from $R_L \approx 1e-5$ to $1e-3$) and their drop testing covered only a very narrow range of impact velocities (ranging from $R_L \approx 0.2$ to 0.3) [19]. Zembiloren and Gurses analyzed beam parameter changes (tilt angle, width/length ratio, beam shape changes) and showed the effects in terms of predicted energy trapping capability in a bistable system, but this quasi-static study

did not address rate dependence [105]. Frenzel *et al.* expanded upon the Shan *et al.* work and produced a smaller 3D lattice with lower relative density, tailorable spring stiffness, and analysis for both bistable and negative stiffness elements without bistability, although their experimentation was only shown for self recovering samples (i.e minimum force > 0), and their maximum loading rates were also low ($R_L \approx 1e-7$ to $1e-3$) [52] . Ha and Plesha *et al.* produced a multi-stable lattice design using a different type of bistable unit cell, but again their maximum impact velocity was slow and narrowly ranged ($R_L \approx 0.09$ to 0.15) [106]. Wu and Zhou *et al.* added a "snap-fit" mechanism in which a plug is designed to be inserted into a corresponding groove as an additional mechanism to achieve and tune their bi-stable unit cell design, although again this was tested at very low loading rates in comparison to the estimated lattice sound speed ($R_L \approx 2e-3$ to $5e-3$) [21]. Katz and Givli conducted an investigation of wave propagation in bistable springs resulting from tri-linear piece-wise functions and indicated through numerical simulation and theory that the prediction of solitary wave propagation (and thus high energy transmission through the material) or oscillatory behavior inhibiting transmission could be linked to the relationship between the pre and post buckled stiffness of the spring- however they did not address rate dependence or conduct experimental studies [107, 108]. Yasuda *et al.* took the tri-linear piece-wise idea in a different direction, using a similar bistable chain and altering impact velocities in order to better understand trapping behaviors, although they did not complete experimental work, and they did not consider a smooth (i.e non-piece-wise) function in their analysis [109].

Thus, the testing of bistable and multi-stable metamaterials has some history, although to date, nothing has rigorously focused on the testing of said materials at higher loading rate divided by lattice sound-speed ratios, and also specifically investigating the link between material performance and the mass and velocity of the impactor impacting the structure. Since this is a goal of this research, and in order to scope the problem even more narrowly, we'll consider impact loading to be the case when a previously propelled but now free-falling object strikes a surface. One such scenario in text describing a similar phenomenon is that of a very

simple impact scenario; a bar hitting a collar and changing the energy landscape, where kinetic energy is transferred into strain energy into the bar [5]. We will also only focus on "conformal contact" (i.e the area of the impactor is similar in dimension to the surface being impacted), rather than point contact [12]. In this manner, the author intends to walk the reader specifically through the benefits and drawbacks resulting largely from the elastic strain energy trapping capabilities of the chosen geometry of bistable metamaterials as a result of changing loading conditions (impactor mass and velocity). Additionally, during the pursuit of a better understanding of the influence of loading conditions on performance, a great deal of additional information was learned in terms of the influence of solitary wave propagation, damping, unit cell sizing, and post buckled stiffness of the bistable unit cell on performance– these results will also be presented.

In prior studies on impact mitigation with bistable materials and the research described in this work, a key mechanism that contributed to poor performance was solitary wave propagation [107–109]. Thus some background on solitary waves and their influence is necessary. A solitary wave is a type of spatially localized nonlinear wave with unusual stability properties, in that there is a trade-off between dispersion and nonlinearity such that the shape and velocity of the wave is preserved as it moves, and has an amplitude dependent wavespeed [110–112]. A solitary wave which has the additional property of retaining the same permanent structure after interaction with another solitary wave of the same property is called a "soliton" [113]. The author notes that while bistable structures have been shown to support solitons [114], this distinction is not specifically investigated in this work. In bistable structures, if an initial energy barrier is overcome in order to move the structure from its higher energy stable state to a lower one, a "transition wave" is formed, which has been demonstrated to allow for wave propagation over long distances [103, 115, 116].

Regarding impact and solitary waves specifically, a few areas of research have included wave tunability within spherical or granular particles [8, 117, 118], wave propagation through a chain of pre-stressed tensegrity prisms [119], and wave propagation through bistable chains [107–109]. As a result, it was understood

that manipulation of microstructure can result in vastly different solitary wave responses; for instance, the careful manipulation of a granular chain can change a single impulse into a series of smaller impulses– ostensibly useful to minimizing a large bolus of energy from crossing a threshold location [8]. However, solitary wave phenomenon are also well known for their self-focusing abilities, ostensibly detrimental to the minimization of a bolus of energy crossing a particular location threshold [111].

Within the context of solitary waves in bistable systems for impact mitigation, one particular case from literature produced a theoretical and numerical analysis to link the stiffness ratio of elements between their pre and post-buckled states as a major predictor of solitary wave propagation [107] by using a tri-linear piecewise function to represent the relationship. These numerical studies with stiffer postbuckled springs propagated solitary waves which transmitted high densities of energy throughout the simulated sample. But by changing to a spring design where the post-buckled spring was softer than the pre-buckled spring, a large portion of the impact energy was trapped in oscillations in the earlier layers, leaving little transmission across the sample [107]. With this study as an inspiration, a polynomial, continuous constitutive function was developed and simulated, which resulted in additional performance benefit. This still leaves for future work the development of a physical bistable unit cell design that would possess a softer post buckled stiffness for experimental trials.

To outline what I will discuss, here is a brief sketch of the topics and their order: 1. The modeling approach, covering the development of the constitutive relationship, unit cell sizing and design, choice of appropriate initial impact conditions, and dynamic modeling of the impact. 2. The simulated material performance in comparison to a material with a linear constitutive response over a broad range of impactor conditions, in cases without damping being modeled, and also cases using intersite linear damping. 3. The simulated performance effects and qualitative differences resulting from increasing the number of unit cells for a given sample size. 4. A full description of the analytical framework for the determination of damping, both for the purposes of simulation, and also for the determination of

real materials best suited for impact absorption in bistable metamaterials. 5. The simulated effect of altering the post buckled stiffness of the force displacement curve on the dynamic performance of the lattice. 6. A background on the choice of using kinetic energy (KE) density as the comparative metric for the dissertation. 7. The results of the physical experimentation done to date. 8. Ideas for future improvement of the bistable design. 9. Recommendations for future work.

Chapter 2

Design and modeling approach

The basic experimental and simulation setup herein is the impact of a relatively rigid "impactor" block onto an arbitrarily-sized, designed "absorbing" block of material, as is shown in Figure 2.1. The chosen absolute dimensions of the sample were 10 cm height by 5 cm width by 5 cm depth. They are also labeled $H_s = 2d$ (height) by d (width) by d (depth). Our designed absorbing material consists of a bistable mechanical metamaterial composed of a periodic array of structured unit cells. The kinetic energy transmitted through the half way point (with respect to the impactor velocity vector) of the absorbing block was chosen as the performance metric (discussed in detail in section 8). This transmitted kinetic energy through the designed absorbing material was then compared against that of a "control" absorbing material.

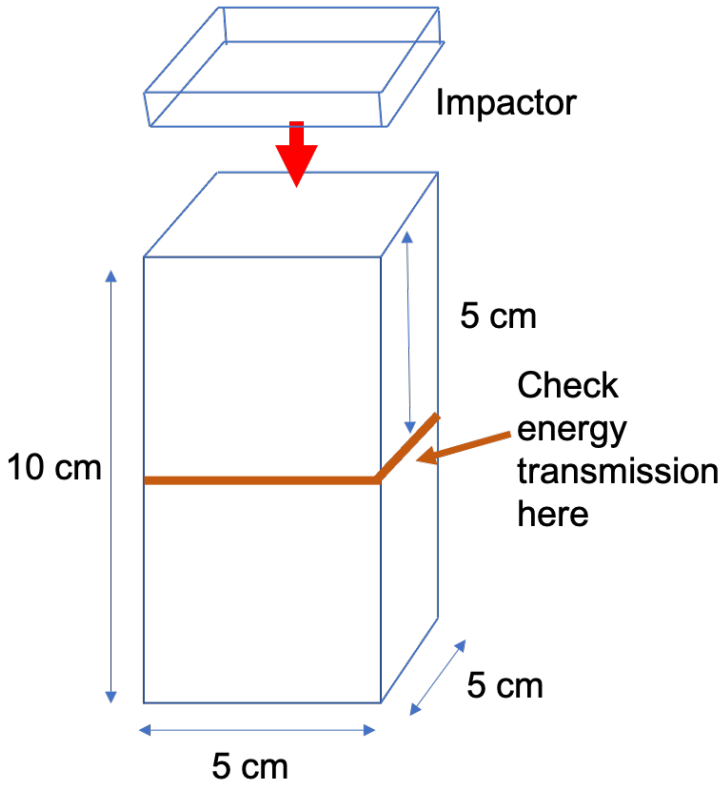

Figure 2.1: The location to determine kinetic energy transmission was at the half-point of the sample in the direction of the impactor velocity vector.

The research of Shan *et al.* [19] was used for inspiration for initial unit cell design of our bistable mechanical metamaterial, however in our case, we sought to focus on modeling and experimental testing at higher rates. As such, a unit cell was designed (shown in Fig. 2.2), composed of two elastic beams connected to a structurally stiffer frame not designed to buckle (called the "monolithic" portion). This design was tessellated in order to produce a lattice from these unit cells. Particular care was taken with the design choice of the thickness to length $r = T/L$ aspect ratio of the beam (where T is the beam thickness and L is its length), as well as the angle of the beam θ (shown in Fig. 2.2). The remaining variables: $L_1, W_2, W_1, d, L_3, W_3$ and L_2 describe the additional geometric features of the unit cell, and are further discussed in Sec. 2.5. Shan *et al.* calculated the magnitude of the energy locked under quasi-static compression as a result of bistability as a function of changes in T/L ratio and beam angle through FEM analysis [19]. This

data was confirmed using FEM, then used for the initial choice of beam aspect ratio and angle.

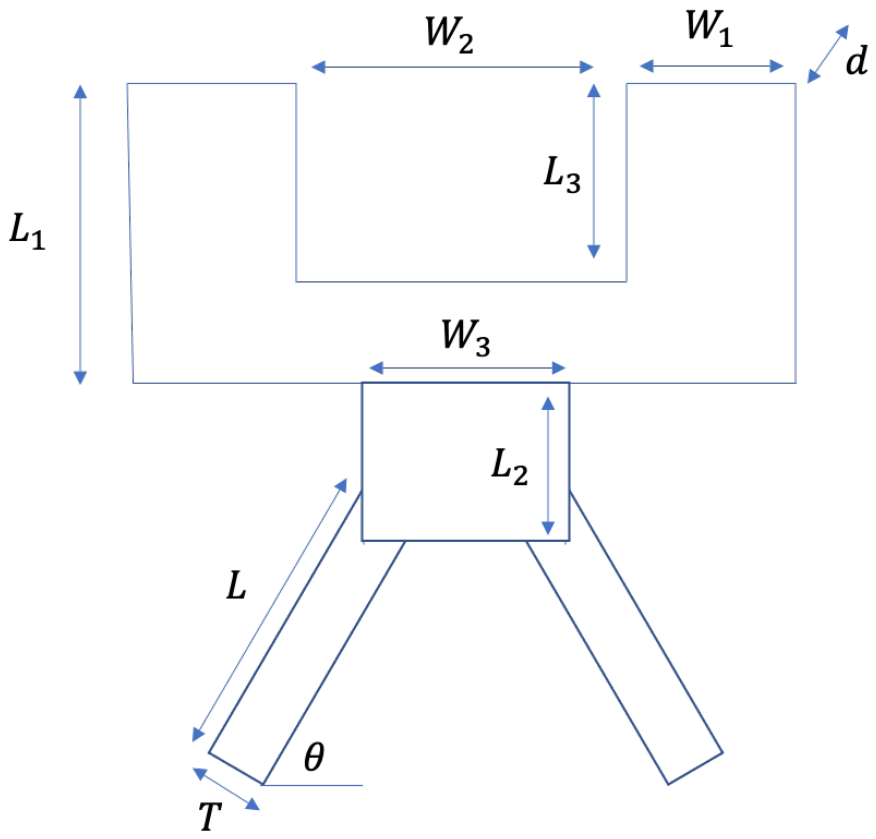

Figure 2.2: Sketch of the unit cell design for the bistable mechanical metamaterial, with the variables used to define the dimensions of the unit cell. For this work, $r = 0.14$, where $r = T/L$ is the thickness over length ratio of the beam, and $\theta = 60$ degrees.

The following describes the process for unit cell design. While previous research stated the energy locking phenomena due to bistability was rate independent [19], the author hypothesized that it was not. Based on this hypothesis, the focus was not on maximizing a quasi-static energy trapping value, but rather to construct a unit cell design for analysis at different rates in order to observe the performance changes as a result of different impactor rate (and mass). Thus the author did not select a value for maximum quasi-static energy locking necessarily anticipating this choice would result in the maximum performance in a dynamic setting. Instead,

a design choice was initially made based on FEM simulations that weighed the following trade-offs with anticipated manufacturing tolerances. Moderately high value of quasi-static energy locking (*i.e.*, steep enough beam angle such that some energy locking is experienced at snap through, and shallow enough that the beam itself doesn't self-contact and prevent energy locking [19]). It was also hypothesized that a choice of r and θ too close to the quasi-static maximum prediction would result in too small of an energy barrier to unsnapping, which could result in the negative consequence of a re-release of energy within wavelike regimes. Thus, $r = 0.14$, and $\theta = 60$ degrees was chosen which resulted in quasi-static bistability both through FEM simulation and experiment with a 3D printed sample. It should be noted that this method leaves room for future study and further optimization.

The rest of the unit cell was subsequently designed to allow sufficient clearance to allow both beams to transition from either stable state without contact-based interference from the monolithic portions of the cell. This was done by dimensioning the unit cell such that the beam was able to buckle at least past its second stable equilibrium point on a force displacement curve prior to the monolithic portions of the tessellated unit cells coming in contact with each other. For instance, Fig. 2.2 shows the unit cell design and labeling of different segments of the unit cell, and Fig. 2.3 shows the strain energy vs. displacement curve for a single, arbitrarily chosen 8 mm length beam used for FEM simulation in COMSOL. A further discussion of boundary conditions, material choice, and material model are included in section 2.2. From Fig. 2.3, the second energy well, $\varepsilon_2 = 0.445$, occurs at approximately 11.1 mm displacement on the blue curve. Per the unit cell design it is assumed that the only portion of the unit cell that will deform significantly is the beam, and thus the vertical displacement for self contact is described by $L_2 + L\sin\theta$. Therefore, L_2 must be dimensioned such that ε_2 is less than the strain in the unit cell at self contact, $\varepsilon_{sc} = 0.563$. This allows the unit cell to achieve bistability before self contact, and the difference between ε_{sc} and ε_2 allows for a small amount of additional manufacturing "pad". While arbitrary dimensions for beam length were used in this example, the behavior is independent of scale if all dimensions retain the same relative magnitude, as described further in section

2.4.

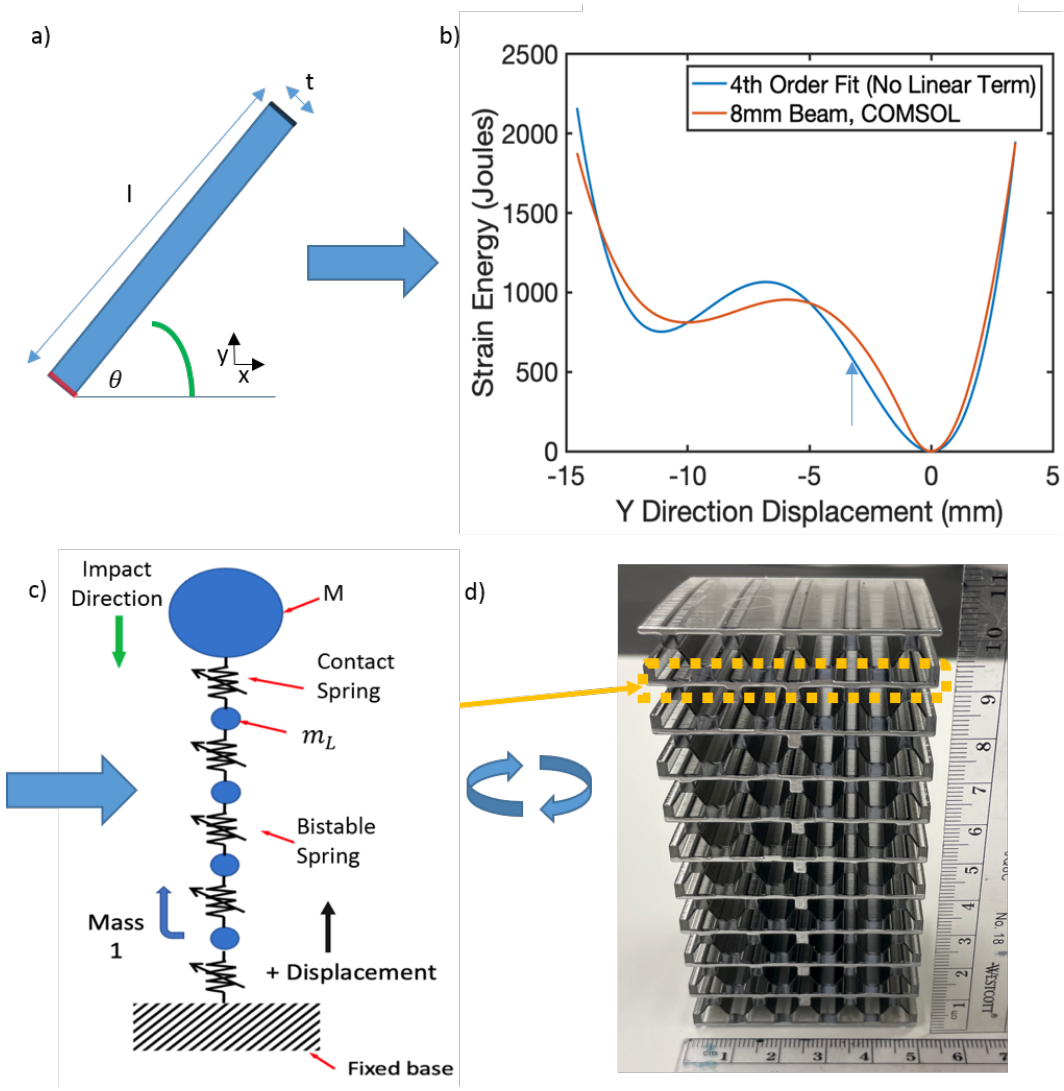

Figure 2.3: (a) Schematic of one beam in the unit cell design. Boundary conditions: red is fixed, black is a prescribed displacement in the negative y-direction only (fixed along the x-direction), and the remaining boundaries are free. (b) Simulated (FEM) strain energy vs. displacement for a single 8 mm long aluminum beam, shown in red, (two beams in each unit cell) and polynomial fourth order curve fit (shown in blue), which is used in the DEM simulations. The strain at the first inflection point is indicated by the blue arrow. The T/L ratio was 0.14 and $\theta = 60$ degrees. c) Illustration of the DEM model, describing the impactor as a mass separated by a nonlinear contact spring, then describing the sample as a series of uniform masses separated by massless nonlinear springs. Positive displacement is defined as upwards, opposite to the impactor initial velocity. Impactor mass M and and layer mass m_L are labeled. d) Printed dual material 50 unit cell (10×5) lattice, used for the impact experiments.

The force (or strain energy) versus displacement curve polynomial fit did not explicitly model a stiffness to account for self contact. For instance, Fig. 2.4 shows the stiffness function derived from the "default" case for a single beam (described further in section 2.2), in blue. The stiffness value estimated at the onset of when self contact was experimentally observed during mechanical testing (from a 10 mm unit cell) is shown in yellow. The estimated theoretical stiffness value at self contact is shown in red for a dual material lattice, and the estimated theoretical stiffness value for a single material lattice is shown in purple. The blue arrow indicates estimated self contact, which occurs at 5.6 mm.

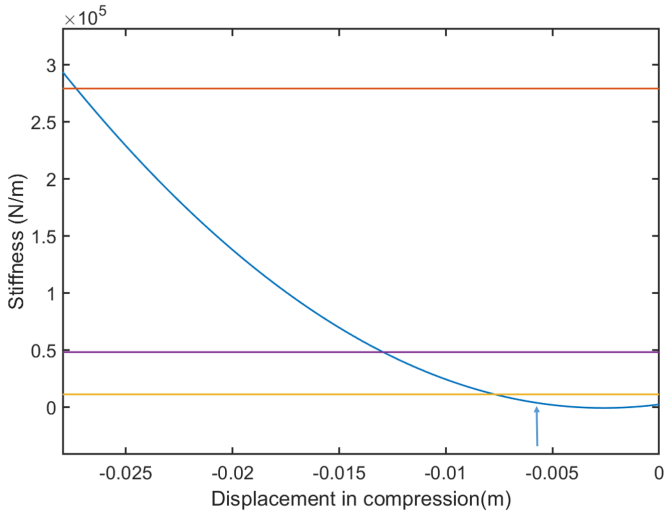

Figure 2.4: Blue color represents the stiffness derived from the "default" case of a single beam. Red shows the estimated theoretical stiffness value for self contact using a unit cell with $\theta = 60$ degrees. The purple shows theoretical stiffness for self contact if the monolithic and beam portions are made of the same material. Yellow shows the estimated stiffness at the onset of self contact from experimental data of the dual material design. The blue arrow indicates estimated self contact, which occurs at 5.6 mm, or $\varepsilon = 0.56$ (unit cell height is 1 cm in this example).

The red stiffness value was estimated using the relationship:

$$K = \frac{WEH_C d}{2(H_C - L_2 - L\sin\theta)}, \tag{2.1}$$

where E is the experimentally measured Young's Modulus of the beam material, H_C is the height of the unit cell which also equalled the width (a square unit cell

assumptions was made), then $H_C - L_2 - L\sin\theta$ represented the height estimate of the unit cell at self contact. The stiffness was increased by a factor of $W = 5.8$, based on an estimate of minimum modulus ratio between the monolithic and beam portion of the unit cell to maintain bistability (described further in subsection 2.3). The purple line was estimated with $W = 1$, representative of a single material lattice design using a beam with $\theta = 40$ degrees, simulated in Sec. 10.1. The results were divided by two in order to model the contact of a half-unit cell in order to compare with the stiffness of a single beam. The yellow line stiffness approximation was from the slope of the force displacement curve just prior to terminating the test as a result of the initial visual observation of self contact (thus one would expect stiffness to continue to increase with further compression). From the data above, it is clear that the stiffness of the polynomial function under represented the stiffness due to self contact, and improvement of this limitation is left for future work.

Further dimensions were chosen as follows. In order to minimize the chances of out-of-plane buckling, the height of the overall sample was set to be only twice the depth (Fig. 2.1). Additionally, an important goal of this research was to focus on a "wave dominated regime", and thus the testing intent was to design such that the impact pulse width was much much less than the sample height. The unit cell height was also chosen to be much much less than the pulse width such that the pulse "sees" the unit cell as a continuum. While it proved difficult to accurately estimate the pulse width of a broadband impact, this constraint favored a very small unit cell, and a very large sample size.

While the relative dimensions of the designed absorbing block of material's unit cell were chosen as described previously, absolute dimensions were chosen based on anticipated available manufacturing and testing resources. For instance, based on discussions with collaborators at the U.S. Army Research Laboratory (ARL), the maximum cross-sectional dimensions of a dynamic impact test chamber readily available to the author was approximately $5x5$ cm, and thus the rectangle of dimensions 10 cm height, 5 cm width, and 5 cm depth was selected (of note, the unit cell features are extruded into the depth making this sample quasi-2D).

While it was desired to make the unit cell small (per the above guidelines), early prototyping experimentation with 3D printing resources available to the author revealed a minimum practical feature size of approximately 0.5 mm. Thus, an initial unit cell size was determined in order to fit roughly 10 unit cells along the height of the initial sample, and five unit cells along the width, for 50 total unit cells in the described case. This nomenclature is described in detail in section 2.4. The initial design trade-off met the initial design guidelines described above, however, as will be discussed later, manufacturing and testing a sample with more (smaller) unit cells is a goal of future work.

A discrete element model (DEM) was used to simulate the dynamics of the bistable metamaterial, where each layer of unit cells (a "layer" being defined here as a plane of unit cells who's normal is in the direction of the impactor velocity vector) were described as lumped mass layers in between massless bistable springs. A DEM was chosen as a reasonable model due to the following key assumptions: 1) Uniaxial loading of the plate impactor on the sample with minimal off axis loading effects; 2) Near zero effective Poisson's ratio of the lattice; and 3) The lattice is composed of stiffer and larger masses lumped within the material, and separated by softer, lower mass elements such that the individual vibrational frequencies of the individual mass and spring components are much higher than the frequency of the spring and mass combined, and thus the higher frequencies can be reasonably ignored. The sample mass was divided into equal "mass layers" in number equal to the amount of unit cells along the height of the material. The springs were modeled by fitting a polynomial function to the strain energy (or force) versus displacement response from FEM simulations of a single beam (or compressive tests on a single layer of five printed unit cells). This function was adjusted to account for the number of springs in parallel (along the width and depth of the material). A "contact spring" (which only supported compression) between the top unit cell and the impactor mass was modeled to describe the impactor hitting the top of the sample and allowed the impactor to freely bounce rather than stick to the top of the lattice after impact. This contact spring transitioned stiffness between zero and a stiffness exceeding the bistable stiffness in accordance with a

Hertzian-like, nonlinear, contact model [12]. This allowed for a better estimation of the physics of impact than simply assigning a prescribed velocity to the top layer of the material, including roughly describing the impactor coming into contact with the sample given slight relative angle between, and asperities on, the two surfaces. It also alleviated potential integration difficulties within the DEM as a result of force discontinuities. Further discussion and the equations used for the contact spring are in section 2.6.

Based upon the theoretical elastic strain energy trapping potential of half the sample, the low amplitude linear stiffness of the lattice, and the density of the lattice, a relationship was developed to estimate the nominal conditions for mass and velocity of the impactor (discussed further in Sec. 2.7). These values were used as a starting point for DEM simulation, then adjusted from these initial values in order to study the metamaterial's performance as a function of impactor characteristics.

In order to compare the performances of the designed lattice (both in simulation and later in experiment), an appropriate metric of "goodness" was required. As stated by Avalle and Montanini et al. "An optimum energy-absorbing material needs to dissipate the kinetic energy of the impact while keeping the force on it below some limit" [55]. Following this idea, and as suggested earlier in this section, the maximum instantaneous kinetic energy of the material at half the sample height was chosen as the comparative metric. One half the sample height was chosen as the point to measure the velocity, and calculate kinetic energy, in order to avoid boundary effects. A detailed discussion of the decision to use kinetic energy is discussed in Section 8.

2.1 Choice of control constitutive relationship

A control material (or control constitutive response) was necessary in order to assess the relative performance of the bistable mechanism; thus a material of matched low-amplitude, linearized stiffness, and matched "relative density" (*i.e.*, total sample mass / volume) was chosen for the following reasons. Regarding stiff-

ness, our DEM simulations showed negligible (approximately 1% maximum) energy transmission difference at the half height between linear materials of different stiffnesses, when analyzed from impact time until the time the first wavefront hits the bottom of the sample. This is shown in Fig. 2.5 using Quality Factor $Q = 100$ linear interlayer damping, $N = 100$ layers, and a total simulation duration of 0.14 s. Quality factor is a unitless quantity defined by: $Q = (\sqrt{k_L m_L})/\eta$, which results in the adjustment of layer damping (η) due to different stiffness values, where m_L is the layer mass, and k_L is the layer stiffness. The "monostable trial 1" (MT1) lattice has a layer stiffness value of $363,960$ N/m and the "monostable trial 2" (MT2) lattice has a value of $5,958,400$ N/m, yet a negligible difference in kinetic energy density transmission is seen across the tested impact, even with some nonlinear effects as a result of the inclusion of the contact spring in this example and over an order of magnitude difference in stiffness.

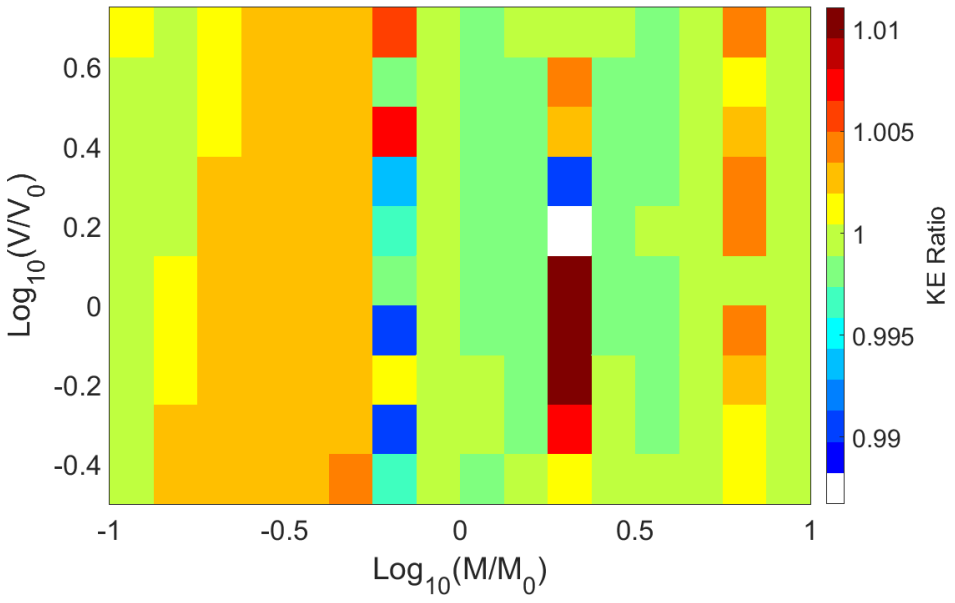

Figure 2.5: , both of linear stiffness, but different stiffness magnitudes, using quality factor $Q = 100$ linear interlayer damping. The stiffness of the linear comparative beams has little effect on the maximum kinetic energy transmission at the halfway point, as indicated by ratios close to one throughout (the minimum is 0.99 and the maximum 1.01. The nominal impact conditions for this sweep were: $V_0 = 18.6$ m/s and $M_0 = 0.18$ kg. Variables M and V represent the chosen impactor mass and velocity.

Comparing a single case represented within Fig. 2.5, Fig. 2.6 shows the kinetic energy as a function of space (particle number) and time for the MT1 and MT2 cases. Here, we see that each lattice has a different wavespeed, yet the kinetic energy transmitted is approximately the same.

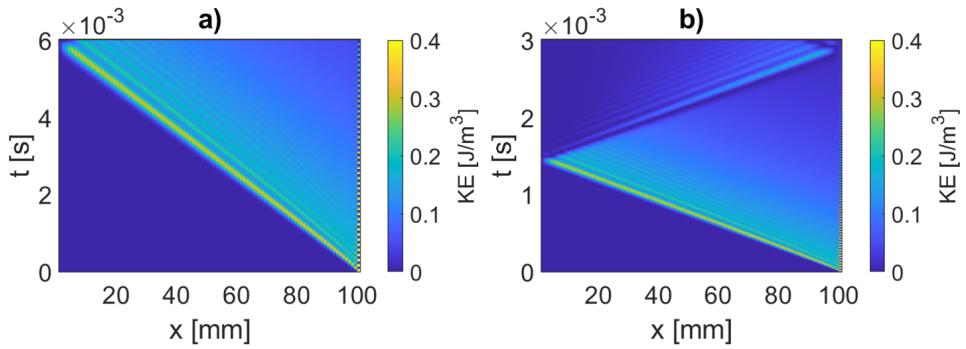

Figure 2.6: Kinetic energy, simulated via DEM, for the linear comparative materials MT1 (a) and MT2 (b), both struck at impactor conditions $V_0 = 18.6$ m/s and $M_0 = 0.18$ kg, modeled using $Q = 100$ linear interlayer damping.

The kinetic energy density transmission's insensitivity to material stiffness is also consistent with conservation of linear momentum within an elastic collision. In the context of an elastic collision between two bodies, the mass and velocity of impactor and absorber are the driving factors and material stiffness plays no role. Consider:

$$m_1 u_1 + m_2 u_2 = m_1 v_1 + m_2 v_2, \tag{2.2}$$

where the "1" subscript represents the impactor, the "2" subscript represents the absorber, "m" represents mass, "u" represents velocity before impact, and "v" represents velocity after impact. In the limit of infinite initial absorber mass and initial velocity of zero, any finite combination of initial mass and velocity of the impactor will result in zero velocity for the absorber post impact (and thus zero kinetic energy transferred to the absorber). For these reasons the magnitude of the stiffness of the linear comparative material was of little importance, although matching it somewhere close to the low amplitude linear stiffness value of the bistable material was useful in order to get simulation timing to match closely.

From an applied perspective, referencing again Eq. 2.2, while an absorber of increasingly larger mass would absorb less kinetic energy, an absorber of extremely high mass is of little practical utility. The keen reader will likely note that this explanation using single particle collisions is an extreme simplification of the wave dominated scenario in question, although the indifference to stiffness in the results suggest that in this instance it is an appropriate one. Thus, in simulations, it was essential to match the relative densities of the bistable and linear comparison material, although matching their long wavelength linear stiffness values was not.

2.2 Fitting and stiffness parameters

Different force versus displacement (or strain energy versus displacement) curves were created (either through FEM or through experimental measurement of physical samples) and used at different points for the data in this work. The FEM simulations were conducted in COMSOL version 5.2 using a stationary solver (geometric nonlinearity enabled), with "Automatic" selected in the "Linearity" list to allow the software to detect whether a linear or nonlinear solving method was used. The MUMPS (default) solver was used for the direct linear system solver, and "Double dogleg" was selected for the nonlinear method. The following boundary conditions were set (as shown in Fig. 2.3(a)): fixed bottom on the short left edge, prescribed displacement downwards on the short right edge (no lateral movement), and free sides (long edges). In order to produce a strain energy vs displacement curve within the desired strain range, an initial constitutive model was needed in order to allow the material to undergo large deformation, and thus (while understood not to be well matched to the initial material choice of aluminum) the Neo-Hookean hyper-elastic constitutive model was used with aluminum material properties (Lamé Parameters: $\lambda = 4.7191e10$ kg/m^3, $\mu = 25e9$ N/m^2, $\rho = 2570$ kg/m^3). This early analysis assumed that only the beam (described by variable L and arbitrarily set to eight millimeters in this case) in Fig. 2.2 would deform and all other portions of the unit cell would remain rigid. This allowed for the construction of an initial strain energy versus displacement curve (shown in Fig.

2.3(b)), which was used for initial DEM simulations of dynamic impact. The equation for this curve describing strain energy as a function of displacement $w(u)$ was fit by the following polynomial:

$$w(u) = \frac{1}{2}\beta_1 u^2 + \frac{1}{3}\beta_2 u^3 + \frac{1}{4}\beta_3 u^4. \tag{2.3}$$

After initial FEM and DEM simulations were completed, a single, ten millimeter height lattice layer was 3D printed on a Stratasys Polyjet 3D printer. The beams were made from Tango Black Plus, a rubber simulant with bulk modulus $\approx 8.42e5$ N/m^2 (from a small strain linear estimate). The "monolithic" (*i.e.* non-beam) portion of the sample was constructed of the stiffer Veroclear material (acrylic simulant, bulk modulus $1.54e9$ N/m^2) in order to prevent unwanted bending. Subsection 2.3 describes further rationale for the dual material choice. The sample was then mechanically tested in compression, using an MTS Exceed Model E43 electromechanical static test system. The resulting force versus displacement $F(u)$ curve for a single beam from this test which was subsequently fit to a third order polynomial was:

$$F(u) = \beta_1 u + \beta_2 u^2 + \beta_3 u^3. \tag{2.4}$$

The reader will note that Eq. 2.4 is the first derivative of Eq. 2.3 with respect to displacement. The choice to use one or the other is a matter of convenience. For instance, in FEM the calculation of strain energy or force is equally convenient, while the mechanical tester used by the author output force versus displacement, which made Eq. 2.4 convenient when using experimental data.

Fittings were completed with no 1st order term (for strain energy fit), or no zeroth order term (for force displacement fit) in order to ensure zero force at zero displacement. Generally, simulations were completed with a 3rd order fit in force versus displacement, which resulted in the desired bistable curve shape while keeping the number of fitting coefficients low. In the case of later simulations where post-buckled stiffness was altered, a 5th order fitting in force vs displacement was used in order to capture the stiffness differences and maintain stability at higher values of compression.

Table 2.1: Material and Coefficient table. "EXP" = fit from experimental data, "MTL" = material, TB = Tango Black, "VC" = Veroclear, "Alum" = Aluminum. "*" refers to piece wise altered FEM for softer post-buckled stiffness.

	β_1 (N/m)	β_2 (N/m)	β_3 (N/m)	β_4 (N/m)	β_5 (N/m)	Type	MTL	H_C (mm)
A	2.26e3	1.19e6	1.52e8			EXP	TB/VC	10
B	2.00e8	4.74e10	2.65e12			FEM	Alum	24.9
D	1.61e8	4.45e10	4.08e12	1.49e14	1.94e15	FEM	Scaled	24.9
E	1.61e3	4.86e5	3.52e7			FEM	Scaled	24.9
F	2.24e3	5.08e5	2.75e7			FEM	Scaled	24.9

The values of the fitting coefficients (*i.e.* β) for the FEM and experimental data discussed above are shown in the Table 2.1, with the FEM example described above labeled "Set C" and the experimental example (described above) is labeled "Set A". The "β" coefficients correspond to the polynomial describing the force versus displacement relationship for a single beam in the system. Beam lengths associated with the β coefficients are 8 mm for all sets except Set A, which is 3.2 mm. The beam depth was always d. Set A is the "default" parameter set, and used for the majority of the simulations in this work. In simulation, cases using Set C data (i.e. β values derived from FEM) resulted in a higher maximum performance ratio than cases using Set A data (i.e. β values derived from experiment). However, the decision was made to do further analysis and show figures primarily from Set A data, despite their lower performance, because this was expected to produce more conservative results. The maximum performance ratio metric used is described in Sec. 3.1.

Additional strain energy functions were produced in order to better understand the effects of beam angle, post buckled stiffness, and material scaling. Set D is for a fifth order polynomial which is used specifically for the investigation the effect of changing postbuckled stiffness on performance, described in section 7. This polynomial was fit based on the same FEM data used in Set C, except the post buckled stiffness was altered manually. Set E and set F are used for the investigation in performance differences as a result of changing the beam angle from 60 degrees (Set F) to 40 degrees (Set E). This was useful for assessing the feasibility of moving from a dual material 3D printed lattice to a single material

lattice for the current design, as described in section 10.1. Set E and Set F are from FEM data for Aluminum which was then arbitrarily scaled to a fictitious material with an elastic modulus of $8.42e5$ N/m^2. The scaling process is described in Sec. 2.8.

2.3 Rationale for dual material design

Initial prototyping of the bistable lattice experimentally showed that the single material lattice did not exhibit bistable characteristics when compressed, but instead it rebounded when a load was no longer applied. Subsequent FEM simulation revealed evidence of the cause, as shown in Figure 2.7.

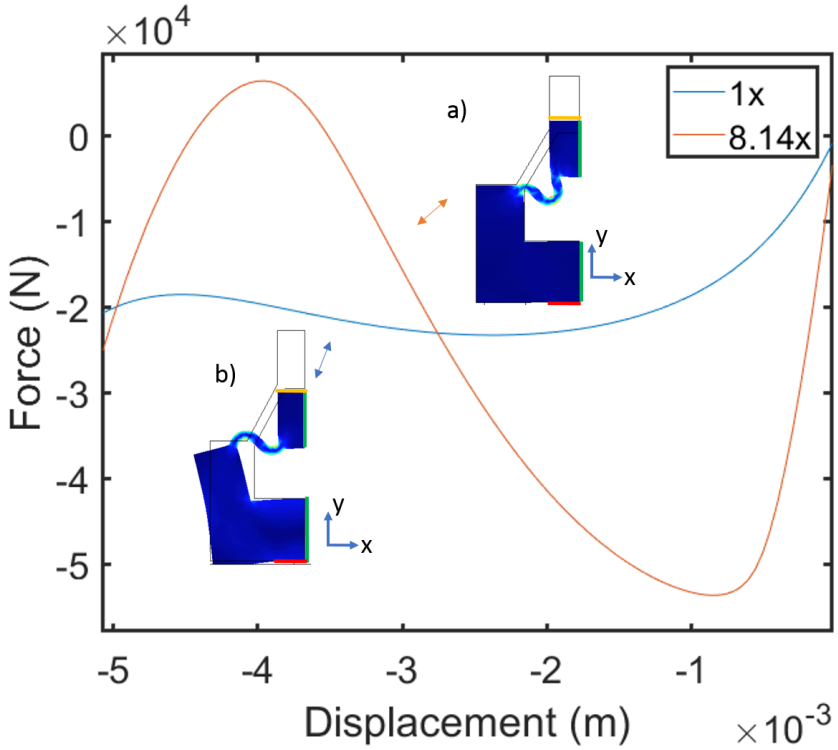

Figure 2.7: The blue line and cartoon labeled "b)" represent a single material unit cell design. The orange line and cartoon labeled "a)" represent a dual material design where the Young's Modulus of the monolithic portion of the unit cell is 8.14x the value of the beam.

Figure 2.7 shows the results of COMSOL FEM of one-half of a dimensioned unit cell (per Sec. 2.5) with $H_C = 10$ mm, $r = 0.14$, and $\theta = 60$ degrees. The COMSOL FEM settings and arbitrary material choice of aluminum were as per Sec. 2.2, with the exception of the boundary conditions. The boundary conditions are marked by their line color in the half unit cells in Fig. 2.7: prescribed displacement (orange), symmetry (green), roller(red), then free for everything else. The prescribed displacement was applied in the "negative Y" direction only, per the

coordinate system in the figure, up to a unit-cell strain value of $\varepsilon = 0.5$, which was greater than ε_2 but just prior to ε_{sc}. The blue line in Figure 2.7 shows the force versus displacement curve when the entire unit cell was designed from a single material, and is compressed: while negative stiffness is seen, zero force bistability (which is the desired behavior) is not. The cartoon labeled Fig. 2.7(b) is associated with the blue line, and indicates that bending of the monolithic portion of the unit cell is spoiling the desired bistability. The author notes that tessellating multiple unit cells may improve this unwanted bending. The orange curve shows the results of the same simulation, with the exception that μ was multiplied by ten only for the monolithic (i.e. non-beam) portion of the unit cell, resulting in a 8.14x increase in the Young's Modulus of the monolithic portion for the orange curve in comparison to the blue curve. As a result of this change, zero-force bistability is achieved, and as shown by Figure 2.7(a), there is little to no outward bending. Of note, while an 8.14x increase in Young's Modulus is shown, a minimum of 5.8x was required for zero force bistability using the same method of FEM described above.

This analysis validated that the modulus ratio (monolithic/beam $\approx$ 1800x) for the produced dual material lattice, (a single layer of which was tested for set A parameters, as previously discussed), was more than adequate to limit bending of the monolithic portion of the beam. It also indicated that the current experimental modulus ratio match-up was probably more than is advantageous, considering the general correlation between modulus and material density. This knowledge indicated opportunities for modifications of the unit cell in the aim of designing a more efficient or more easily producible (*e.g.* single material) design. Some ideas for optimization are discussed in Chapter 10.

2.4 Relating beam response to unit cell behavior

The polynomial described in Eq. 2.4 was valid for a single beam, however the goal of simulation was to model a lattice made of multiple unit cells (with two beams per unit cell). Thus, it was necessary to scale Eq. 2.4 such that simulation

could be completed for any sized system. Force and displacement were converted to stress and strain in order to make the equations geometry independent. To simplify calculations, a square unit cell assumption was made, thus unit cell height H_C equaled, and was substituted for, unit cell width W_U. The stress of the unit cell is:

$$\sigma = \frac{2f(u)}{H_C d}, \tag{2.5}$$

recognizing that each unit cell had 2 beams, and the cross-sectional area the force was acting on was represented by $H_C d$. Note that H_C, W_U, and d refer to the dimensions of the unit cell associated with the arbitrarily sized beam. Further note that whether referring to unit cell or sample depth, d is the same.

Unit cell strain was defined as:

$$\varepsilon_u = \frac{u}{H_C}. \tag{2.6}$$

Using Eqs. 2.6 and 2.5 allowed stress to be described as a function of unit cell strain, such that:

$$\sigma = \frac{2}{d}(\beta_3(H_C^2)(\varepsilon_u)^3 + \beta_2(H_C)(\varepsilon_u)^2 + \beta_1\varepsilon_u). \tag{2.7}$$

For our DEM simulation, it was necessary to scale Eq. 2.7 such that it applied to any arbitrary DEM layer spacing. First, the relationship between DEM layer height a and sample height $H_s = Na$ was established, where N is the number of layers. Since sample width was chosen to be one-half of the sample height, sample width $W_s = Na/2$. Thus, a 100 layer (*i.e.* $N = 100$) sample would be composed of 100 unit cells in height by 50 in width, resulting in 5000 total unit cells modeled. Now, representing layer strain ε_L by the relationship $\varepsilon_L = \delta/a$, and the area over which the stress acts in a layer as $Nad/2$, the layer force can now be expressed in terms of DEM layer displacement δ:

$$F_L = Na(\beta_3 H_C^2(\frac{\delta}{a})^3 + \beta_2 H_C(\frac{\delta}{a})^2 + \beta_1(\frac{\delta}{a})). \tag{2.8}$$

Equation 2.8 allows for the expression of force per layer in DEM for any amount of N layers and DEM spacing a given β values from a single beam and a known

unit cell height H_C associated with that beam. Excluding the higher order terms, the linear layer stiffness for any amount of N layers simplifies to:

$$k_L = N\beta_1. \tag{2.9}$$

The author expected the strain energy of a given sample size to be independent of the amount of layers chosen. To check this, we refer back to Eq. 2.7 and introduce sample displacement $D = N\delta$, and the relationship $\varepsilon = D/L$, resulting in the equation for force per sample:

$$F_S = 2d(\beta_3(H_C^2)(\frac{D}{L})^3 + \beta_2(H_C)(\frac{D}{L})^2 + \beta_1\frac{D}{L}). \tag{2.10}$$

One should note that $L = Na$, and N and a are inversely proportional to each-other such that force per sample, and strain energy per sample are independent of N.

These relationships allow for the scaling of the design to any layer size. It is also noteworthy that from these relationships, at least in the quasi-static sense, there is no difference in energy trapping predicted as a result of unit cell (or layer) size. The fact that dynamically, our data suggests substantial differences in performance are seen as a result of changing unit cell size specifically is one motivation for this work (discussed in section 5).

2.5 Unit cell design

The unit cell design, (shown on Fig. 2.2), was constructed such that all parameters could be related to three picked variables: θ (which was selected as 60 degrees, excepting chapter 10), L, and $r = T/L$ (which was selected as 0.14). As discussed in the introduction, the unit cell was designed such that $\varepsilon_2 < \varepsilon_{sc}$ (where as a reminder, subscript ε_{sc} denotes the strain at self contact). It was then desired to maximize the width of W_3 in order to increase the stiffness of this horizontal portion of the unit cell, although it was also necessary that the size difference between W_2 and W_3 be sufficient to prevent interference between the sides of the unit cell and the buckled beams, which was addressed by the following relationship:

$$W_2 = 2L\cos\theta + W_3. \tag{2.11}$$

The author freely notes that this rough method of dimensioning leaves many opportunities for future work to optimize the unit cell to better mass efficiency. Additionally, L_3 was set to match L_2, such that there was sufficient room to prevent premature self contact. These constraints were satisfied by the following relationships:

$$L_2 = L_3 = W_3 = 0.8875L. \tag{2.12}$$

Next, L_1 was dimensioned such that $L_3 - L_1$ was at least 3x larger than T in order to minimize bending of the monolithic portion, and thus $L_1 = 9.707T$ was chosen. The unit cell height was now described by $H_C = L_1 + L_2 + L\sin\theta$, and the unit cell width was described by $W_U = 2L\cos\theta + W_3 + 2W_1$. Finally, W_1 was dimensioned such that $W_1 = 4.375T$ in order to make $H_C = W_U$.

The "relative density" of the unit cell, ($\rho_{rel} = M_U/V_R$), was then defined, where M_U was the mass of the unit cell, and V_R was the total outer volume of an imaginary cube that the dimensioned unit cell would fit within. This relationship was used in order to determine (m_L) for the DEM simulation. Defining ρ_b as the bulk density of any chosen material, then substituting the geometric parameters shown previously for the unit cell results in the following relationship:

$$\rho_{rel} = \frac{\rho_b(2L_1W_1 + W_2L_1 - W_2L_3 + L_2W_3 + 2TL)}{(2L\cos\theta + W_3 + 2W_1)(L_1 + L_2 + L\sin\theta)}. \tag{2.13}$$

Now, layer mass is described by:

$$m_L = \rho_{rel} a d^2 \tag{2.14}$$

2.6 DEM modeling algorithm

The DEM simulation was constructed using the ODE45 numerical integrator in Mathworks MATLAB in order to solve a system of "$N+1$" ordinary differential equations, which counted for each layer as well as the impactor mass [120]. The sign

convention was in accordance with Fig. 2.3(c). Starting from the top (where the sample is impacted), the first equation described the impactor mass striking the top of the sample—no damping was modeled for this portion of the impact modeling, and the impact was described by a Hertzian-like nonlinear contact model [12]. This function only applied a force when the downward displacement was < 0 in order to simulate an impactor hitting a structure, then being freely able to bounce, and is shown below:

$$M\ddot{y}_i = C_1 E_{lin} a^{-1.5} d^{-2} ([y_{i-1} - y_i]_+)^{\frac{3}{2}}, \tag{2.15}$$

where the $[]_+$ denotes spring's inability to support tension. In Eq. 2.6, M represented the top mass (shown in Fig. 2.3(c)), y_i represented displacement of this mass, $E_{lin} = 4\beta_1/d$ was the Young's Modulus of the surface being impacted derived from its linear stiffness value, and C_1 was an arbitrarily set fitting coefficient. The number of asperities was arbitrarily set to 10, then for simulations, C_1 was set to -119.21. For experimental matching (discussed later), C_1 was adjusted based on qualitative factors from experimental impact in order to get a closer phenomenological match between the simulation and experimental data.

The next equation describes the top layer of the absorber, being struck by the impactor:

$$\begin{aligned} m_L\ddot{y}_i = {} & C_1 E_{lin} a^{-1.5} d^{-2} (y_i - y_{i+1})^{\frac{3}{2}} \\ & - (\frac{2d}{H_c})(\beta_3 (\frac{H_c}{a})^3 (y_i - y_{i-1})^3 + \\ & \beta_2 (\frac{H_c}{a})^2 (y_i - y_{i-1})^2 + \beta_1 (\frac{H_c}{a})(y_i - y_{i-1}))) \\ & - \eta(\dot{y}_i - \dot{y}_{i-1}), \end{aligned} \tag{2.16}$$

where m_L refers to the first mass beneath impactor mass M in Fig. 2.3(c)), and y_i represents the displacement of m_L. The spring above the mass layer was described by Eq., with the exception of the term $y_i - y_{i+1}$. The spring below the mass layer was the bistable spring, and η described the linear layer damping value.

The third equation modeled the layers in-between the top and the bottom of the sample (*i.e.*, in Fig.2.3(c)), counting up from the fixed base, the second and

third mass)—thus the ordinary differential equations (ODEs) described a mass spring system with linear intersite damping, and nonlinear, bistable, springs on either side:

$$\begin{aligned} m_L\ddot{y}_i = &(\frac{2d}{H_c})(\beta_3(\frac{H_c}{a})^3(y_{i+1}-y_i)^3+ \\ &\beta_2(\frac{H_c}{a})^2(y_{i+1}-y_i)^2+\beta_1(\frac{H_c}{a})(y_{i+1}-y_i)) \\ &-(\frac{2d}{H_c})(\beta_3(\frac{H_c}{a})^3(y_i-y_{i-1})^3+\beta_2(\frac{H_c}{a})^2(y_i-y_{i-1})^2 \\ &+\beta_1(\frac{H_c}{a})(y_i-y_{i-1})) \\ &+\eta(\dot{y}_{i+1}-\dot{y}_i)-\eta(\dot{y}_i-\dot{y}_{i-1}). \end{aligned} \tag{2.17}$$

The bottom mass (*i.e.* "Mass 1" in Fig.2.3(c), with y_i referring to the displacement of this mass) was similarly described, except the bottom boundary was fixed (Eq. 2.18):

$$\begin{aligned} m_L\ddot{y}_i = &(\frac{2d}{H_c})(\beta_3(\frac{H_c}{a})^3(y_{i+1}-y_i)^3+ \\ &\beta_2(\frac{H_c}{a})^2(y_{i+1}-y_i)^2+\beta_1(\frac{H_c}{a})(y_{i+1}-y_i)) \\ &-(\frac{2d}{H_c})(\beta_3(\frac{H_c}{a})^3(y_i)^3+\beta_2(\frac{H_c}{a})^2(y_i)^2 \\ &+\beta_1(\frac{H_c}{a})(y_i)) \\ &+\eta(\dot{y}_{i+1}-\dot{y}_i)-\eta(\dot{y}_i). \end{aligned} \tag{2.18}$$

The ODE45 options structure was set to default values for everything except initial step size, and maximum step size [120]. The initial step size was set to $1e-6$, then maximum step $= (\pi/500)(\sqrt{m_L/k_L})$. The initial values for the integrator were set to all zero, with the exception of the velocity of the end mass, which was set to the impactor velocity. The values for β for the different simulation runs are described in Table 2.1. Of note, the constitutive relationship for the "control" beam was taken in a similar manner, although there were no nonlinear terms (*i.e.* β_2 or β_3).

The total simulation time was adjusted based on the particular simulation case, and described prior to each case. In some instances, the simulation time was

adjusted in order to isolate the maximum energy transmission to occur between the impact point and the first wavefront hitting the bottom of the sample, in order to isolate the analysis of these effects from anything that might happen afterwards. This was particularly useful when analyzing undamped cases, or cases with very little damping. In other cases, the simulation time was run long enough that the velocity of the impactor had at a minimum began to reverse direction (*i.e.* the material started to rebound from maximum compression). This length of time was chosen because it allowed the impactor to impart all of its kinetic energy to the sample, and allowed for analysis of the system during interactions past the initial wavefront.

Since an essential part of the study was to better understand the effects of changing impactor mass and velocity on the performance of the sample, an exponential sweep was set, such that once the nominal impact conditions were estimated, exponential increments of these values could be tried. For instance, for a nominal test sweep where nominal impactor mass (M_0) and nominal impactor velocity (V_0) were set, additional iterations were controlled from a default mass sweep range of $M/M_0 = 10^{-1}$ to $M/M_0 = 10^{1}$ and velocity sweep range of $V/V_0 = 10^{-0.5}$ to $V/V_0 = 10^{0.75}$. Calculation of the M_0 and V_0 values is discussed in Sec. 2.7.

The outputs of the ODE45 simulation were matrices of the displacement and velocity of each mass at each timestep for the duration of the simulation, for each pairing of impactor mass and velocity. These outputs were used to calculate kinetic energy (KE), potential energy (PE), total energy (TE), and "spring stretch". Potential energy was calculated from the spring stretch below the mass, then TE is the sum of KE and PE. Kinetic energy, TE, and PE values were converted to energy density by dividing the energy in each layer for a given time step by the volume of said layer (ad^2). Two of these plots are shown below in Fig. 2.8 and Fig. 2.9, for the reference and bistable lattice, respectively. In Fig. 2.8, the results of a sample DEM simulation with no damping, for a 100 layer linear case are shown, impacted at impactor conditions $M_0 = 18$ g and $V_0 = 3.6$ m/s. The simulation duration variable $T_s \approx 1.2$, where $T_s = T_{lin}/T$, and T_{lin} represented the approximate time for the linear wave to travel across the sample once, and T represented

the absolute simulation duration, which was 0.012 s.

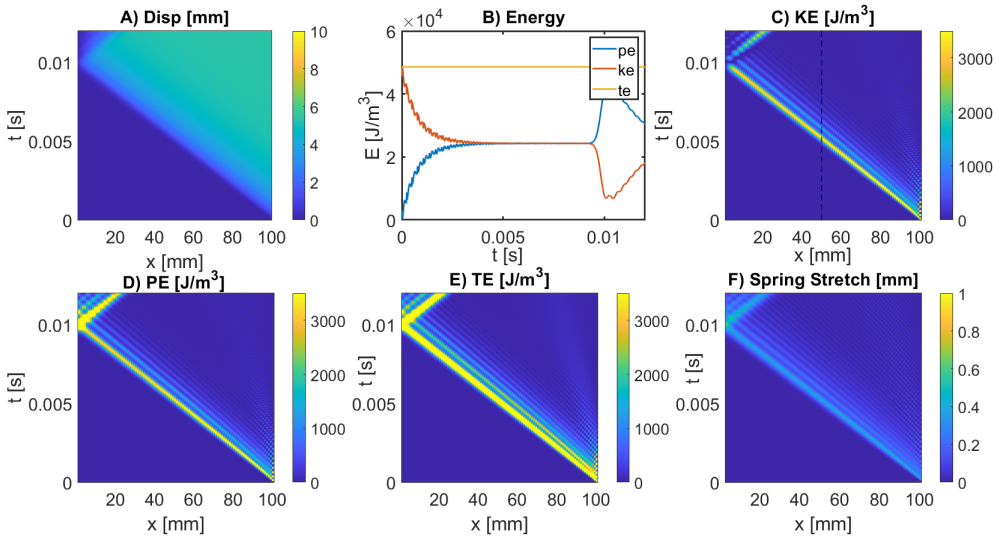

Figure 2.8: in terms of (A) particle displacement, (B) Kinetic, potential, and total energy density over the whole lattice, (C) kinetic energy density, (D) potential energy density, (E) total energy, and (F) spring stretch. The impact occurs at the bottom right of all panels except for (B), where it occurs at the bottom left.

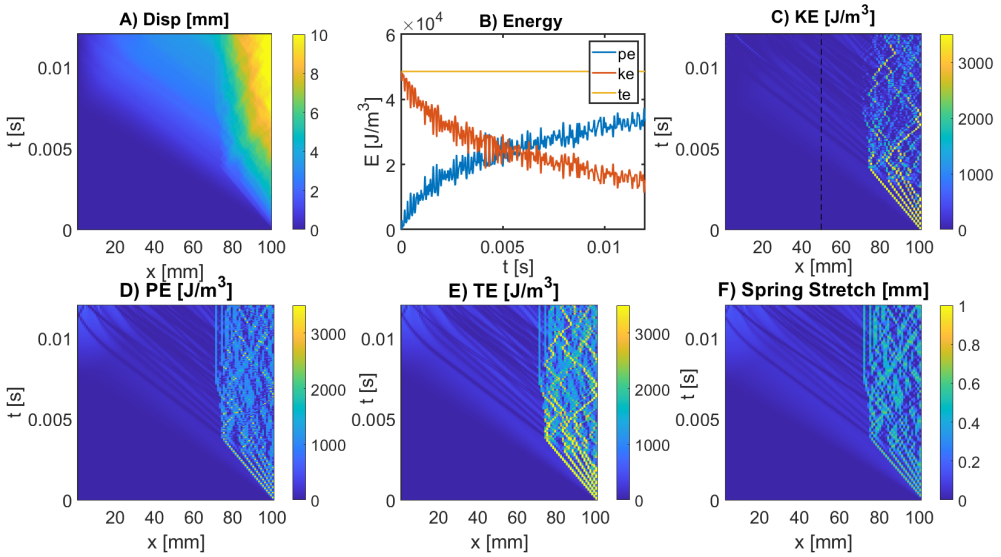

Figure 2.9: shows different quantities of wave propagation in terms of (A) particle displacement, (C) kinetic energy density, (D) potential energy density, (E) total energy, and (F) spring stretch. Panel (B) shows the summation of kinetic, potential, and total energy density of the lattice, including an extra "layer" (of the same size as the other layers) for the impactor. Only 0.16 kJ/m^3 of KE density is transmitted, or 20.9x less than the linear sample in Fig. 2.8.

The point of impact between the impactor and the sample is at $x = 100$ mm and time ($t = 0$) s, and is depicted by the bottom right corner of the panels (excepting the top middle panel) in Fig. 2.8 and Fig. 2.9. Of note, the impactor is not included in the displacement or spring stretch spatiotemporal diagrams, although it is included in conservation of energy calculations as well as: KE, TE, and PE spatiotemporal (XT) diagrams. In Fig. 2.8(a), we see a compression of the material of approximately 6 mm which travels at a speed of approximately 10 m/s from one end of the material to the other. Figure 2.8(b) shows PE density, KE density, and TE density, summed over all particles, vs. time. The impactor is assumed as one additional layer having the same volume as every other layer (ad^2) for this calculation. Here it is seen that initially all the energy is kinetic (from the impactor), which subsequently transitions between kinetic and potential as the wave propagates through the sample. Total energy is conserved, in this case, since damping is not modeled. Figure 2.8(c) shows the KE density that propagates

through the sample, as a result of the velocity imparted to the absorbing material. Since KE density is also the chosen comparative metric, the maximum KE density which occurs at 50 mm (or the $N/2$ layer) is 3.4 kJ/m^3. Figure 2.8(d) and Fig. 2.8(f) represent the potential energy density (PE) and the spring stretch, which are closely related. Spring stretch shows the local stretch of each layer within the material (with positive stretch representing compression), while potential energy uses this information with the material constitutive relationship in order to relate it to strain energy. Finally, in Fig. 2.8(e), the TE density adds the KE and PE density plots together.

In contrast to the linear material (Fig. 2.8), the bistable material (Fig. 2.9) clearly shows nonlinear effects. Observing first the displacement plot (Fig. 2.9(a)), a larger displacement of up to 10 mm is seen in terms of the cumulative displacement of the top of the sample compared to its position prior to impact. However, very little displacement is seen at the half height as well as at the bottom of the sample. The energy density plot in Fig. 2.9(b) again shows total energy conservation and the trade-off between KE density and PE density, although it also shows additional dynamic effects such as higher amplitude vibrations. In Fig. 2.9(c), we see the first indication of the richness of the bistable system. Initially, we see solitary wave emission at the onset of impact, as shown by the straight, yellow lines that progress approximately 25 mm into the sample. Looking first at each of these emissions, we see that the first wave appears to be the fastest, then the next two are progressively slower, as indicated by the steeping of the slope on the diagram. This is possibly a result of the amplitude dependent wavespeed of the nonlinear wave; since the highest impact energy happens at the moment of impact this results in the fastest wave. As the energy of the impactor is shed into the material, the subsequent waves at the location of impact but after $t = 0$ are slightly slower. The energy is shown clearly in Fig. 2.10, which takes a "slice" of Fig. 2.9(c) at $t = 3$ ms over the top 40 mm of the lattice. The KE density of the first solitary wave is 3.97 kJ/m^3, then 3.65 kJ/m^3 for the second, then subsequently lower for the third and fourth. Referring back to Fig. 2.9(c), we additionally note that beyond approximately 4 ms from the $80 - 100$ mm point of the material, we see a complex

and oscillatory behavior, likely a result of vibrations of the bistable structure in these first (approximately) 20 layers from impact. Crucially, past approximately $20 - 25$ mm from impact, very little KE density is transmitted further into the sample, and at the N/2 point, only 0.16 kJ/m^3 of KE density is transmitted, or 20.9x less than the linear sample in Fig. 2.8. The remaining panels (Fig. 2.9(d) to Fig. 2.9(f)) show qualitatively similar phenomenon as was seen in Fig. 2.9(c)): it appears that solitary waves develop initially, then there is an oscillatory behavior, as previously described. While the dynamics are far more complex in this system compared to the linear case, the bottom line for purpose of comparison is that very little energy is transmitted though the half height of the sample, indicating a substantial benefit in terms of energy absorption as a result of using a bistable lattice at this particular choice of impactor mass and velocity for the given sample lattice. The calculations regarding the determination and understanding of superior and inferior regions of performance is a major focus of this dissertation, and discussed further.

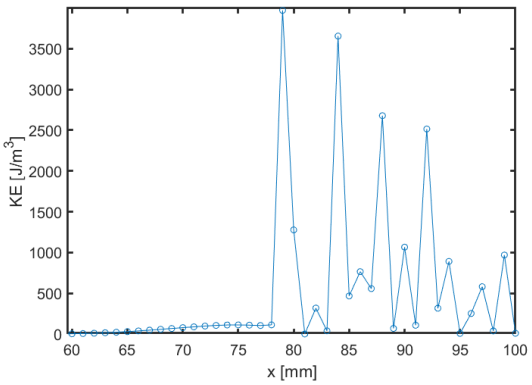

Figure 2.10: Kinetic energy density at $t = 3$ ms for the top 40 mm of the bistable lattice shown in Fig. 2.9(c).

2.7 Estimation of nominal impact conditions for dynamic effects

To calculate the nominal impact velocity (V_0), a "desired strain" (ε_0) was selected as the strain at the first inflection point of the strain energy vs displacement curve (*i.e.* onset of negative stiffness), which is shown by the blue arrow in Fig. 2.3(b). Eq. 2.19 from text [3] was used to determine impactor velocity:

$$V_0 = 2c_0\varepsilon_0, \tag{2.19}$$

where the long wavelength linear sound speed is:

$$c_0 = a\sqrt{\frac{k_L}{m_L}}. \tag{2.20}$$

Equation 2.19 assumed elastic wave propagation within a cylindrical rod after impact from another rod of the same material and same cross sectional area, with lateral strain assumed zero [3].

Since all initial energy resulted from the impactor velocity and mass, and the material was designed to absorb all energy at the "half-height" of the sample, a nominal impactor mass was estimated by setting impactor kinetic energy equal to elastic strain energy produced by compression of the first half of the bistable sample. Each of the layers in the first half of the sample were assumed to compress to a final strain value ϵ_2 corresponding to the bottom of the second energy well of the blue strain energy versus displacement curve in Fig. 2.3(b). In essence, this simulated a case where the impactor struck the material, then every layer in the first half of the sample was compressed to a strain of ϵ_2, which is described by the following (with F_L from Eq. 2.8):

$$PE = \frac{N}{2}\int_o^{a\epsilon_2} F_L(u)du. \tag{2.21}$$

Thus, based on the noted assumptions, we know PE, and based on the desired performance we'd like to achieve, we also know that if the KE imparted from the striker equals the calculated value for PE, ideally our system will be able to trap

all the energy, and there will be no remaining energy transmitted through the half sample. As an aside, in an ideal theoretical scenario, this would result in an infinite performance ratio (*i.e.* linear KE transmission/ bistable KE transmission). Thus, we set KE=PE at the PE value calculated from Eq. 2.21, then find M_0 as the only remaining unknown in the following equation:

$$KE = \frac{1}{2} M_0 {V_0}^2. \tag{2.22}$$

2.8 Scaling of nominal impactor mass and velocity based on lattice material density and elastic modulus

A relationship was developed such that a wide range of material properties (i.e. constituent materials making up the beams tested through FEM or experiment) could be simulated with similar performance benefits as long as the nominal impactor mass and velocity were scaled appropriately. Note that this scaling relationship assumes the same number of layers, same total sample dimensions, the same stress versus strain curve, and the same ε_2. Starting with nominal impactor mass and velocity of some arbitrary "baseline" material, V_{0b} and M_{0b}, we proceed. First, the 1D sound speed "c" of the new bulk material as well as the baseline material are calculated:

$$c = \sqrt{\frac{E}{\rho}}. \tag{2.23}$$

The impactor mass and velocity of the new material are then scaled according to:

$$V_{0n} = V_{0b}(\frac{c_n}{c_b}) \tag{2.24}$$

$$M_{0n} = M_{0b}(\frac{\rho_{0n}}{\rho_{0b}}), \tag{2.25}$$

where the "b" subscript represents "baseline" and "n" represents "new":

Equations 2.24 and 2.25 were verified through numerical (DEM) simulation, where a chosen baseline material with material properties: elastic modulus 67 GPa and density 2710 kg/m^3 was impacted at nominal impactor mass and velocity ($V_0 = 703$ m/s and $M_0 = 0.0391$ kg). Then a new material with properties: elastic modulus 20 MPa and density of 6000 kg/m^3 was impacted at nominal impactor mass and velocity for this new material ($V_0 = 8.2$ m/s and $M_0 = 0.0865$ kg), as calculated from the developed scaling laws in Eq. 2.24 and Eq. 2.25. The resulting spatiotemporal diagrams showed qualitatively the same behavior, and identical kinetic energy density reduction ratio of 9.62x (Fig. 2.11).

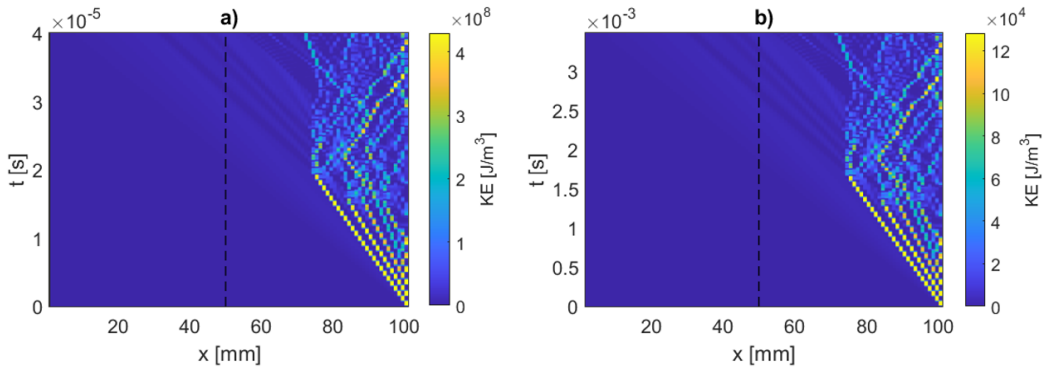

Figure 2.11: a) The KE density for an impact into a simulated aluminum block (impactor conditions: $V_0 = 703$ m/s and $M_0 = 0.0391$ kg). b) Impact into a block simulating a fictitious material with properties: elastic modulus of 20e6 Pa and density of 6000 kg/m^3 (impactor conditions: $V_0 = 8.2$ m/s and $M_0 = 0.0865$ kg). The important takeaway from the diagram above is that while the energy propagating through the material is different between the two cases, the observed qualitative behavior of the two cases is the same, as is the KE reduction ratio of 9.62x. Note: the maximum KE value was divided by nine in both panels in order to show the qualitative wave behavior more clearly.

Chapter 3

Performance as a function of impactor mass and velocity (N=100, no strain limitation)

Further expansion of the undamped, $N = 100$, short simulation duration (0.012 s, or ratio to linear wave transit time $T_s \approx 1.2$) case will be considered in this chapter, still with initially all the same constraints as used for Fig. 2.8 and Fig. 2.9, except now sweeps of varying impactor mass and velocity are presented. Then, the results are expanded to a longer period of simulation ($T_s \approx 20.5$), in order to highlight some observed complications of simulation in the fully undamped case. Next, a damped system observed to have a high KE ratio will be shown, and analyzed in a similar manner. The relationship between damping and performance will also be explored. It is important to note that for simplicity in this chapter, the simulations were not initially controlled for maximum unit cell strain.

3.1 Impact conditions sweep (undamped, short duration simulation)

Simulation sweeps were conducted that iterated plus and minus one order of magnitude in impactor mass, and plus and minus one-half order of magnitude

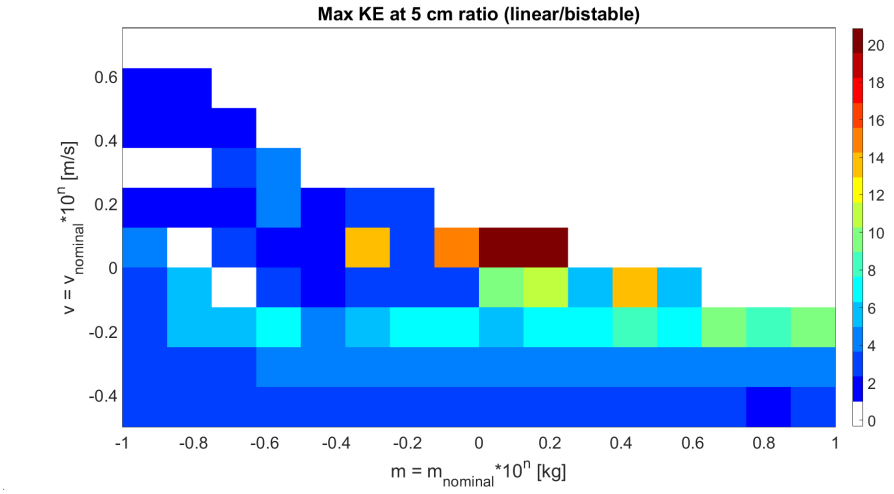

Figure 3.1: (set A from Table 2.1), modeled without damping, and $T_s \approx 1.2$. The maximum KE density ratio was 20.9x. A strong connection between impactor rate, impactor mass, and ratio of absorption is indicated.

in velocity for both the linear and bistable cases, and the maximum KE density values at the half height were stored for each case. These values were collected for both the bistable material and the linear material. The linear value was divided by the bistable one to produce a relative metric of energy transmission across a broad range of impactor mass and velocity. For instance a "KE ratio" of two would indicate that the linear material transmitted twice the KE density at the collection point as the bistable material.

It is clear from the results in Fig. 3.1 that within the right combination of impactor velocity and mass, substantially better KE ratio performance is available from the bistable material, relative to the comparative counterpart. However, it is also clear that within other regions the linear comparative's material outperforms the bistable for this same metric. Thus, a strong connection between impactor rate, impactor mass and KE ratio is indicated, however the mechanisms of these performance differences need to be investigated further. In order to investigate regions of superior and inferior performance, four individual cases are picked from Fig. 3.1 for further analysis and discussion: 1) The case of maximum bistable performance, 2) An intermediate case where performance is still better than the linear but well below the maximum observed 3) A case in the top left of the plot

where velocity is high and mass is very low, and 4) A case near the top right of the figure where both mass and velocity are high.

3.2 Analysis of spatiotemporal responses of four cases (undamped, short duration simulation)

The case showing maximum bistable performance also corresponded to the nominal impact conditions $M_0 = 3.16$ m/s and $V_0 = 18$ g. In Fig. 3.2, an annotated KE density diagram of the impact is shown, and an initial combination of solitary transition waves is observed. These waves subsequently stop prior to approximately the 70 mm point (but crucially before the 50 mm point shown by the black dashed line in Fig. 3.2, since this is our chosen metric). The waves transition to an oscillatory region, marked by the orange rectangle, where we see a combination of reflections, buckling, unbuckling, and interference. This region is also where the majority of the energy is trapped. The green bracket in Fig. 3.2 indicates the fastest of the first three solitary waves observed in the figure, as indicated by the shallowest slope (going from right to left), having a wavespeed of 7.1 m/s. The next two solitary waves (first wave is the base and the third wave is at the head of the red arrow, are decreasing wave speed (6.3 m/s, and 5.3 m/s), likely a result of the known phenomenon of amplitude dependent wave speed of nonlinear waves [111], in combination with correspondingly less energy imparted from the impactor as it sheds it's kinetic energy into the material. The small red bracket shows the initiation of the solitary waves and their correlation with the snapping and unsnapping of the top layer of the lattice. The resulting maximum KE density transmission is 163.51 J/m^3, 20.9x less than the transmission in the comparative case. This is an excellent example of a case where the impactor is well matched to the sample, resulting in good performance.

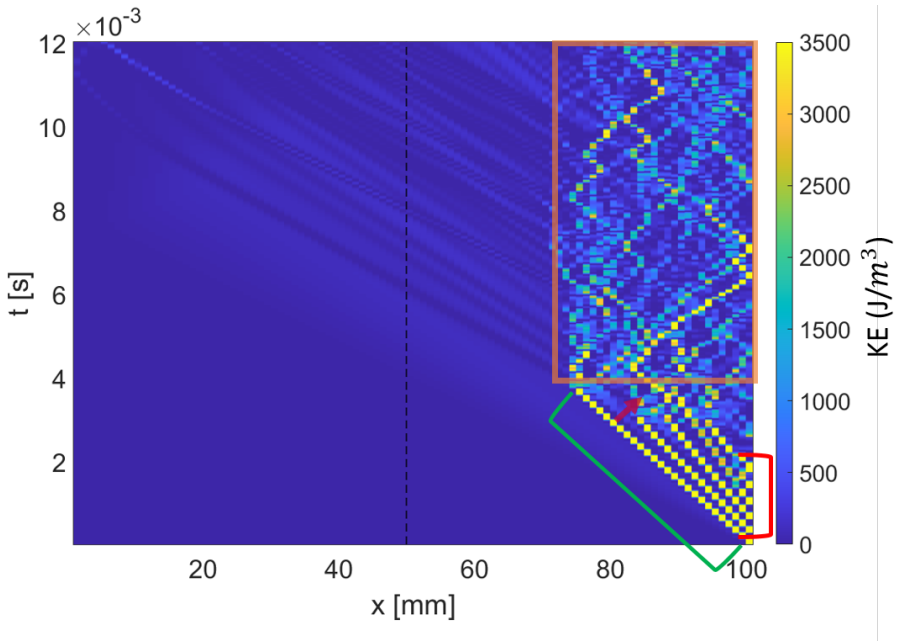

Figure 3.2: There is no damping modeled, and $T_s \approx 1.2$. The dashed black line shows the spatial position where KE density is calculated. The orange rectangle notes the dynamic nonlinear region. The small red bracket marks solitary wave emissions at impact. The green bracket notes the first solitary wave, and the red arrow marks subsequent, slower solitary waves. The resulting maximum KE density transmission is 163.51 J/m^3, 20.9x less than the transmission in the comparative case.

Figure 3.3 shows the KE density transmission of the linear comparative material at the same impactor conditions as were shown in Fig. 3.2. In Fig. 3.3, the small red bracket marks the impact point at the top of the sample, where we see some oscillatory motion as the impactor continues to compress the sample (reminder that the impactor is included in the plots of the KE density spatiotemporal responses). The green bracket marks the "primary" pulse of maximum KE density magnitude that is initiated at impact and propagates with little dispersion across the half-point, and through to the bottom of the sample with little decrease in magnitude. The wave propagation speed is approximately 10 m/s. Some dispersion is indicated by the widening of the pulse after impact, although the majority of the magnitude of the initial pulse appears to travel with little abatement from the top to the bottom of the sample. The orange rectangle in Fig. 3.3 identifies instances of additional, smaller oscillations that propagate from the top of the sample. This

results in a maximum KE density transmitted of 3.41 kJ/m^3, 20.9x higher than the bistable case in Fig. 3.2.

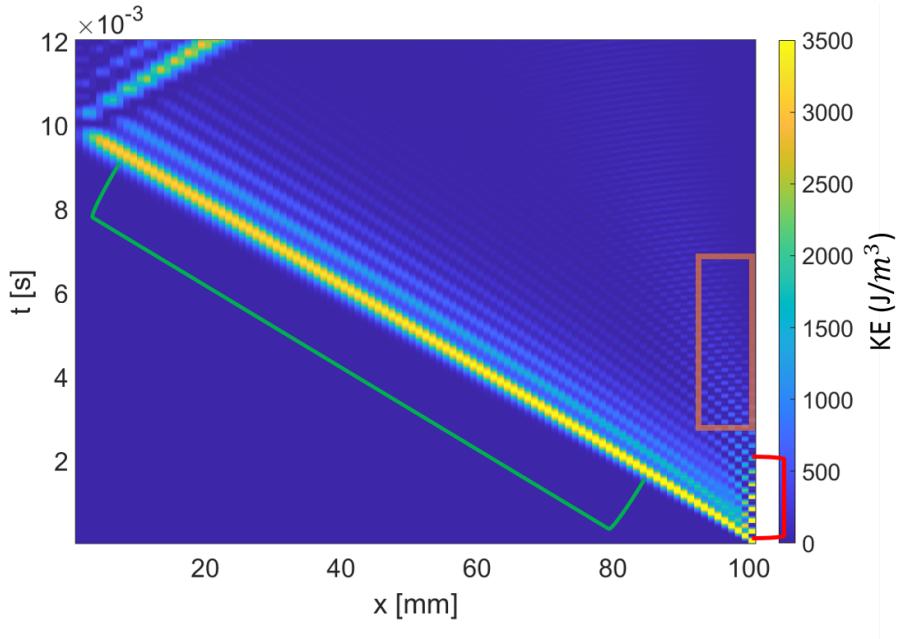

Figure 3.3: There is no damping modeled, and $T_s \approx 1.2$. Noteworthy portions of the diagram are annotated. The red bracket indicates the point of impact, the green bracket notes the primary pulse, and the orange rectangle notes instances of additional smaller oscillations. The maximum KE density transmitted of 3.41 kJ/m^3 is 20.9x higher than the bistable case in Fig. 3.2

Figure 3.4 shows a comparison between the KE density plot for the best performance case in the sweep (panel b) with 20.9x KE ratio at impactor conditions: M_0 and V_0), and a case of medium performance (panel a) shows 4.44x at impactor conditions: $M/M_0 = 10^{-.625}$ and $V/V_0 = 10^{.25}$). A side by side comparison reveals qualitative differences in the behavior; namely longer and more initial solitary wave propagation in Fig. 3.4(b) that transitions to a oscillatory phase which covers more area on the plot than panel a). Specifically, comparing the phenomenon noted by the green and red brackets between both panels highlights the higher number of initial solitary wave-fronts in panel b) that travel a longer spatial distance before transitioning to the oscillatory region as noted by the the orange rectangle. The orange rectangle highlights the oscillatory region, and particularly that this region encompasses a larger area in panel b). Finally the two red circles in Fig. 3.4(a)

show wave-fronts that travel through the half-point of the sample that are all of higher KE density than any of the crossing wave-fronts in panel b). One might note that these red circled wavefronts are "delayed" (i.e they occur later in time than the time it would take for the first solitary wave to reach the half-sample had it continued to propagate), which may stem from dynamic unsnapping of the unit cells.

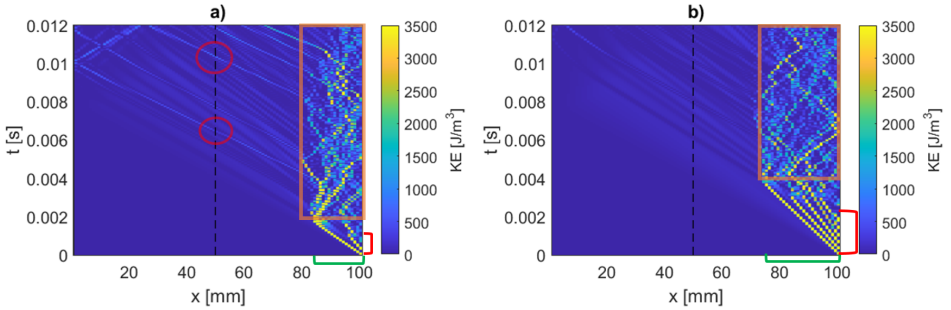

Figure 3.4: a) Impactor conditions: $M/M_0 = 10^{-0.625}$ and $V/V_0 = 10^{0.25}$, resulting in a 4.44x KE ratio. b) Impactor conditions: M_0 and V_0, resulting in a 20.9x KE ratio. The red bracket marks the point where solitary waves are emitted. The green bracket notes the approximate spatial length of the longest solitary wave emission. The orange rectangle marks the dynamic, oscillatory region, and the red circles show high KE density wavefronts that transit the half-sample point. The colorbar maximum scale is reduced to show a comparison of the wavefronts more clearly.

Fig. 3.5 shows a comparison between between the linear and bistable samples at a location in the sweep corresponding to the top left of Fig. 3.1, which also corresponds to the worst performance of the bistable material. At these impactor conditions ($M/M_0 = 10^{-1}$ and $V/V_0 = 10^{0.75}$), a very high amplitude, very short wavelength, solitary wave travels throughout the sample, resulting in 138.6 kJ/m^3 of KE density at the measurement point, which is 11.8x higher than the corresponding linear sample, resulting in a KE ratio of 0.0848x. Defining $M_R = M/m_L$, $M_R = 1.5$ and the formation of a single solitary wave in this instance agrees with previous literature in granular chain impacts favoring single solitary wave formation when impactor and layer mass are closely matched [8,121]. While a secondary solitary wave, and some bistable, oscillatory effects can be seen Fig. 3.5(a), the high level of KE transmission and poor comparative performance appear to result

primarily from the initial solitary wave that transmits throughout the sample. The wave speed of the "primary pulse" of the sample is much faster than the primary pulse of the linear comparative sample. For instance, the solitary wave pulse in Fig. 3.5(a) travels at approximately 16 m/s, while the primary pulse in the comparative (linear) sample (Fig. 3.5(b) travels at approximately 10 m/s. In comparison, in the nominal impact case shown in Fig. 2.8 and Fig. 2.9, the primary pulse of the linear sample travels at approximately the same speed, although the bistable sample (as indicated by the slope of the first solitary wave emission) is less than 10 m/s (such that the solitary wave in the bistable case is actually slower than the linear wavespeed). This difference is indicative of the amplitude dependent wave speed of nonlinear waves. The KE density transmission at N/2 for the linear material was 11.76 kJ/m^3. Additionally, from a comparison of the energy trade off during the simulation (Figs. 3.5(c,d), TE conserved but not shown), it was observed that a much higher amplitude trade-off of system kinetic and potential energy is seen in the bistable system.

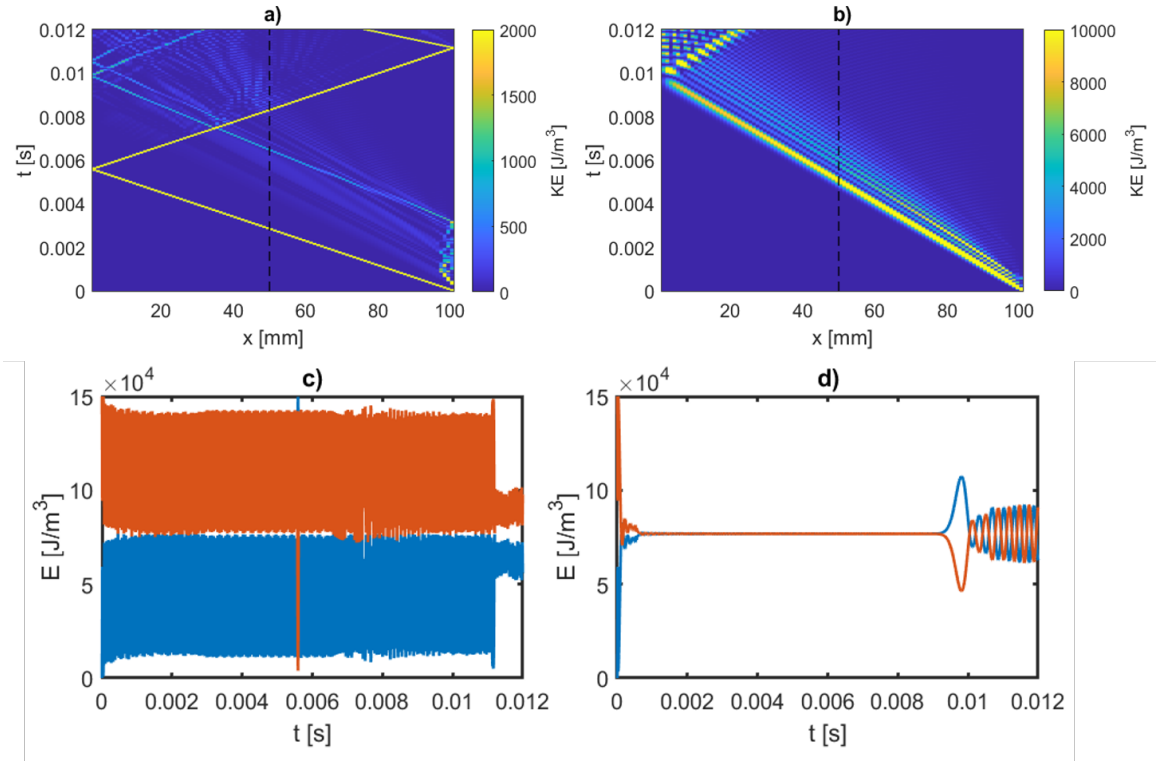

Figure 3.5: (a,c) The KE density and total system energy, respectively, for the bistable sample. (b,d) The KE density and total system energy for the linear comparison sample. This combination of mass and velocity resulted in the worst performance of the chosen sweep, with a KE ratio of 0.0848x. The colorbar scale in a) and b) was reduced to show the wave effects more clearly.

Figure 3.6 shows an example from the region of Fig. 3.1 where both impactor mass and velocity are high, corresponding to the top right quadrant of the plot (high mass, high velocity, where parallels could be drawn with known "shock" cases in granular chains [122]). Impact conditions are: $M/M_0 = 10^{0.75}$ and $V/V_0 = 10^{0.75}$. In Panel A, a "train" of solitary waves is emitted after impact, and appears to continue to do so along the right side of the XT diagram. The KE density magnitude of subsequent emitted waves appears to decrease, and the highest KE density solitary wave, which is also the wave that triggers the maximum KE density value of 354.54 kJ/m^3 is the wave that begins emission at the time of initial impact. In panel b), qualitatively a similar phenomenon of "trains" of waves is seen, also with the strongest magnitude wavefront at the time of initial impact, however, in the case of panel b) we see dispersive effects, as indicated by the broadening of the

pulse in space and time. The maximum KE density in panel b) is substantially less, at 153.01 kJ/m^3. The KE ratio was 0.4316x. Of note: this simulation was run for different simulation durations in each case in order to isolate the analysis to the KE density maximum at the N/2 point that occurred only as a result of the initial wavefront, since in the case of the bistable sample, increasing the runtime past 4.2 ms resulted in a higher maximum KE value after reflection off the bottom of the sample. Thus panel a) was run for 4.2 ms while panel b) was run for 0.012 s.

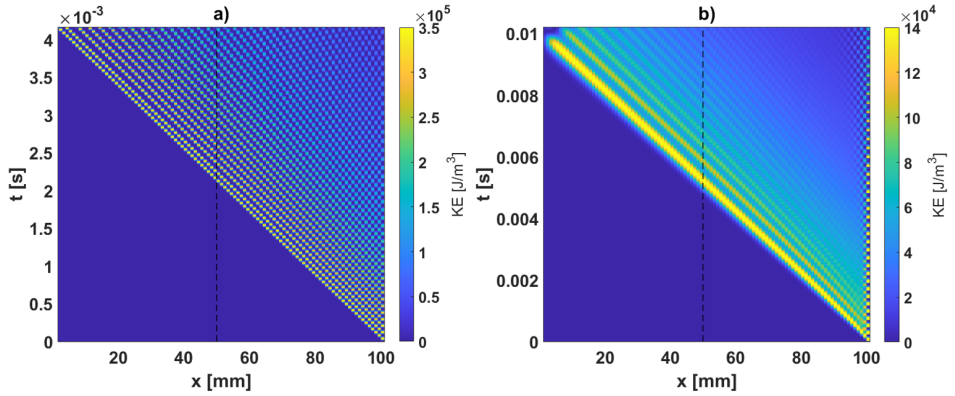

Figure 3.6: , with a) showing the bistable sample, and b) showing the linear comparison sample. The KE ratio was 0.4316x. The colorbar axis was adjusted lower to more clearly show the initial wavefront.

From the analysis of four scenarios with best, good, bad, and "ugly" performance from the given impactor conditions sweep in Sec. 3.1, a few general observations are clear. In the best performing case, multiple solitary waves develop initially, although crucially, these solitary waves transition to a regime prior to the half sample where they oscillate in time, and don't generally propagate past the furthest initial solitary wavefront. In the "good" case, (Fig. 3.3), we see similar phenomenon in terms of initial solitary wave propagation that transitions to the oscillatory region, although the initial solitary "wave train" is shorter, the spatio-temporal area encompassed by the dynamic oscillatory region is less. Additionally, subsequent wavefronts of higher KE density magnitude are emitted that cross the measurement threshold. In the "poor" performing case (Fig. 3.6), we see a train of

much more solitary waves, that continue to emit from the point of impact past the measurement point for the duration in time of the simulation run. Additionally, the first solitary wave has the highest KE density magnitude when it crosses the measurement point. Finally in the worst performing case (*i.e.* "the ugly"), shown in Fig. 3.5, while upon close inspection there are some bistable effects, we primarily see a single solitary wave that dominates the KE density transmission that emits across the sample starting at the initial point of impact. The author notes that all solitary waves observed showed a strain value greater than ε_0, indicative of "transition waves".

3.3 Impact conditions sweep (undamped, long duration simulation)

In this next section, we'll see the effect on the KE ratio performance from a sweep and the effect on individual cases of impact when the simulation duration is increased to $T_s \approx 20.5$. The reader will note that while simulations were run to their full time associated with the T_s value, the maximum KE density values never occurred this late after impact. In order to facilitate presentation of the information, the time axis was shortened in order to display relevant information to the reader.

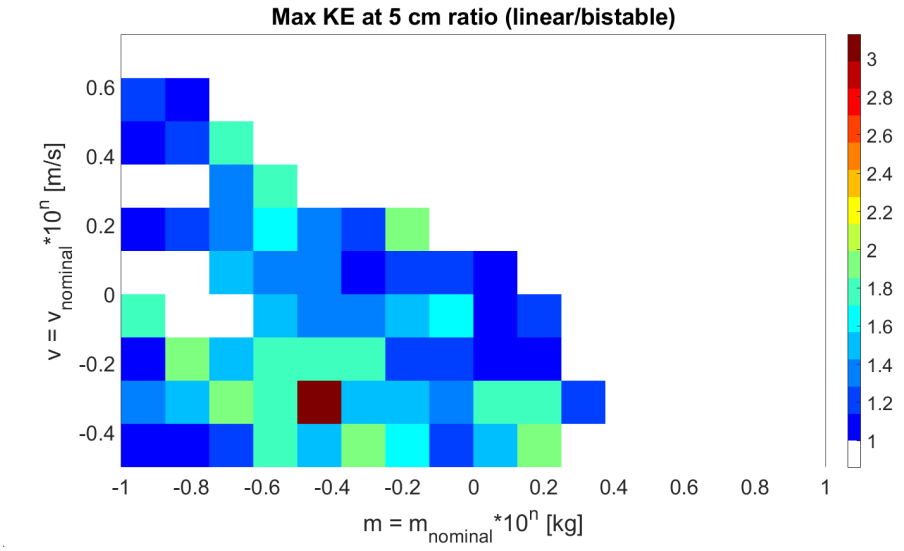

Figure 3.7: Modeled without damping and run for a simulation time $T_s \approx 20.5$. Nominal impactor conditions were $M_0 = 18$g, $V_0 = 3.6$ m/s.

Figure 3.7 shows that significantly lower maximum KE ratio performance in a sweep is indicated when the simulation is run for a long period of time. This lower KE ratio is indicative of complications in the undamped system, likely associated with reflections and interference which occur well after impact. In order to investigate some causes of this, combinations of impactor mass and velocity that were analysed in Sec. 3.2 will be revisited with longer simulation duration for comparison.

Comparison of the worst performing case in the shortened simulation (shown in Fig. 3.5) with the long simulation (Fig. 3.8) and the same impactor conditions ($M/M_0 = 10^{-1}$ and $V/V_0 = 10^{0.75}$) reveals that both bistable and linear samples admit the same maximum kinetic energy density values in both cases, and thus the performance ratio is equally poor. This is because the initial solitary wave emission in the bistable sample is of the highest KE density, which is greater than the strength of interference and reflection that occurs later.

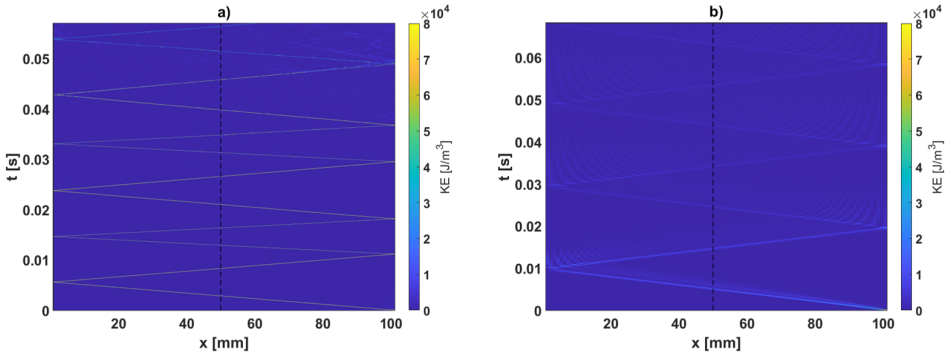

Figure 3.8: a) Bistable sample. b) Linear comparison sample. This combination of mass and velocity resulted in the worst performance of the chosen sweep, with a KE ratio of 0.0848x. The default colorbar values were reduced to show the wavefronts more clearly.

Comparison of impact conditions M_0 and V_0 between the short simulation duration (Fig. 3.2) and long simulation duration (Fig. 3.9) reveals that in the longer simulation runtimes, the linear comparison case yields the same maximum KE density value that it did during the shortened simulation, but the maximum KE density value of the bistable case is much higher. This value occurs well past the initial wavefront, at $t = 0.0168$ s and is circled in red. Energy is released from the oscillatory phenomena occurring within approximately the top 25 mm of the lattice, resulting in a maximum KE density at the half-point of 3.31 kJ/m^3. The emission causing this maximum appears to be either a reflection off the top of the sample, or unsnapping or transition wave behavior. In Fig. 3.9(b), the comparative linear sample is shown. Notably, the maximum KE density is the same in both the short and long duration simulations. As a result, the KE ratio in the longer run case is 1.03x, in comparison to 20.9x in the shortened simulation duration.

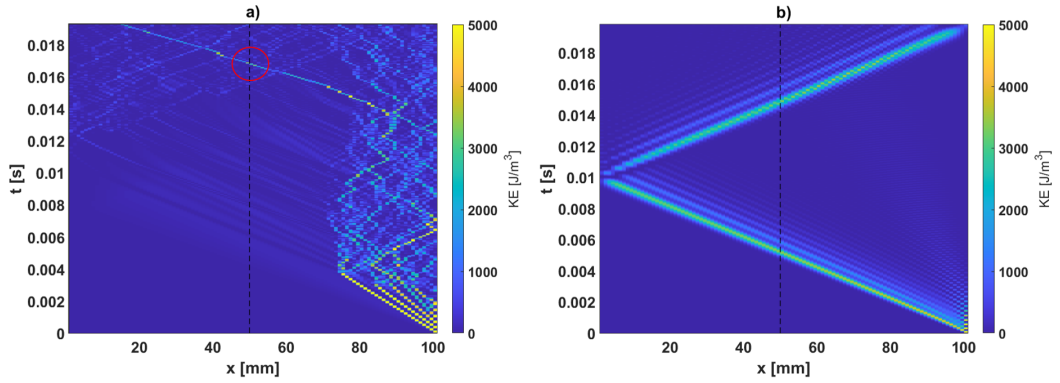

Figure 3.9: The resulting ratio of linear/bistable performance in this longer simulation duration case is 1.03x. a) Bistable sample. b) Linear sample.

Comparison of impact conditions $M/M_0 = 10^{-.625}$ and $V/V_0 = 10^{0.25}$ between the short simulation duration (Fig. 3.3(a)) and long simulation duration (Fig. 3.10) reveals that, similar to the previous example, the linear comparison of the long simulation duration example (Fig. 3.9(b)) has a maximum KE density value (3.83 kJ/m^3) as a result of the initial wavefront ($t = 5.1$ ms). Different from the previous example, however, the bistable sample (Fig. 3.9(a)) has the maximum value after the large magnitude emission from the oscillatory region reflects off the bottom on the sample and returns. This maximum value occurs at $t = 0.02$ s and is 2.15 kJ/m^3, resulting in a KE ratio of 1.78x. Thus, the "medium" performing case from the short simulation duration and the same impactor conditions (Fig. 3.3(a), KE ratio is 4.44x) outperforms the KE ratio of the "best" performing case (1.78x) when the simulation duration is extended.

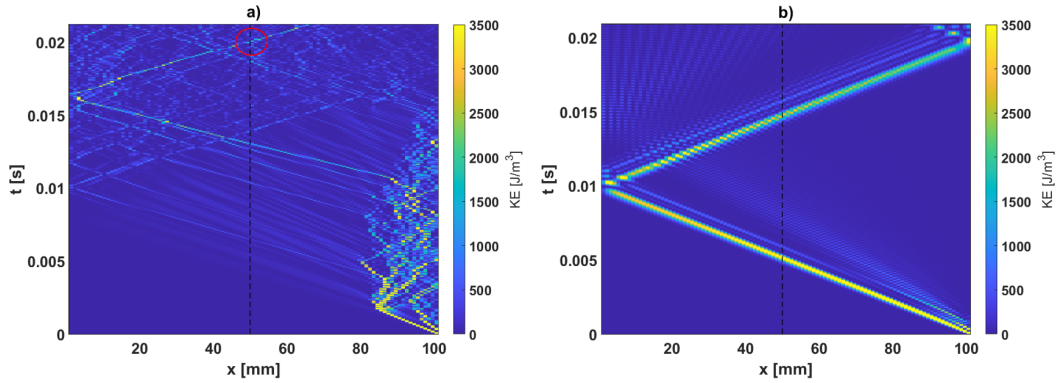

Figure 3.10: Comparison between KE density plots for $N = 100$ lattice, undamped, long simulation duration, at impact conditions: $M/M_0 = 10^{-0.625}$ and $V/V_0 = 10^{0.25}$. The resulting KE ratio was 1.78x. a) Bistable sample. b) Linear sample.

Figure (3.11) shows impactor conditions $M/M_0 = 10^{0.75}$ and $V/V_0 = 10^{0.75}$, which is a region in the upper right corner of the sweep in Fig. 3.7. These are the same impactor conditions as used in Fig. 3.6, but with a longer simulation duration. In Fig. 3.11(a), the bistable sample, the maximum KE density at the half sample point occurs at $t = 0.055$s, resulting from what appears to be the reflection of the first wavefront off of the back of the sample (KE density is 621.06 kJ/m^3). At times after this maximum, multiple interactions of the wave fronts are observed, although none at the half-sample point are of higher KE density magnitude. In Fig. 3.11(b), for the linear sample, the maximum KE density does not occur until the fifth reflection off the sample (counting the initial wavefront as zero), resulting in a KE density of 209.79 kJ/m^3. This is substantially higher KE density than occurs at the first wavefront, and the first time in the example XT diagrams shown where a higher KE density magnitude in a linear sample occurs after the initial wavefront. The resulting KE ratio is 0.3378x.

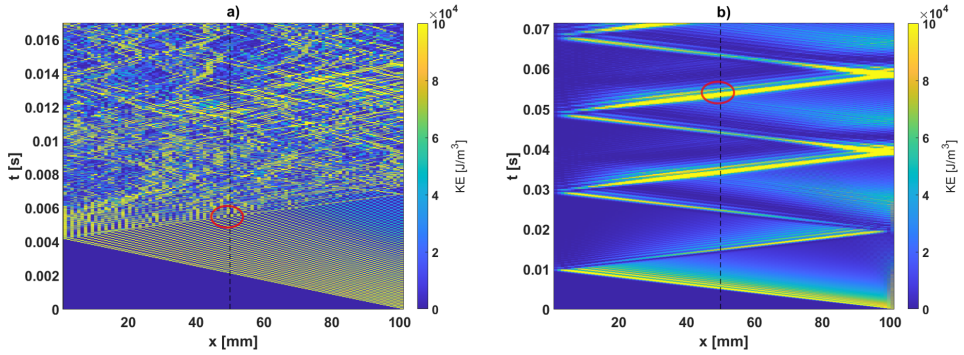

Figure 3.11: Comparison between KE density plots for $N = 100$ lattice, undamped, long simulation duration, at impact conditions: $M/M_0 = 10^{0.75}$ and $V/V_0 = 10^{0.75}$ (high mass, high velocity). The resulting KE ratio was 0.3378x. a) Bistable sample. b) Linear sample.

Now, we look at Fig. 3.12, the case that performed the best during the long simulation duration sweep. The impact conditions were: $M/M_0 = 10^{-0.5}$ and $V/V_0 = 10^{-0.375}$, and resulted in a KE ratio of 3.13x, the best performance seen in the undamped, long duration simulation sweep. In Fig. 3.12(a), the KE density maximum of the first wavefront, (73.99 J/m^3) occurs at $t = 5$ ms, while the total maximum of 92.86 J/m^3 occurs at $t = 0.168$ s, and is not shown in the frame. A small concentration of KE density near the impact point is observed, however, the rest of the case qualitatively is unremarkable. Fig. 3.12(c), shows the results of the linear sample, where the maximum KE density at the half sample of 290.4 J/m^3 occurs at $t = 5.1$ ms, corresponding to the first wavefront.

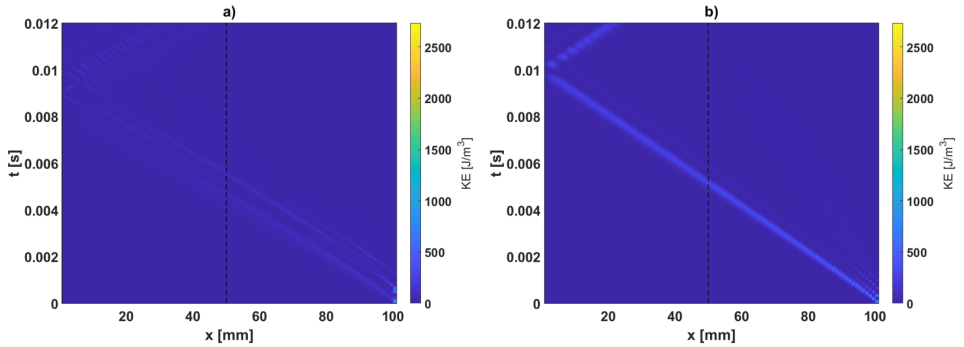

Figure 3.12: Impactor mass was $M/M_0 = 10^{-0.5}$ and velocity was $V/V_0 = 10^{-0.375}$ in this extended simulation duration, $N = 100$ undamped case. The KE ratio was 3.13x, the best of the simulation sweep. a) Bistable sample. b) Linear sample.

The following general observations are noted from the examples in this section. First, in comparison with the shortened simulation duration case, the longer simulation duration examples do not perform as well. This is indicated by the 6.7x worse performance, if you compare the best performing bistable case from Fig. 3.1 with the best performing case from Fig. 3.7. Second, the worst performing case ($M/M_0 = 10^{-1}$ and $V/V_0 = 10^{0.75}$) performed equally poorly (KE ratio is 0.0848x) in both short and long duration simulations. It is possible that this behavior is related to the singular solitary wave that appears to propagate though the sample in both cases, with little apparent qualitative difference as a result of subsequent reflections in the longer simulation case. Third, in three of the four comparison cases, the maximum KE density at the half point in the linear sample occurred during the initial wavefront, and thus this maximum value for the linear comparison sample is the same in both the short and the long simulation time scenario. The only exception to this is at impactor conditions $M/M_0 = 10^{0.75}$ and $V/V_0 = 10^{0.75}$, where the maximum occurs five reflections after the initial wavefront. In contrast, for the bistable cases shown, all of the maximums in the long duration simulations occur after the initial wavefront, with the exception of impactor conditions ($M/M_0 = 10^{-1}$ and $V/V_0 = 10^{0.75}$), which was previously mentioned.

3.4 Damped analysis

In this section, the effect of the addition of a predetermined amount of damping to the simulation is assessed. While a detailed analysis of the effect of changing damping on maximum KE density ratio performance is conducted in Sec. 6.5, in this section, an amount of damping in which "good" performance was observed is used. The simulation setup is identical to those used in Sec. 3.3, with the exception of including whole sample damping (η_s) in the amount of 0.00164 Ns/m. The relationship between η_s and interlayer damping η is: $\eta_s = \eta/N$.

The result of the long simulation duration ($T_s \approx 20.5$) sweep is shown in Fig. 3.13, and the short simulation duration sweep (0.012 s) is shown in Fig. 3.14. As was the case in the previous section for the undamped sweeps, the shorter

simulation duration in the damped sweeps resulted in generally better performance as well. This was hypothesized to be due to interactions past the initial wavefront (reflection, focusing, etc). However, while the performance was still better in the shortened simulation for the damped case, the performance difference between the long and short duration simulations was much smaller than in the undamped case. Thus, for this section, while both short and long simulations were conducted, the XT diagrams of comparison were shown for the long duration simulations. In instances where the maximum transmitted kinetic energy density occurs later in the simulation, this is noted.

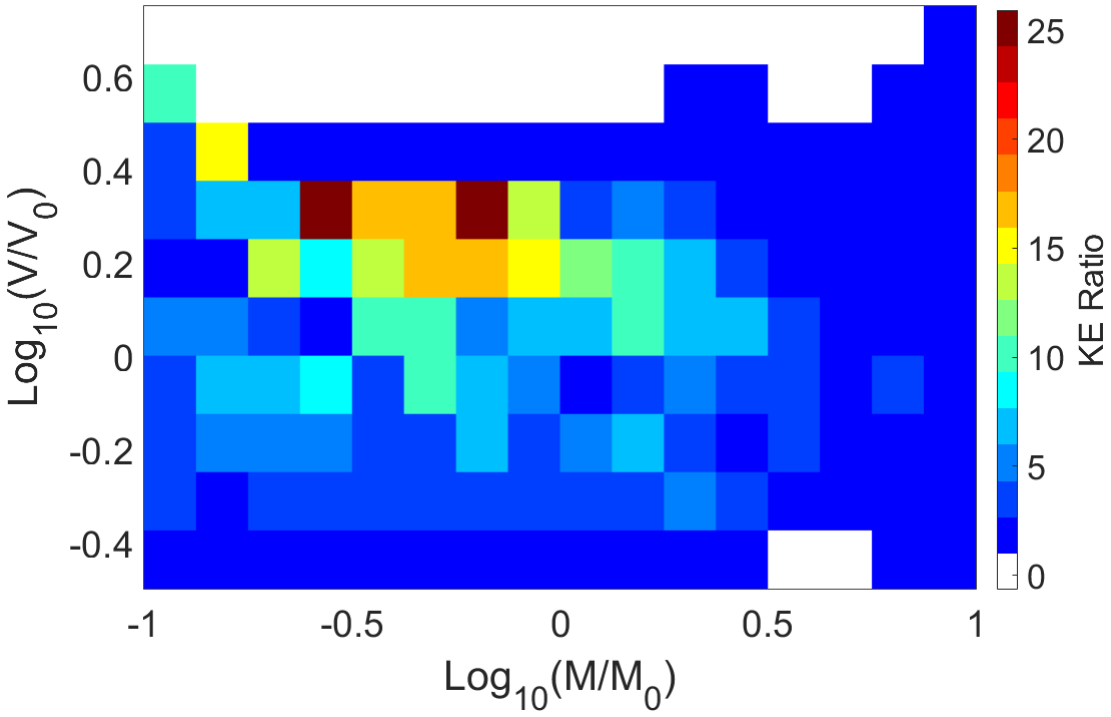

Figure 3.13: Maximum KE ratio of a $N = 100$ bistable lattice compared to a material with linear constitutive response, for simulation duration $T_s \approx 20.5$, and $\eta_s = 0.00164$ Ns/m. The maximum KE ratio was 25.91x.

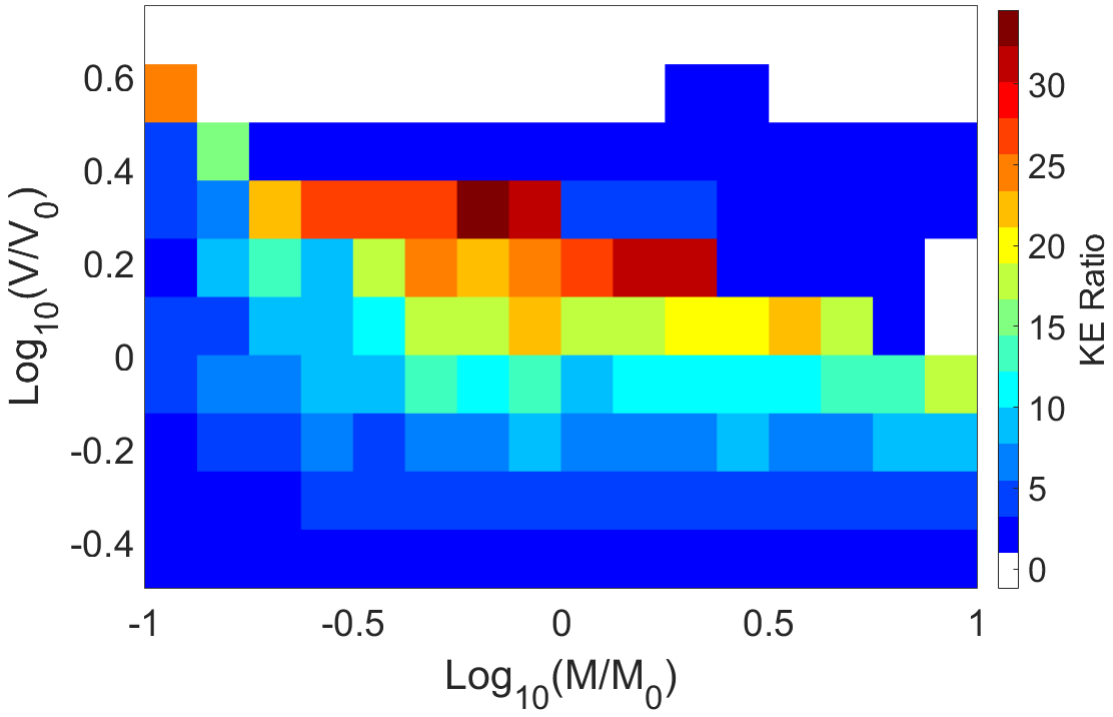

Figure 3.14: Maximum KE ratio of a $N = 100$ bistable lattice compared to a material with linear constitutive response, for simulation duration $T_s \approx 1.2$, and $\eta_s = 0.00164$ Ns/m. The maximum KE ratio was 34.58x.

Figure 3.13 shows the long simulation duration damped sweep, where the maximum KE ratio was 25.91x. This ratio exceeds that of both of the undamped cases (long and short duration simulation). Figure 3.14 shows the short simulation duration damped sweep, where the maximum KE ratio was 34.58x, the highest yet. Individual impactor combinations from the sweeps of interest will be analyzed in the damped scenarios in a similar manner as they were analyzed in the undamped scenarios.

Figure 3.15 shows the case corresponding to the top left corner of the phase plot, representing impactor mass $M/M_0 = 10^{-1}$ and impactor velocity $V/V_0 = 10^{0.75}$. This represents the worst performance of the damped sweep from Fig. 3.13. It is also the same case that resulted in the worst performance from both undamped sweeps (Fig. 3.5 and Fig. 3.8). Figure 3.15(a) shows the bistable sample and Fig. 3.15(b) shows the linear sample. The maximum values in both panels are

seen as the initial wavefront crosses the middle of the sample. These values are 47.63 kJ/m^3 at $t = 3.3$ ms for the bistable sample, and 9.88 kJ/m^3 at $t = 5$ ms for the linear comparison. The KE density transmission values in each panel are less (better) than the values observed in the two previous undamped examples at the same impact conditions, which is expected due to the addition of damping taking away some energy from the system. However, while the performance of this system is still the worst of the sweep, the KE ratio of $0.2073x$ is better than the undamped cases' ratio of $0.0848x$.

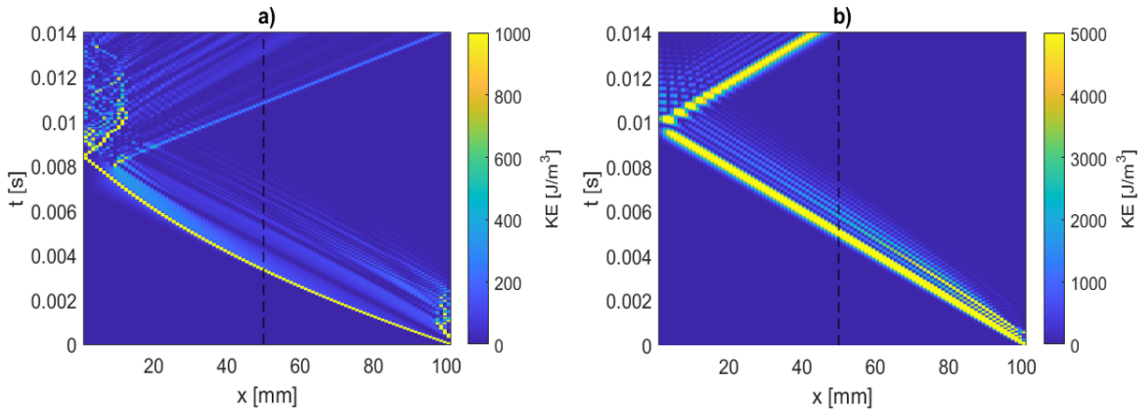

Figure 3.15: Comparison between KE density plots for $N = 100$ lattice, damped, long simulation duration, at impact conditions: $M/M_0 = 10^{-1}$ and $V/V_0 = 10^{0.75}$ (low mass, high velocity). The resulting KE ratio was 0.2073x. a) Bistable sample. b) Linear sample.

Additionally, there are several qualitative and quantitative differences in the damped case which are worthy of note. First, in Fig. 3.15(a), the primary solitary wave emission increases in slope as it propagates down the sample (moving from right to left), representing a slowing wavespeed as the pulse propagates. This is indicative of the amplitude dependent wavespeed of nonlinear waves, with amplitude decreasing as a result of the addition of damping. Second, while the two undamped examples at the same impactor conditions reflect a strong solitary wave back once the initial pulse hits the floor of the sample, the damped case does not. While a smaller amplitude solitary type wave is seen (beginning at approximately $t = 8$ ms and 16 mm, traveling rightward, at the impact point of the first pulse

with the bottom of the sample), we see the dynamic, oscillatory tail of snapping and unsnapping, which is not seen in the undamped cases. This could be a result of the addition of damping dissipating enough energy that the dynamic oscillatory region develops, rather than resulting in another solitary wave reflection.

Figure 3.16 shows the example of the impact conditions which resulted in the best performance in this section: $M/M_0 = 10^{-0.625}$ and $V/V_0 = 10^{0.25}$. The KE ratio was 25.9x. Figure 3.16(a,c) shows the bistable sample, and Fig. 3.16(b,d) shows the linear. The spring stretch is shown in Fig. 3.16(c,d). The maximum KE density at the half point in Fig. 3.16(a) is 126.35 J/m^3 at $t = 5.7$ ms. In Fig. 3.16(c), the maximum value is 3.27 kJ/m^3 at $t = 5.1$ ms.

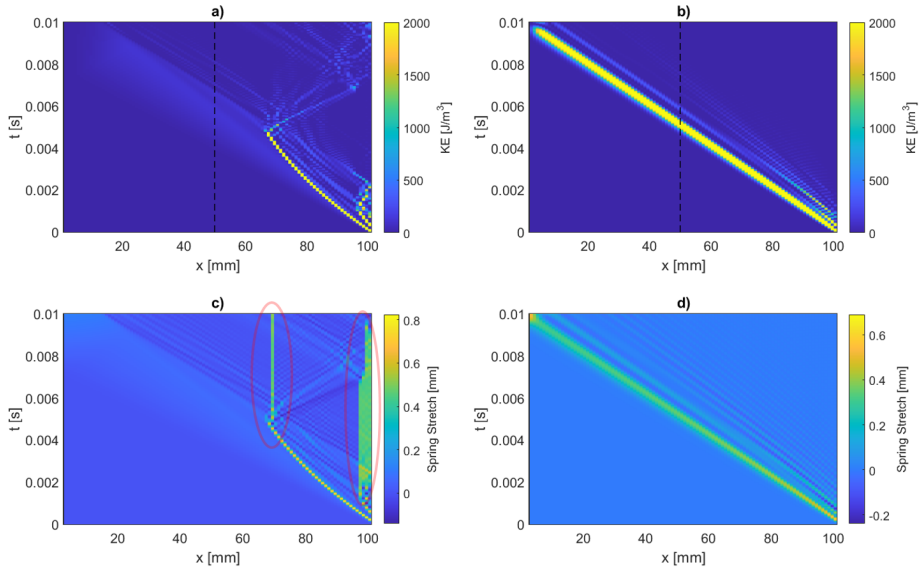

Figure 3.16: Comparison between KE density and spring stretch plots for $N = 100$ lattice, damped, long simulation duration, at impact conditions: $M/M_0 = 10^{-0.625}$ and $V/V_0 = 10^{0.25}$. The resulting KE ratio was 25.9x. a,c) Bistable sample. b,d) Linear sample.

Qualitatively, some similarities are observed when Fig. 3.16(a) is compared with other cases with high performance ratios. We see an initial solitary wavefront that transitions (in time) to the dynamic, oscillatory region prior to crossing the halfway point of the sample. Additionally, as indicated by the maximum KE density value in Fig. 3.16(a) being observed at initial wavefront passage ($t =$

5.1 ms), we don't observe large enough releases of energy from the oscillatory region to exceed this measurement. Furthermore, in Fig. 3.16(c) the two red ovals show regions from the spring stretch plot where we have a permanent (or semi-permanent) stretch or compression of a particular layer. This is indicative of snapping or unsnapping of a layer and remaining in that state, aided by damping. Other noteworthy differences in this damped, bistable case include the changing wavespeed of the wavefront, and what appears to be smaller oscillatory region than what was seen in the higher performing undamped examples.

Figure 3.17 shows the result of impactor conditions: M_0 and V_0. Figure 3.17(a,c) shows the bistable sample and Fig. 3.17(b,d) shows the linear sample: the KE ratio is 6.04x. The maximum KE density of 497.71 J/m^3 occurs at $t = 0.0305$ s, which is much later than the first wavefront, and occurs as a result of what appears to be reflections off the top of the sample. The maximum KE density of the simulation was limited to the shortened simulation duration was 177.73 J/m^3 at $t = 9.9$ ms. Both of these maximum values are circled in red in Fig. 3.17(a). The maximum of the linear sample in Fig. 3.17(b) occurs at the initial wavefront (3004.48 J/m^3 at $t = 5.2$ ms) in either simulation duration, thus, the KE ratio increases to 16.9x if only the first wavefront is considered. Figure 3.17 panels (c,d) represent the same long duration simulation shown in panels (a,b), with the exception that the time axis is adjusted to a maximum of 12 ms.

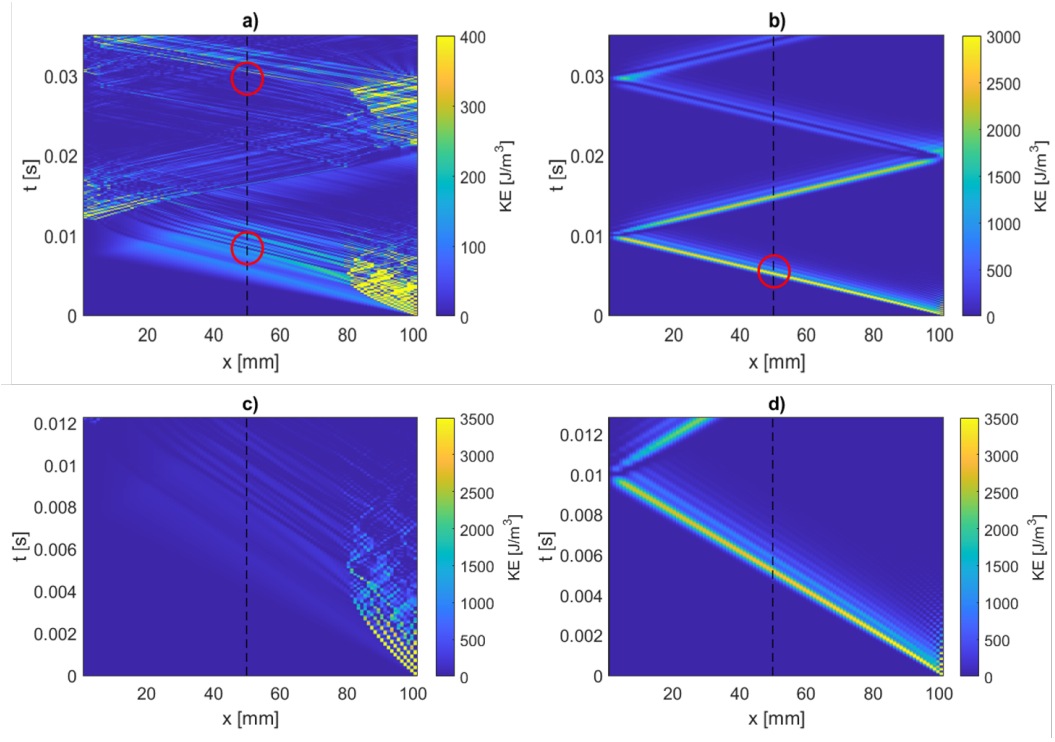

Figure 3.17: Of note, a) and c) show the same simulation for the bistable sample, with different time ranges. b) and d) show the corresponding time ranges for the linear sample. The colorbar axis were adjusted lower than the maximum value in order to see the KE transmission across the half sample more clearly.

Comparisons between the undamped short and long simulation duration cases yield some interesting observations. Compared to the undamped, long simulation duration case (Fig. 3.9), while the damped performance is much better, in both cases kinetic energy release or reflection that occurs well after the initial wavefront results in the maximum KE density value at the half sample. In comparison to the short duration, undamped simulation (Fig. 3.4(b)) the undamped case actually outperformed the damped case. Qualitative comparison of the two cases (Fig. 3.17(c) for the damped, and Fig. 3.4(b) for the undamped) reveals the following: both cases initially emit solitary waves immediately at impact, which are initially qualitatively similar, with the exception of the damped case having a changing wavespeed as indicated by changing slope. However, the damped case transitions to the oscillatory regime earlier (approximately 3 ms for the initial wave in Fig. 3.17(c) compared to approximately 4 ms in Fig. 3.4(b). This regime lasts for a

shorter period of time for the damped case; lasting approximately 4 ms in Fig. 3.17(c), compared to approximately 8 ms in Fig. 3.4(b), with the same colorbar settings shown. This suggests that possibly there may be some performance benefit in the lengthening of the time in this oscillatory regime. It is also possible that the nominal impactor conditions are not matched as well for maximum KE ratio in the damped example as they are in the undamped example.

Figure 3.18 shows impactor conditions $M/M_0 = 10^{0.75}$ and $V/V_0 = 10^{0.75}$, which is a region in the upper right corner of the sweep in Fig. 3.13. The KE ratio was 0.922x. The max KE density in the bistable sample (Fig. 3.18(a)) was 186.35 kJ/m^3 at t= 2.3 ms, at the initial wavefront. The linear sample had a maximum value of 136.72 kJ/m^3 at the initial wavefront, although the simulation maximum of 171.876 kJ/m^3 for this sample did not occur until the 3rd reflection at $t = 0.0342$ s.

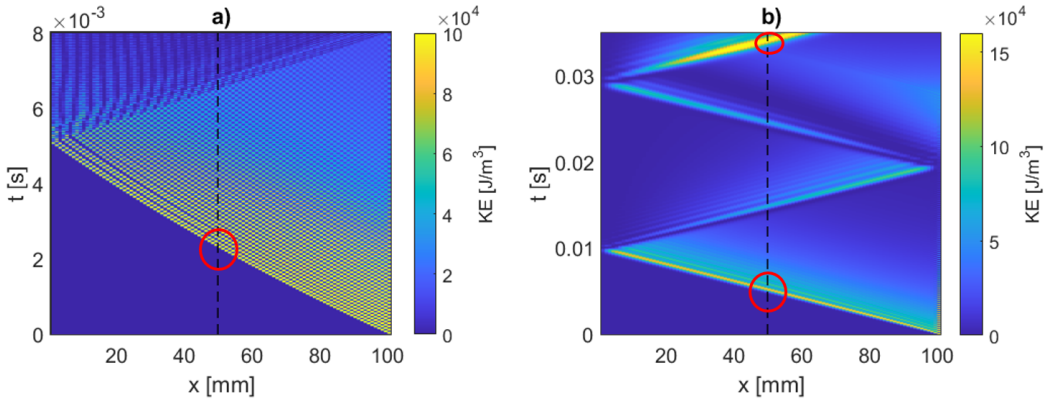

Figure 3.18: The resulting KE ratio was 0.922x. a) Bistable sample. b) Linear sample. The red circles note the maximums at the half-sample. The simulation maximum in b) is the red circle at the top of the plot and the lower red circle is the maximum that occurs during the initial wavefront.

A comparison to the undamped cases of the same impactor conditions (short simulation duration undamped example was Fig. 3.6 and the long simulation duration undamped example was Fig. 3.11), revealed the following. Comparing Fig. 3.18 to Fig. 3.6, qualitatively both panels of each case appear similar, (with exception of wavefront curvature), in that the bistable case has a series of solitary waves, and the linear cases shows a dispersive wavefront. At the half-height measurement

point, each of the damped cases have less KE density that passes in comparison to their undamped counterparts, which is at least partially a result of the damping term dissipating energy within the initial wavefront, but also due to the complex interplay between bistable performance and damping, discussed further in Sec. 6.5. Comparing Fig. 3.18 with Fig. 3.11, the following is noted. While Fig. 3.18(a) has a maximum value at the initial frontal passage, Fig. 3.11(a) has a maximum after the first reflection. Additionally, comparing Fig. 3.18(b) with Fig. 3.11(b) (the linear examples), the maximum value is observed after a different number of reflections: the 3rd reflection for the damped example, then the 5th for the undamped.

Figure 3.19 represents impactor conditions $M/M_0 = 10^{-0.5}$ and $V/V_0 = 10^{-0.375}$. The maximum KE ratio was 3.59x. The maximum KE density of the bistable sample (Fig. 3.19(a)) was 69.66 J/m^3, and the maximum KE density of the linear sample (Fig. 3.19(b)) was 250.35 J/m^3. Comparing this example to Fig. 3.12, which represented the maximum performance (KE ratio is 3.13x) of the long simulation duration undamped sweep, the following is noted. Qualitatively, the initial wave-fronts from the bistable undamped and damped examples are quite similar. The most notable difference, however, is that while the maximum value in the undamped case is far later in the simulation, in the damped case the maximums occurs within the initial wavefront (for both the linear and bistable cases).

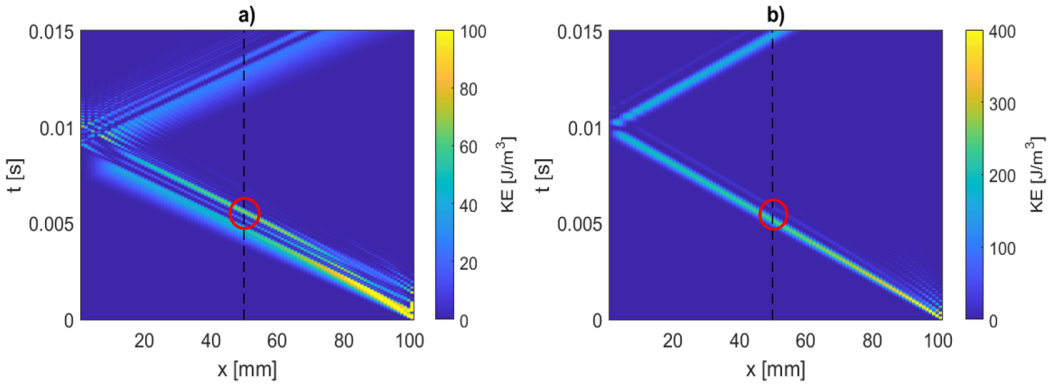

Figure 3.19: The red circles show the areas of highest KE density at the half-sample point, which occurs on both panels at the initial wavefront.

Chapter 4

Performance as a function of impactor mass and velocity (N=100, maximum strain limited)

For simplicity, examples shown up to this point were not constrained to a strain limit. As a result, particularly in cases of where a sample was simulated at high energy impact conditions, the strain between the individual layers in the DEM was able to exceed one. In order to increase the realism of the simulation, examples in this chapter are presented to show the effect on the results when strain between the individual layers was limited to less than or equal to one. Indeed, better modeling of the stiffness resulting from unit-cell self contact would be a more accurate next step, however this strain limitation provides an accessible metric for probing when self-contact and sample compaction will occur. Data will be presented in the same order that it was in the previous chapter: short simulation duration undamped simulations, followed by long simulation duration undamped, then finally a combined section of short and long duration damped simulations (in order to focus on relevant features in the results).

4.1 Impact conditions sweep (undamped, short duration simulation)

Figure 4.1(a) shows the maximum KE ratio resulting from a short duration (simulation duration was 0.012 s, $T_s \approx 1.2$), $N = 100$, undamped sweep. Figure 4.1(b) shows the maximum layer strain experienced at any point in the simulation for the same impactor conditions. Additionally, the red diagonal line indicates the energy required to collapse every layer within the top half of the sample (from $N = 100$ to $N = 50$) to a strain value of ε_{sc}. The calculation assumes all impactor KE is converted to PE, and the idealization that the top half of the sample absorbs all the KE to PE, without transmission to layers less than $N = 50$. The red line in Fig. 4.1(b) gives an additional metric to indicate sub-optimally high impactor energy for the lattice, and as seen in the diagram, occurs generally prior to the observance of maximum lattice strain values of 1. Of note, stress corresponding to ε_{sc} can be calculated by substituting ε_{sc} for ε in Eq. 2.7. Impactor conditions where layer strain exceeds 1 at any point are excluded from XT diagram analysis in this section. The maximum KE ratio was 20.9x.

The performance where a strain value of 1 was exceeded were in regions of the sweep where performance was poor anyways. Thus there were not significant differences in performance benefits between the strain limited case shown, and the sweep shown without the strain limitation in Fig. 3.1. It is noteworthy however, that when looking at lower energy maximum impactor conditions that define the strain limited regime, at low mass and high velocity we still see few or singular solitary wave formation, and high mass and high velocity we see trains of solitary waves. These two examples are shown in Fig. 4.2 and Fig. 4.3 below.

Figure 4.2 shows impactor conditions: $M/M_0 = 10^{-0.75}$ and $V/V_0 = 10^{0.5}$ (low mass and high velocity), which represents the conditions of the worst KE ratio performance (KE ratio = 0.13x) in the strain limited sweep in Fig. 4.1. At these impactor conditions, a very high amplitude, very short wavelength, solitary wave travels throughout the sample, resulting in 63.93 kJ/m^3 of KE density at the half sample point, in comparison to 8.53 kJ/m^3 of KE density in the linear sample.

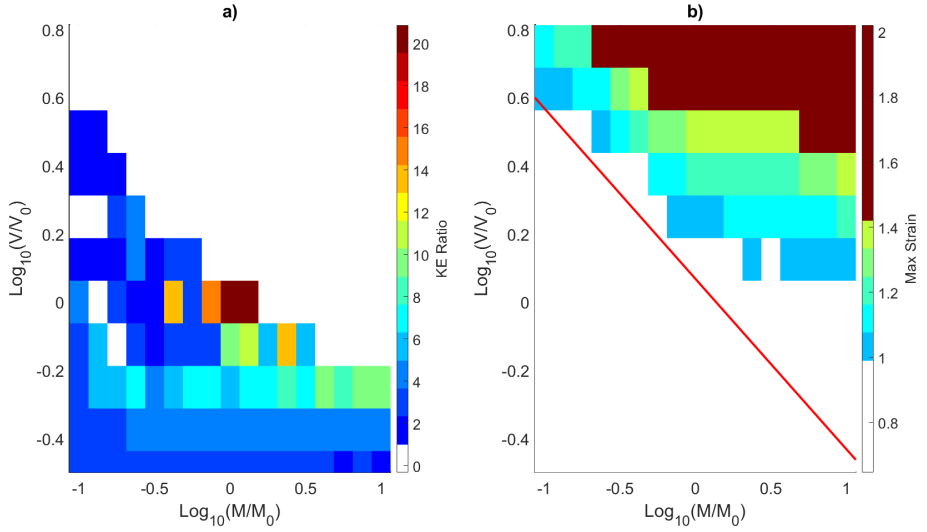

Figure 4.1: a) Maximum KE ratio for the given impactor conditions. b) Maximum layer strain. Note the minimum value in the colorbar legend in a) was reduced such that the transition from white to blue occurred at a value of 1. The red diagonal line denotes the idealized impactor KE required to collapse the first half of the sample (from $N = 100$ to $N = 50$) to ε_{sc}.

While some bistable, oscillatory effects can also be seen in the bistable sample (Fig. 4.2(a)), the high level of kinetic energy transmission and poor comparative performance appear to result primarily from the initial solitary wave transmission.

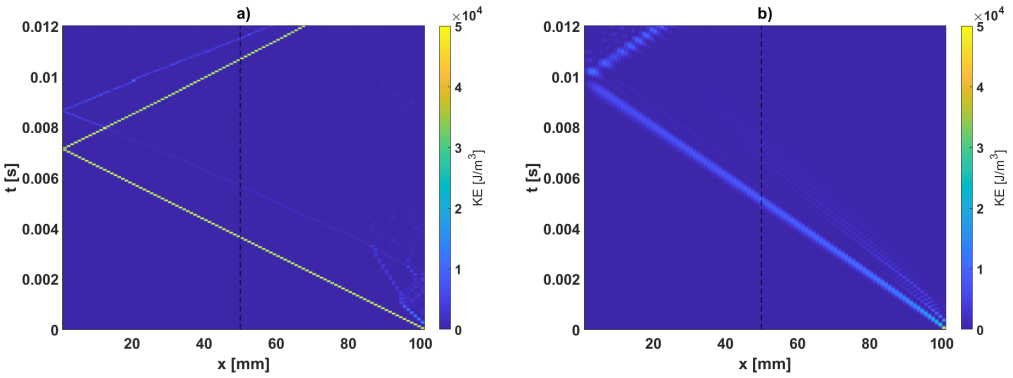

Figure 4.2: KE density plots for impactor conditions $M/M_0 = 10^{-0.75}$ and $V/V_0 = 10^{0.5}$ (low mass, high velocity). a) Bistable KE density. b) Linear KE density. The KE ratio was 0.13x.

Figure 4.3 shows a sample impacted at conditions: $M/M_0 = 10^1$ and V_0, which is representative of the highest velocity at the maximum impactor mass in Fig. 4.1 prior to the layer strain limit being reached. The KE ratio was 0.31x. The bistable sample (Fig. 4.3(a)) transmits a maximum KE density of 15.48 kJ/m^3 at the half sample point at $t = 8.2$ ms. Qualitatively, in Fig. 4.3(a), a series of solitary waves is emitted after impact, and appears to continue to do so initially, along the right side of the diagram. At approximately 4 ms, a higher velocity and higher amplitude solitary wave is emitted which causes the maximum KE density value at the half sample point. Figure 4.3(b) shows the linear sample: here, multiple linear waves are seen as the large mass continues to compress the sample. A KE density at the half sample of 50.02 kJ/m^3 occurs at 5.2 ms, which is during the first wavefront. Additionally, in Fig. 4.3(b), dispersive effects are seen, as indicated by a broadening of the pulse in space and time.

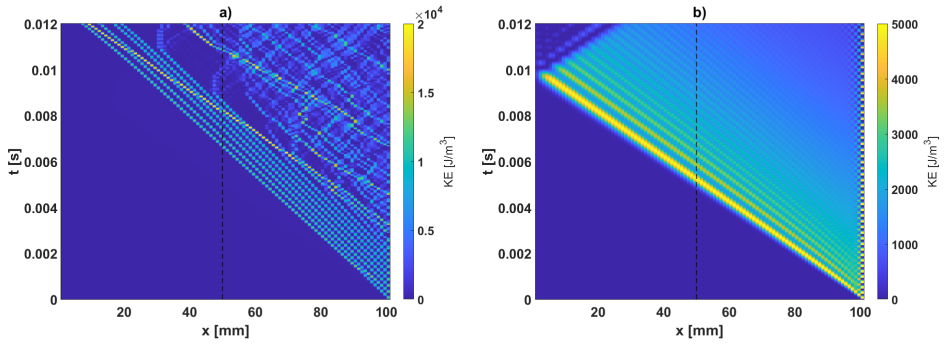

Figure 4.3: KE density plots for impactor conditions $M/M_0 = 10^1$ and V_0 (high mass, high velocity). a) Bistable KE density. b) Linear KE density. The KE ratio was 0.31x.

4.2 Impact conditions sweep (undamped, long duration simulation)

In this section, all the conditions are the same as Sec. 4.1, with the exception of the simulation duration, which is increased to 0.2049 s. Figure 4.4(a) shows that significantly lower maximum KE ratio performance (maximum KE ratio is 3.12x, at impact conditions: $M/M_0 = 10^{-0.5}$ and $V/V_0 = 10^{-0.375}$) is indicated when the undamped simulation is run for a longer period of time. This level of performance is consistent with Sec. 3.3, where a similar sweep was performed without regard for limiting the maximum layer strain value. Figure 4.4(b) shows the maximum layer strain experienced at the same impactor conditions described for panel a). Additionally, the red diagonal line indicates the energy required to collapse every layer within the top half of the sample (from $N = 100$ to $N = 50$) to a strain value of ε_{sc}, as described in Sec. 4.1. As before, cases with strains greater than unity are excluded from further discussion.

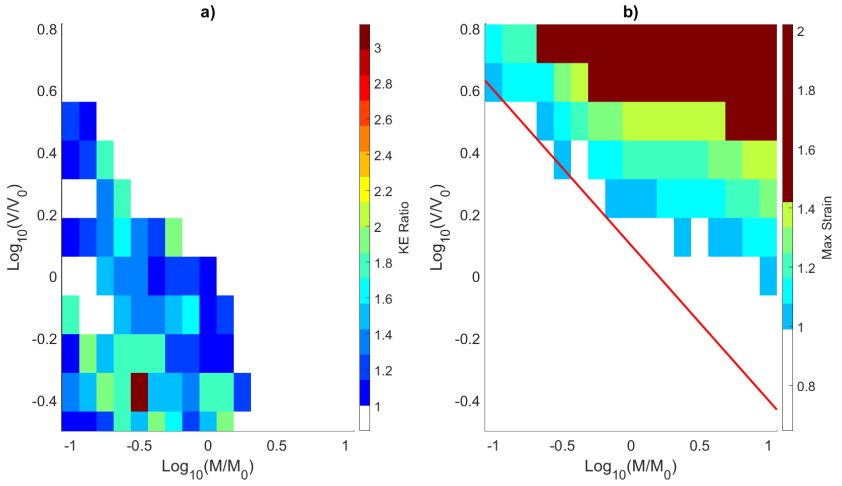

Figure 4.4: a) Maximum KE ratio. b) Maximum layer strain. The red diagonal line denotes the idealized impactor KE required to collapse the first half of the sample (from $N = 100$ to $N = 50$) to ε_{sc}. The maximum KE ratio of 3.12x occurred at impact conditions: $M/M_0 = 10^{-0.5}$ and $V/V_0 = 10^{-0.375}$

4.3 Damped analysis

Now we'll look at some updates to the simulation as a result of adding damping and limiting our results to only those cases where the maximum layer strain is less than one. Again, results of short and long simulation duration scenarios are shown. Figure 4.5 shows the long simulation duration damped sweep. In Fig. 4.5(a) the maximum KE ratio is shown as a function of impactor conditions. In Fig. 4.5(b), the maximum layer strain for the given impactor conditions are shown. The maximum KE ratio was 25.91x, the simulation duration was 0.2049 s ($T_s \approx 21$), and η_s of 0.00164 Ns/m was modeled. Of note, the maximum KE ratio value in this sweep (25.91x) is the same value found when the maximum layer strain limit was not imposed. This is because the KE ratio was poor in areas with maximum layer strains greater than one.

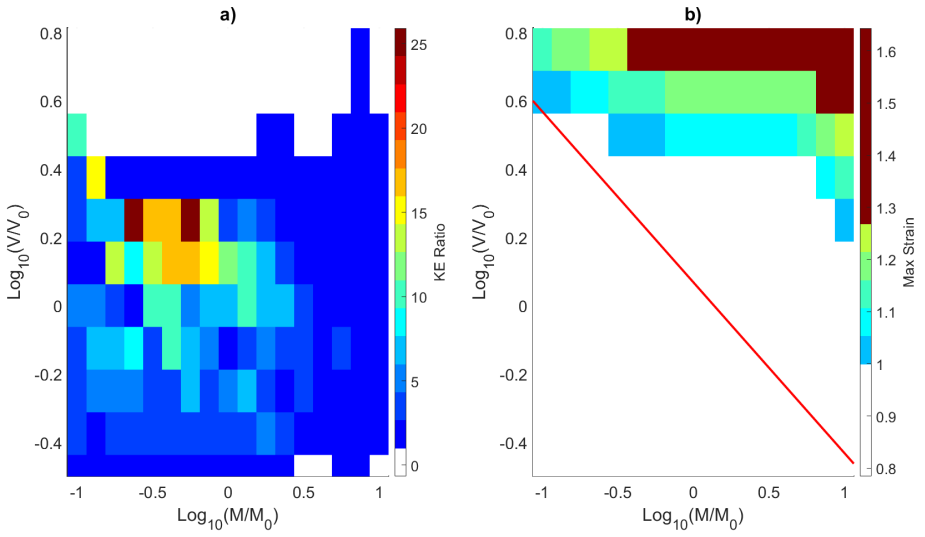

Figure 4.5: a) Maximum KE ratio. b) Maximum layer strain. The red diagonal line denotes the idealized impactor KE required to collapse the first half of the sample (from $N = 100$ to $N = 50$) to ε_{sc}.

Figure 4.6 shows the short simulation duration damped sweep. In Fig. 4.6(a) the maximum KE ratio is shown as a function of impactor conditions. In Fig. 4.6(b), the maximum layer strain for the given impactor conditions are shown. The maximum KE density ratio was 34.58x. Similar to the long duration simulation

above, the maximum KE ratio of the best performing conditions was not affected by the maximum strain limitation, because in this simulation the KE ratio was poor in areas with maximum layer strains greater than one.

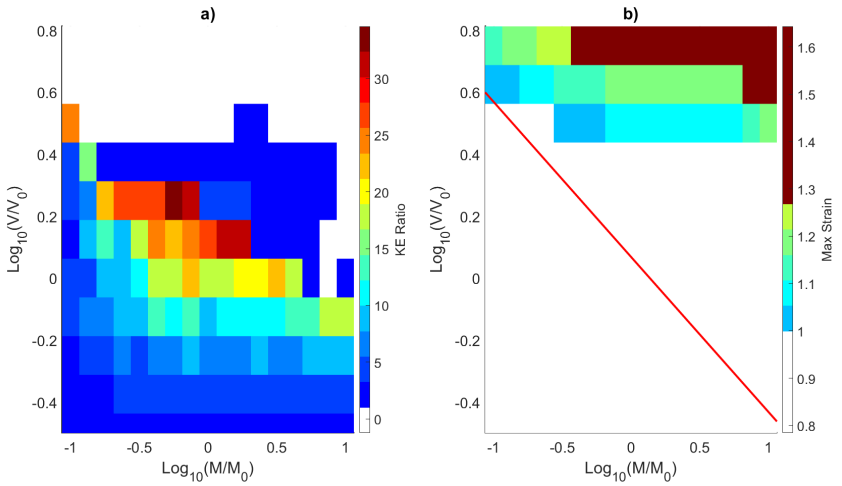

Figure 4.6: a) Maximum KE ratio. b) Maximum layer strain. The red diagonal line denotes the idealized impactor KE required to collapse the first half of the sample (from $N = 100$ to $N = 50$) to ε_{sc}.

There were not significant differences in the performance benefit in the damped $N = 100$ simulations when the strain limitation was imposed.

Chapter 5

Performance as a function of number of layers in a finite size sample

The results shown so far have been modeled with $N = 100$ layers. This chapter explores the relationship between maximum KE ratio performance and the N value chosen within a chosen (uniform) sample size. It is important to note that there appears to be a correlation between not only N value and performance, but also, the optimum damping value to maximize performance for a given N value as well. Thus, in this chapter, the same sample damping value from Sec. 3.4 of 0.00164 Ns/m was set fixed, and N was varied. Combinations of short simulation time (0.012 s) and long simulation time (0.2049 s) were run in order to assess where the KE transmission driving the performance ratio was seen. Conservative (i.e. undamped) simulations were also conducted that showed improved maximum performance with increasing N. These simulations were run in order to verify the effect wasn't merely a result of damping, although for the sake of brevity they are not shown.

Figure 5.1 shows the results of a series of sweeps from 0.2049 second (long) simulation runs. Each discreet data point represents the maximum KE ratio that was achieved from a sweep of plus and minus one order of magnitude from nominal impactor mass and plus and minus one-half order of magnitude from nominal

impactor velocity for the given N value noted (wherein the comparative linear material used for the ratio has the same number of layers as the bistable sample, and the same interlayer damping η). It appears that particularly within the range of $N = 50$ and $N = 200$ there is a strong correlation between maximum KE ratio performance and higher N value, thus this was the particular area that was focused on. However, it is also noted that as the N value is changed, the "landscape" of the region (*i.e.* the region in mass and velocity space where the performance maximum occurs) shifts (which is discussed further in this chapter).

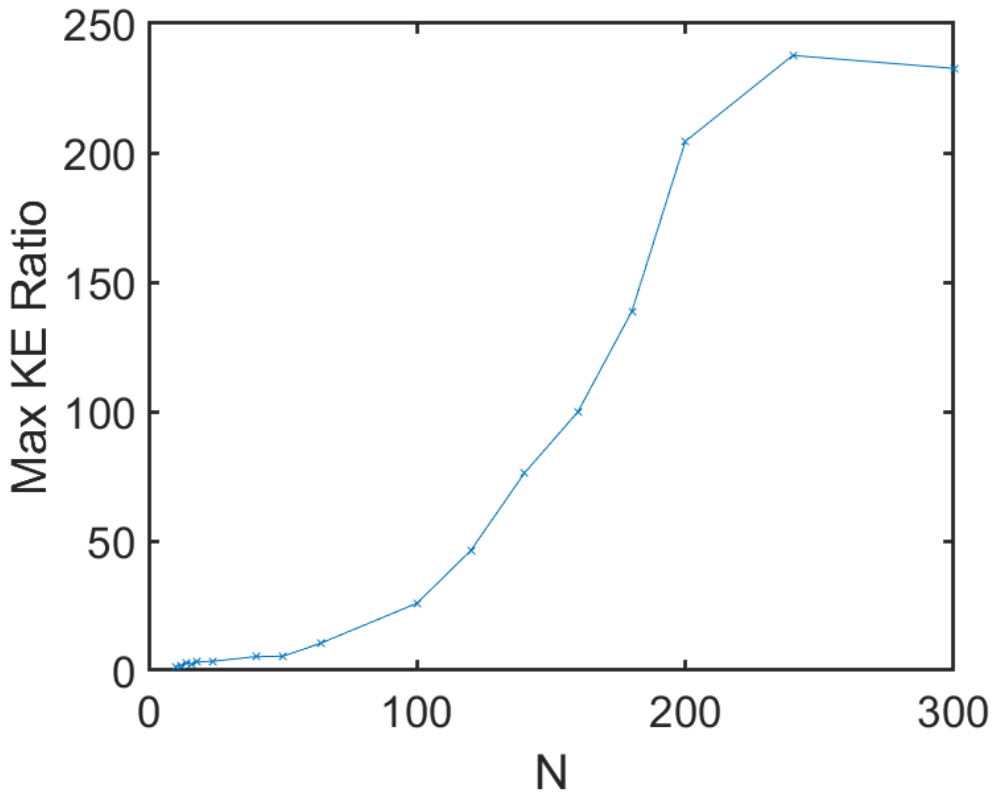

Figure 5.1: (number of DEM layers within a fixed sample size), resulting from a 0.2049 s (long) simulation duration with sample damping of 0.00164 Ns/m.

All simulations were conducted with an even N value in order to have whole integer values at the $N/2$ point, the chosen position to measure KE density. Even values of N were used so as not to have half a unit cell in the sample width. Although, particularly in low N cases, this did result in a spatial shift in the point

where data was collected. Thus it was a source of error, particularly in low N cases (for instance, with $N = 4$, choosing $N/2 = 2$ would represent the bottom quarter of the sample, rather than the halfway point). However, in larger N cases (as was the focus here), the effect was not significant. It is also noteworthy that for simplicity with this initial analysis, unit cell strain was not limited in any of these cases, which is important, because unlike the $N = 100$ cases which were shown in previous sections where performance was generally poor in instances maximum unit cell strain values were greater than one, this was not the case in the $N = 200$ simulations. Examples where unit cell strain is limited are shown in Sec. 5.1.

Motivated by the indication of a drastic performance improvement by increasing N value (between $N = 50$ and $N = 200$), these two cases and the $N = 100$ case were analyzed. Thus, Figs. 5.2, 5.3, and 5.4 show the sweeps for the $N = 50$, $N = 100$, and $N = 200$ simulations, respectively. In the $N = 50$ case, we see KE ratios greater than one generally in the entire lower region of the plot, then also in the upper middle left quadrant. We see generally poor performance in the top portion. Additionally, the maximum kinetic energy density ratio achieved is relatively low compared to the other two cases, with a maximum KE ratio of 5.43x. The $N = 100$ case, by contrast, shows the poorest performance along the top of the plot (high velocity and varied mass), and performance better than the comparison sample largely everywhere else, with exception of a small region in the bottom right corner. Importantly, however, is the large increase in maximum performance ratio from the $N = 50$ plot. In this case, the maximum KE ratio of 25.92x is almost 5x that of the $N = 50$ sweep, with only twice as many layers. Figure 5.4, the $N = 200$ sweep, shows a maximum KE ratio of 204.35x, almost 8x maximum KE ratio improvement over the maximum KE ratio in the $N = 100$ case, and almost 38x improvement over the $N = 50$ sweep, again with only 2x and 4x as many layers, respectively. Additionally, for the $N = 200$ sweep, in all of the tested conditions of the entire sweep with the exception of a single test point at $M/M_0 = 10^1$ and $V/V_0 = 10^{-0.5}$ where the performance ratio was $0.86x$, the bistable sample always outperformed the linear sample. Of note, the best performance in Fig. 5.4 occurred at impactor $V/V_0 = 10^{0.75}$, which was the fastest

impactor simulated. This suggests the possibility of even higher performance at higher impact velocity, assuming there is no constraint on maximum layer strain.

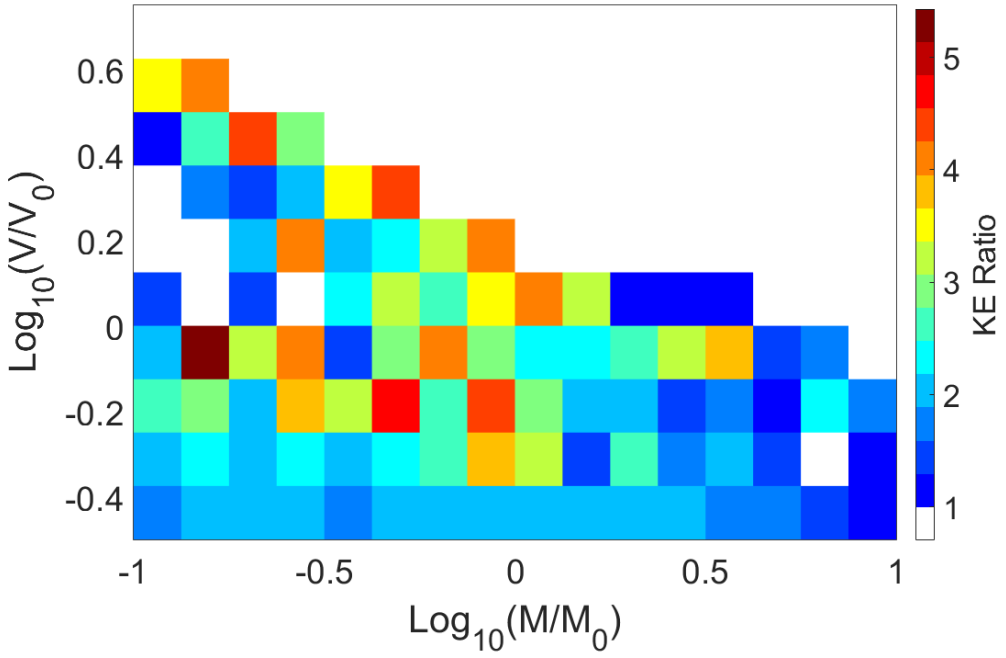

Figure 5.2: The maximum ratio of 5.43x was seen at $M/M_0 = 10^{-0.375}$ and $V/V_0 = 10^{-0.25}$.

Additional insight was gained by taking the difference of the KE ratio between a sweep of one N value and another. Figure 5.5(a) shows the maximum KE ratio of the $N = 50$ sweep subtracted from the maximum KE ratio of the $N = 200$ sweep, for each of the impactor conditions simulated. In the 187 impactor conditions simulated in this sweep, the $N = 200$ sample outperformed the $N = 50$ sample in 183 instances. Figure 5.5(b) shows the four instances where the $N = 200$ sample under performed the $N = 50$ sample. Of these four cases, the maximum KE ratio difference was $1.97x$, which occurred in a single case, and the remaining three cases had a KE ratio difference of less than 1x. Thus, not only does the $N = 200$ case possess a significantly higher maximum performance ratio, but overwhelmingly, it has superior KE ratio performance throughout the simulated sweep regime in comparison to the $N = 50$ sample.

Figure 5.6(a) shows the maximum KE ratio of the $N = 100$ sweep subtracted

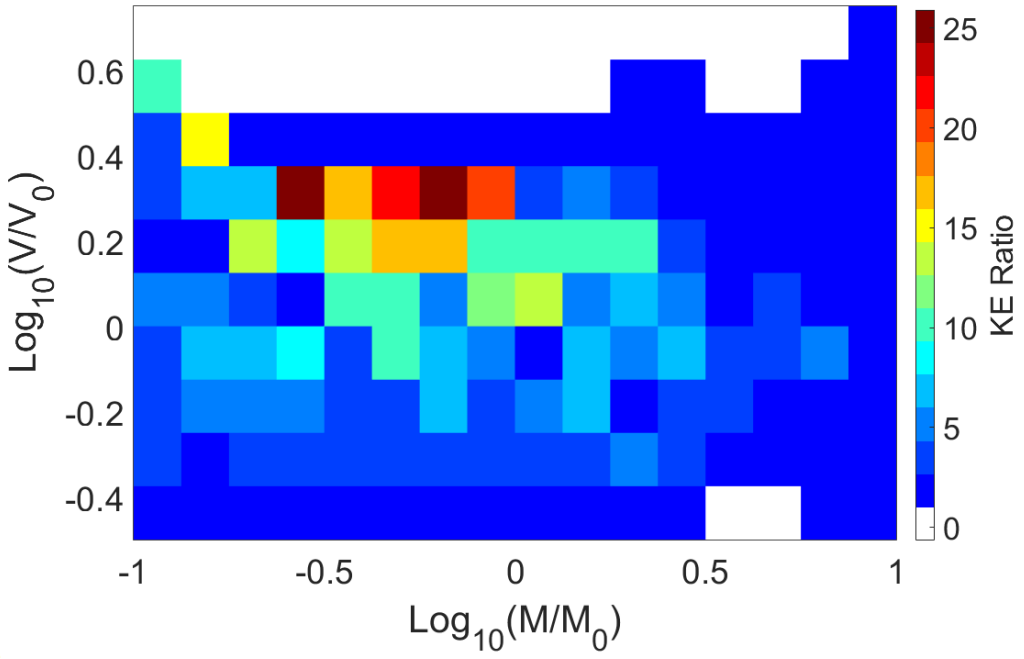

Figure 5.3: The maximum ratio of 25.92x was seen at $M/M_0 = 10^{-0.625}$ and $V/V_0 = 10^{0.25}$.

from the maximum KE ratio of the $N = 200$ sweep, for each of the impactor conditions simulated. The $N = 200$ sample had a higher maximum KE ratio in 168 of 187 cases. Figure 5.6(b) shows the 19 cases where the $N = 100$ sample's KE ratio performance was better. Of these 19 instances, a maximum ratio difference of $2 - 4$x occurred in four instances, and the ratio difference was less than $1.1x$ in the remaining instances.

Thus it appears from the data within this range and at these specific simulation conditions, that at sufficiently high N values, not only can a high level of maximum performance be achieved, but a minimum threshold of performance superior to the linear case is often achieved as well. The minimum threshold is shown particularly well in the $N = 200$ example where only a single combination of impact conditions from the entire sweep (1/187) did the bistable sample underperform the linear, and the underperformance in this single case was not by a large margin (0.86x).

Now, XT diagrams from the best performance impactor conditions of the above phase diagrams were analyzed, and the best KE ratio performance case for each

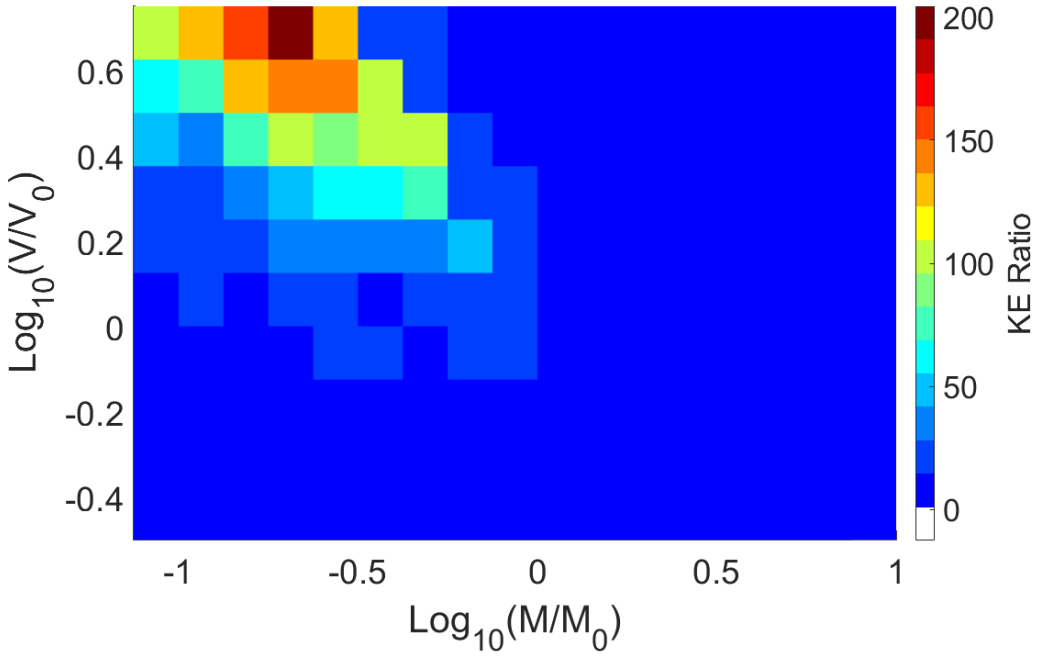

Figure 5.4: The maximum ratio of 204.35x was seen at $M/M_0 = 10^{-0.625}$ and $V/V_0 = 10^{0.75}$ Of note, the minimum value in the plot was 0.86, although the colorbar min value was adjusted lower in order to show a transition from white to blue at at KE ratio of 1.

N value was compared to the same impactor conditions from the other two N layer states. Figure 5.7 shows the KE density XT diagram for the $N = 200$ sample with impactor conditions $M/M_0 = 10^{-0.625}$ and $V/V_0 = 10^{0.75}$ (impactor conditions which yielded the highest KE density ratio for the $N = 200$ case). Figure 5.7(a) and (c) show the same KE density diagram for the bistable sample, although panel c) shows a longer simulation time than panel a) (in order to better show solitary waves in panel a), and the global simulation KE density maximum in panel c). Figure 5.7(b) and (d) show the corresponding impact into the comparison sample. In Fig. 5.7(a), immediately at impact the emission of several solitary waves are seen beginning in the bottom right corner of the plot. These solitary wave emissions have been shown in previous examples, however at the higher N value they appear to more rapidly decrease in velocity as the wave propagates in space. As the wave emission slows, it then transitions to the "oscillatory" region, which has been

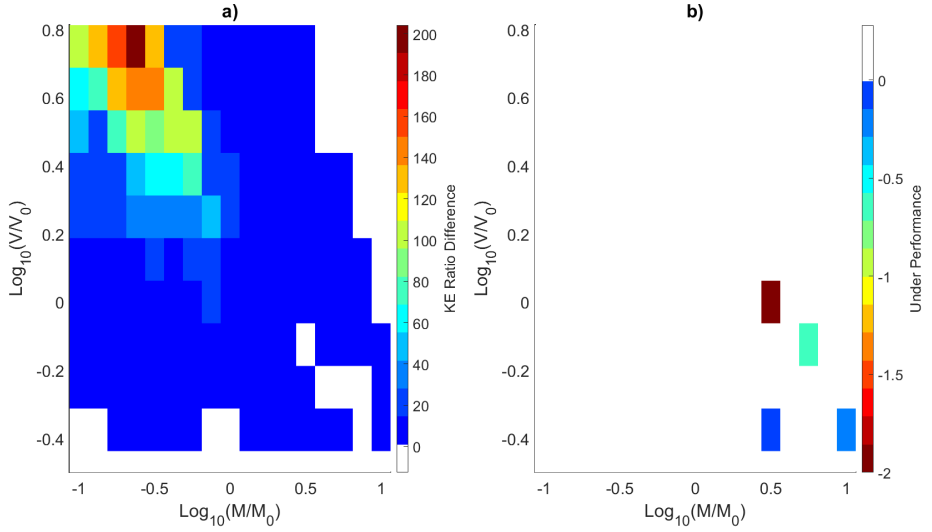

Figure 5.5: a) Difference in KE ratio between the $N = 200$ and $N = 50$ sweeps. b) Combinations of impactor mass and velocity where the $N = 200$ sample underperforms in comparison to the $N = 50$ sample.

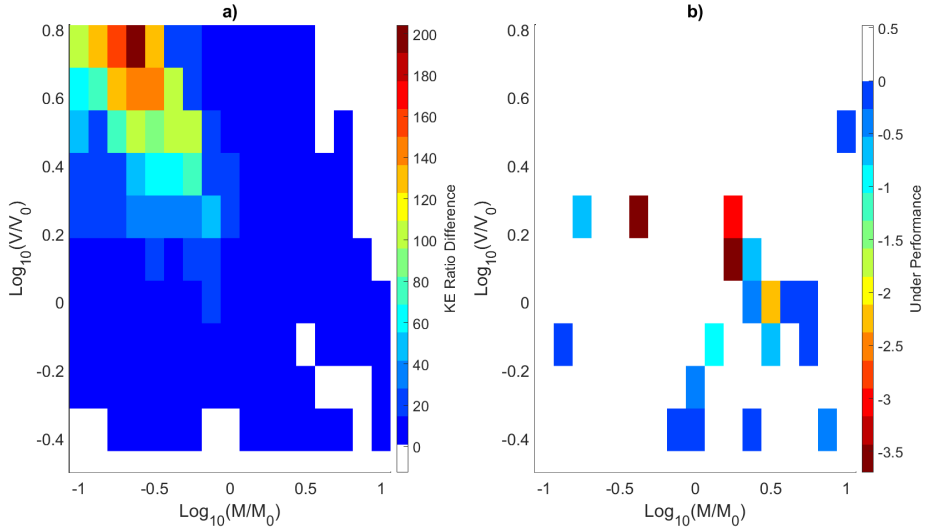

Figure 5.6: a) Difference in KE ratio between the $N = 200$ and $N = 100$ sweeps. b) Combinations of impactor mass and velocity where the $N = 200$ sample underperforms in comparison to the $N = 100$ sample.

previously described. The maximum KE density value at the half sample in Fig. 5.7(a) of 205.93 J/m^3 occurs at 5.8 ms and is circled in red. The total simulation maximum for the bistable sample is 212.68 J/m^3 occurs at $t = 0.0373$ s and is

circled in red in Fig. 5.7(c). Figure 5.7(b) and (d) show the comparative sample, where the simulation maximum KE density at the half-sample is 43.46 kJ/m^3, which occurs at $t = 5$ ms, and is circled in red in both panels. The KE ratio is 204.35x. Figure 5.8 is the spring stretch plot to accompany Fig. 5.7(a). Figure 5.7(a) shows that lots of the top layers of the lattice have snapped closed prior to the half sample point, which is an indicator of very good performance.

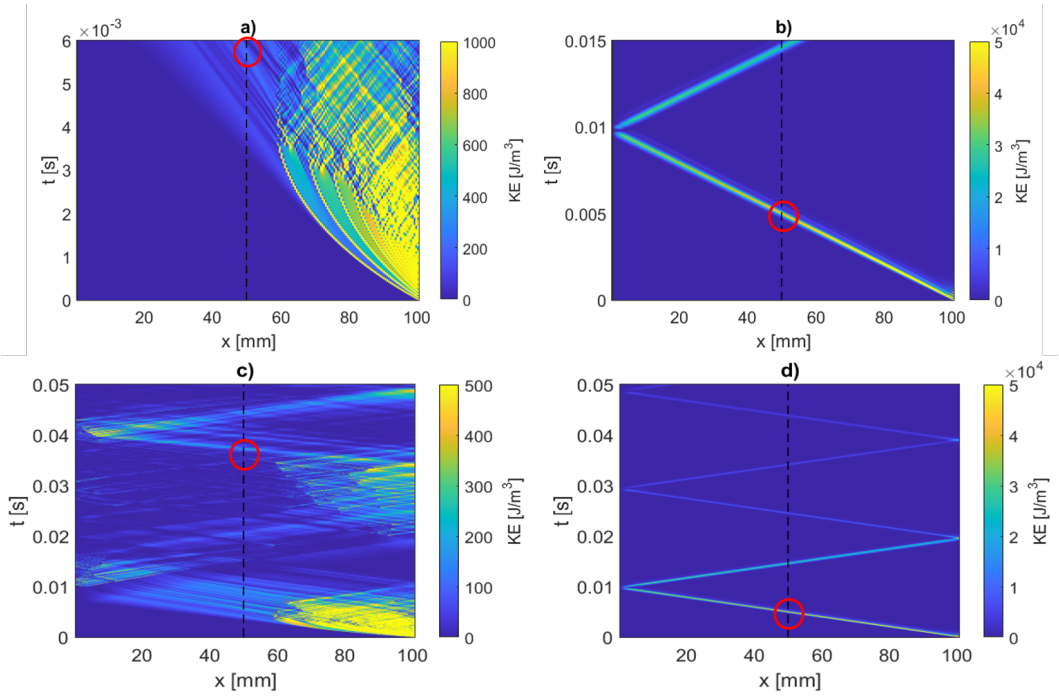

Figure 5.7: (a,c) Bistable KE density. (b,d) Linear KE density. (a,b) Short and (c,d) long time range shown. The KE ratio was 204.35x.

Figure 5.9 shows the results of the same conditions as described in Fig. 5.7, with the exception of $N = 100$. Figure 5.9(a) and (c) show the KE density and spring stretch for the bistable sample, and Fig. 5.9(b) and (d) show the same information for the linear sample. In Fig. 5.9(a), the maximum KE density of 96.89 kJ/m^3 occurs as a result of a solitary wave emission (circled in red). Figure 5.9(b) shows the maximum KE density from the linear sample of 32.59 kJ/m^3, which also occurs at the first wavefront. The KE ratio was 0.34x. In Fig. 5.9(c) we see several instances of relatively-long-time snapping shut of layers. This is indicated by the near vertical light blue lines at the end of the solitary wave

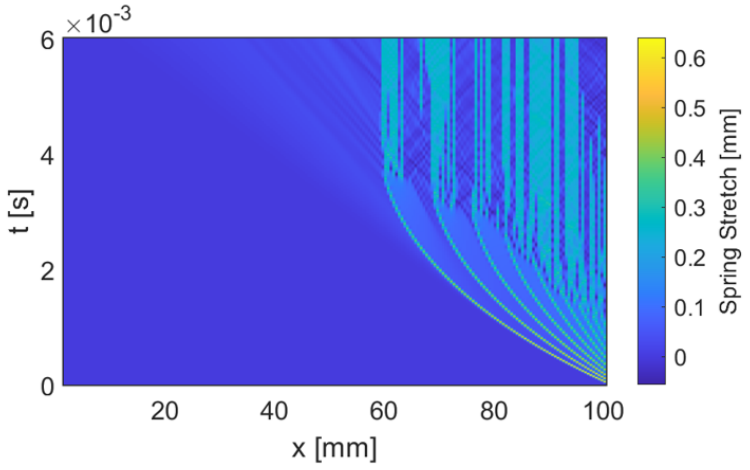

Figure 5.8: Spring stretch plot to accompany Fig. 5.7(a).

emissions at approximate spatial locations 95 mm, 78 mm, then multiple instances between 0 and 40 mm.

Qualitatively, a similar effect is seen in Figure 5.9 in comparison to Fig. 5.7, in terms of the initial emission of several solitary waves. However, unlike Fig. 5.7, the waves in this example do not decelerate as rapidly, as indicated by the more constant slope of the solitary wave emission, which results in solitary wave passage across the half sample point shortly after the sample is impacted. Additionally, while the oscillatory tail is seen at the end of many (if not all) of the solitary wave emissions, these tails are separated in space and time to a much greater extent than is seen in the $N = 200$ case. Furthermore, the $N = 200$ example in Fig. 5.8 shows far more "permanent" spring stretch than the $N = 100$ example in Fig. 5.9(c).

Figure 5.10 shows the results of all of the same conditions as described in Fig. 5.9 and 5.7, with the exception of $N = 50$. Figure 5.10(a) shows KE density for the bistable sample, and Fig. 5.10(b) shows the same information for the linear sample. The maximum KE density in Fig. 5.10(a), is 124.77 kJ/m^3, in comparison to the maximum KE density from the linear sample (Fig. 5.10(b)), of 18.96 kJ/m^3. Thus the KE ratio is $0.15x$. In comparison to the N =200 case, the difference in performance ($N = 200$ KE ratio/ $N = 50$ KE ratio) is $1,362x$.

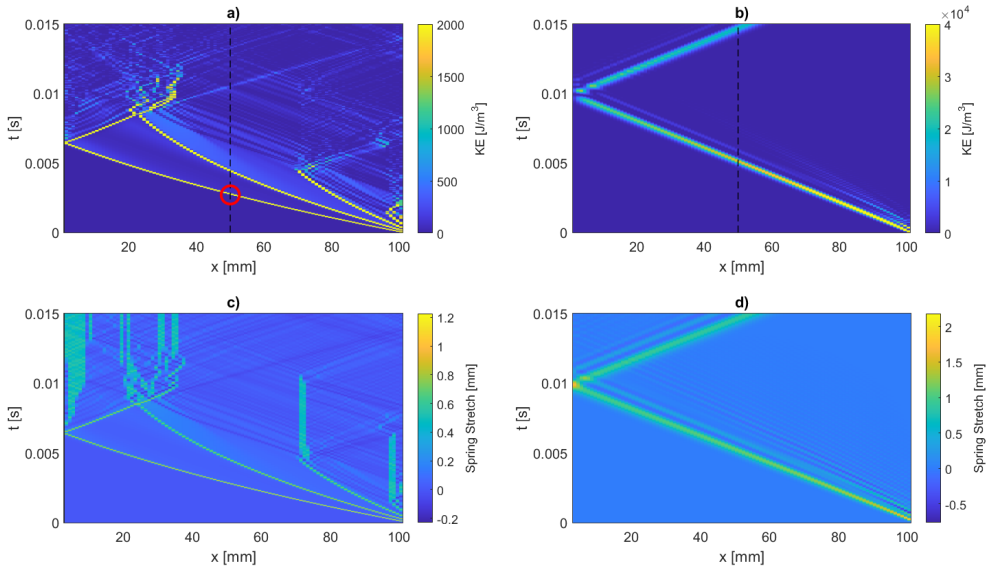

Figure 5.9: . (a,c) Bistable sample. b,d) Linear sample. The KE ratio was 0.34x.

Qualitatively, an extension of a similar comparison can be made between this case (Fig. 5.10) and the previous $N = 100$ (Fig. 5.9) and $N = 200$ (Fig. 5.7) cases. In Fig. 5.10, we see only two clear solitary wave emissions, which is less in number than either of the other two examples. While the second solitary wave is short in length, then transitions to the oscillatory region, the first solitary wave crosses the half sample point, reflects off the bottom of the sample, then reflects back with a high amount of energy density. The slope of this wave changes less than either of the two (higher N) examples. Additionally, while in the higher N examples, there are multiple other solitary waves (after the initial one) that transition to the oscillatory phase, in the $N = 50$ example, there is only one observed emission that transitions this way. It is noted that $M_R = 7.3$ for $N = 200$ at $M/M_0 = 10^{-0.625}$ in Fig. 5.7(a), $M_R = 3.7$ for $N = 100$ in Fig. 5.9(a), and $M_R = 1.8$ for $N = 50$ in Fig. 5.10. It is noted that in these three instances performance gets worse as M_R approaches 1, which is consistent with literature [8, 121].

Figure 5.11 provides additional comparison between Fig. 5.7, Fig. 5.9, and Fig. 5.10. Figure 5.11 shows the KE (in Joules) across space at 2 ms after impact for $N = 200$, $N = 100$, and $N = 50$, with a) showing the bistable samples, and

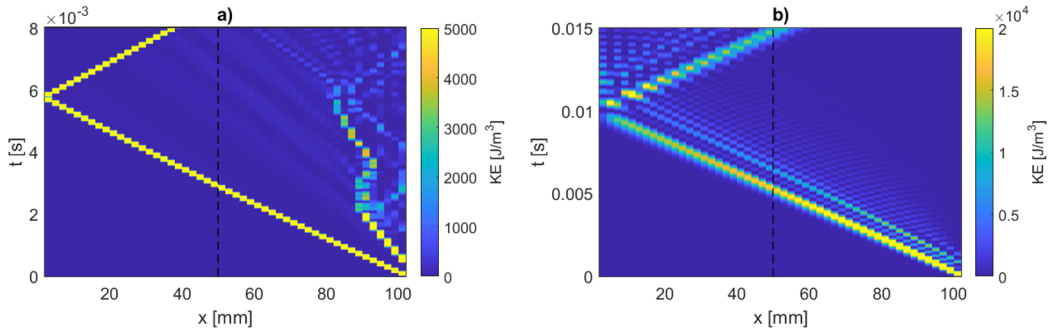

Figure 5.10: a) Bistable and b) linear sample. The KE ratio was 0.15x.

b) showing the linear. In the bistable system of Fig. 5.11(a), for the $N = 50$ case, two solitary waves are seen. The solitary wave with the largest magnitude starts at approximately 62 mm, which is approximately twice the magnitude of the corresponding linear wave at $N = 50$ shown in Fig. 5.11(b) (starting at approximately 76 mm). The pulse width of the highest amplitude $N = 50$ solitary wave is approximately 6 mm ($\approx$ 3 particles), in comparison to the highest amplitude $N = 50$ linear wave, which has a pulse width of approximately 10 mm ($\approx$ 5 particles). The largest amplitude $N = 50$ nonlinear wave in Fig. 5.11(a) subsequently crosses the half sample point, and results in poor overall performance. Also in Fig. 5.11(a), for $N = 100$, three distinct solitary waves peaks are seen, with the largest magnitude on the order of, but less than the magnitude of the largest magnitude $N = 100$ linear wave in Fig. 5.11(b). This large magnitude solitary wave also crosses the half sample point and results in poor performance. The pulse width of the highest amplitude $N = 100$ solitary wave is approximately 3 mm ($\approx$ 3 particles), in comparison to the highest amplitude $N = 100$ linear wave, which has a pulse width of approximately 7 mm ($\approx$ 7 particles). In the $N = 200$ case in Fig. 5.11(a), more than 4 peaks are seen, with the largest amplitude less than half of the amplitude of the largest $N = 200$ linear wave in Fig. 5.11(b). These higher in number, but smaller in magnitude solitary waves do not cross the half sample point (as seen in Fig. 5.7(a)), resulting in excellent performance. The pulse width of the highest amplitude $N = 200$ solitary wave is approximately 1 mm ($\approx$ 2 particles), in comparison to the highest amplitude $N = 200$ linear wave, which has a pulse

width of approximately 4.5 mm (≈ 9 particles). The phenomenon of smaller layer sizing resulting in more, but smaller magnitude boluses of energy being carried in solitary waves is consistent with prior studies [8]. Additionally, the pulse width of the bistable samples discussed remains similar (in terms of particle number), while the pulse width of the linear samples increases with increasing N value. This difference, indicative of the pulse width being tied to a number of particles as opposed to a spatial distance for solitary waves in the bistable samples, again is consistent with literature [8].

Separately, in Fig. 5.11(b), the linear comparison, note that the leading pulse has approximately the same wavespeed for different N (same impactor conditions). In contrast, the pulses have different KE magnitudes as a result of more/fewer particles per volume (resulting in similar KE density), as well as dispersive effects. This highlights the necessity of comparing bistable and linear performance directly only when both samples are of the same N value, and is discussed further later in this section.

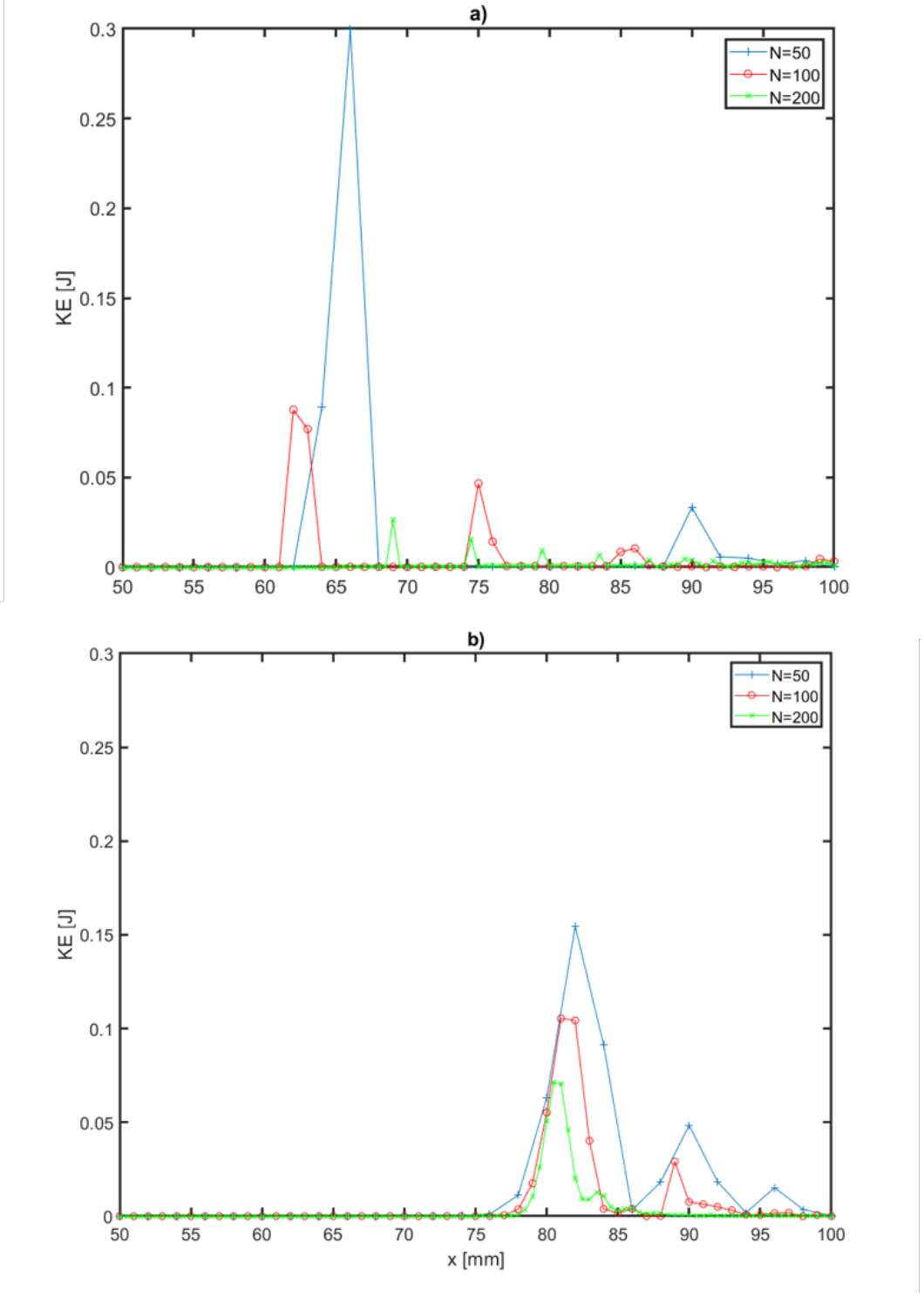

Figure 5.11: Kinetic energy at 2 ms for $N = 200$, $N = 100$, and $N = 50$ samples shown in Figs. 5.7, 5.9, and 5.10. a) Bistable cases. b) Linear cases.

Now a comparison was performed between the $N = 100$ case at the impactor conditions corresponding to the best $N = 100$ performance, with the $N = 200$, and $N = 50$ samples stuck at the same impactor conditions. Figure 5.12 shows the KE density plot for the best performing case of the $N = 100$ sample, at impactor conditions: $M/M_0 = 10^{-0.625}$ and $V/V_0 = 10^{0.25}$. The maximum KE ratio was $25.9x$. Three key observations about Fig. 5.12(a) are noted: first, multiple solitary wave emissions are seen that transition to the oscillatory regime prior to the halfway point of the sample. Second, we see a slowing of the wavespeed in the solitary wave emission, as indicated by an increase in the slope (moving right to left). Finally, if we reference Fig. 3.16(c), we note extended time periods of snapping of layers prior to the half-sample point (indicated by the light blue vertical lines in the XT diagram spring stretch plot). These three observations appear to positively influence KE ratio.

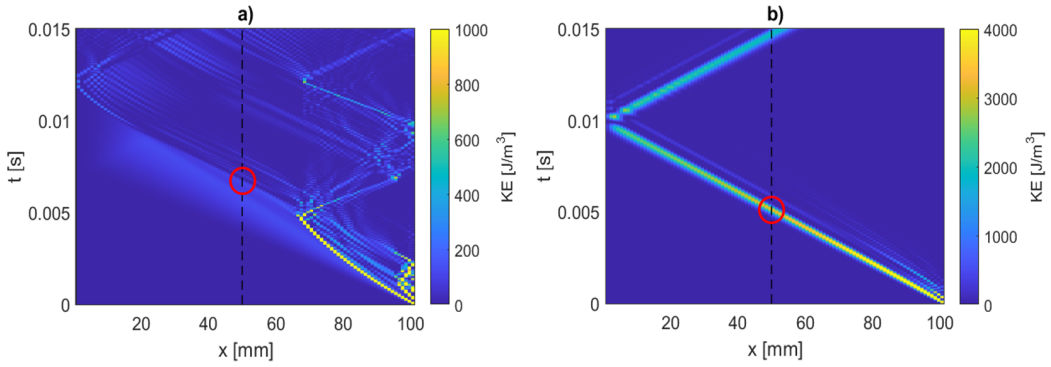

Figure 5.12: The resulting maximum KE density performance ratio was $25.9x$. a) Bistable sample. b) Linear sample.

Figure 5.13 shows the results at the same simulation and impactor conditions as Fig. 5.12, with the exception of using a $N = 50$ sample. The maximum KE ratio was 1.93x. Similar to Fig. 5.12(a), in Fig. 5.13(b), at the initial impact a solitary wave is seen that transitions to the oscillatory regime. However, in contrast to the $N = 100$ example, the $N = 50$ example emits two solitary waves from the oscillatory regime after impact. The first wave is emitted at approximate time 4 ms, and crosses the half sample point at time 6.1 ms at a KE density value of 991.61 J/m^3, causing the 1.93x KE ratio value. A secondary solitary wave (of lesser KE

density when crossing the half-sample point) is also emitted at approximately 6.5 ms, although this does not affect the KE ratio. Additionally, it is noted that the slope of both solitary wave emissions in Fig. 5.13(a) appear to be mostly linear, while the emission from the $N = 100$ example in Fig. 5.12(a) shows a decreasing slope.

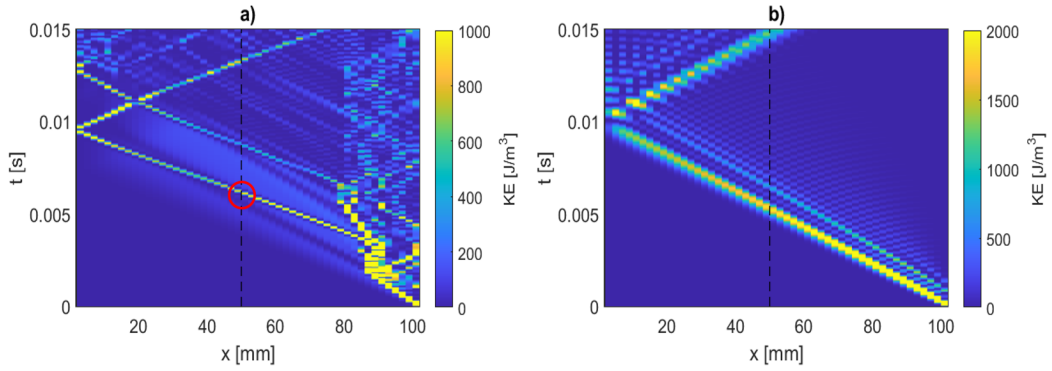

Figure 5.13: The resulting maximum KE ratio is 1.93x. The maximum KE ratio in the bistable case was 991.61 J/m^3 and the maximum KE density transmission in the linear case was 1909.97 J/m^3. a) Bistable and b) linear sample.

Figure 5.14 shows the results at the same simulation and impactor conditions as Fig. 5.13 and Fig. 5.12, with exception of now using a $N = 200$ sample. Figure 5.14(a) shows the bistable sample and Fig. 5.14(b) shows the linear sample. The maximum KE density across the half sample point was 128.08 J/m^3 in panel a), and 4359.09 J/m^3 in panel b). The KE ratio was 34.03x. Similar to the $N = 100$ example in Fig. 5.12(a), in Fig. 5.14(a), multiple solitary wave emissions are seen beginning at the initial impact. However, the longest of these wave emissions propagates a shorter temporal distance (approximately 2 ms vs approximately 5 ms in the $N = 100$ example) prior to transitioning to the oscillatory regime. Additionally, by inspection, there's a larger increase in the slope of the solitary wave emission in the $N = 200$ example, indicative of more slowing of the wave emission. Thus, even at the impact conditions of best performance for the $N = 100$ example, the $N = 200$ example has a higher KE ratio.

As an aside, a reader might note that while the KE ratio of the $N = 200$ example is superior to the $N = 100$ example, by comparison of only the kinetic

energy density transmission of the bistable samples (panel a)) of each of these two examples, there's actually more transmission in the $N = 200$ example (128.08 vs. 126.35 J/m^3). However, this is an example of the smaller layer volume which occurs in the higher N cases being able to more precisely capture (or saturate) at the passage of a pulse, in comparison to a lower N example (larger layer volume) having an averaging effect. For instance, in this example, as noted the $N = 200$ example transmits 128.08 J/m^3, recorded at the 100th layer at $t = 6.8$ms, while the $N = 100$ example transmits 126.35 J/m^3, recorded at the 50th layer at $t = 5.7$ ms. To more accurately compare the KE density quantities directly, we look to the 101st layer in the $N = 200$ example, where we record 123.29 J/m^3 at the same time where we recorded for the 100th layer ($t = 6.8$ms). Averaging the recordings of layer 100 and 101 yields 125.69 J/m^3, less than the maximum KE density transmission recorded in the $N = 100$ example. This example also illustrates the rationale for calculating KE ratio (bistable/linear) only between samples of the same N value, then comparing KE ratio to KE ratio between samples of different N values. This method avoids possible "averaging mismatches", as explained above, and also disparities in comparison resulting from dispersive effects of lattice spacing a decreasing at higher N values.

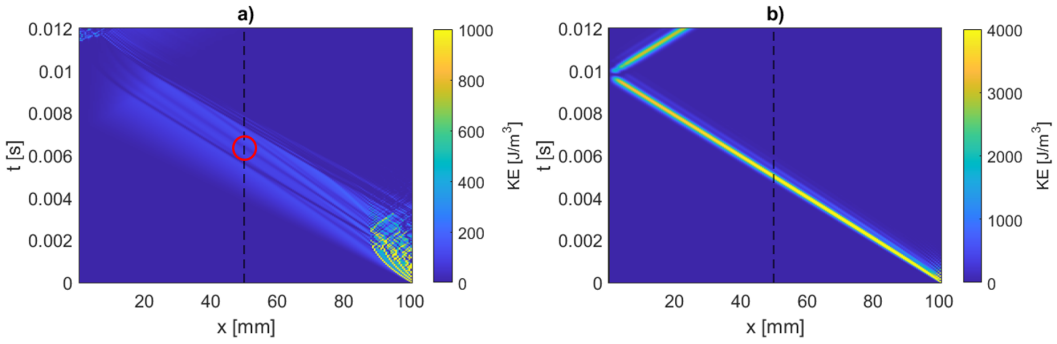

Figure 5.14: The resulting maximum KE density performance ratio is 34.03x. a) Bistable sample. b) Linear sample.

Finally, a comparison was performed between the $N = 50$ case at the impactor conditions which it performed the best, with the $N = 200$, and $N = 100$ samples stuck at the same impactor conditions for comparison. Figure 5.15 shows the results of the best performing case of the $N = 50$ sweep, at impactor conditions

$M/M_0 = 10^{-0.375}$ and $V/V_0 = 10^{-0.25}$, with a KE ratio of 4.78x. Fig. 5.15(a) shows the bistable sample, where a maximum KE density at the half sample of 83.25 J/m^3 was transmitted. Figure 5.15(b) shows the linear sample, where a maximum KE density at the half sample of 398.28 J/m^3 was transmitted. The author doesn't have much qualitative commentary on this example, although it appears the pulse is concentrated at the initial impact, then it dissipates and broadens prior to reaching the half-sample point.

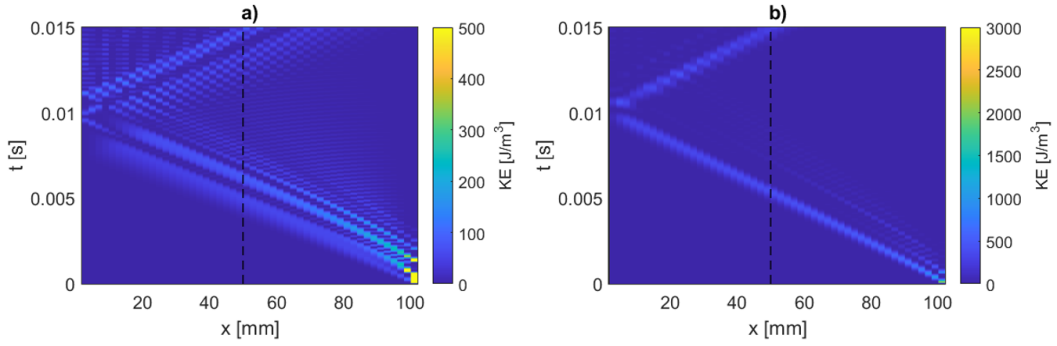

Figure 5.15: The KE ratio is 4.78x. a) Bistable sample. b) Linear sample.

Fig. 5.16 shows the results at the same simulation and impactor conditions as Fig. 5.15, with the exception of now using a $N = 100$ sample. In Fig. 5.16(a), the bistable sample, the maximum KE density value of 164.97 J/m^3 occurs at $t = 0.023$ s, while the maximum value at the first wavefront was 84.15 J/m^3 at 5.7 ms. In Fig. 5.16(b), the linear sample has a KE density maximum at the half sample of 572.49 J/m^3 that occurs at approximately 6 ms. Thus the KE ratio for the whole simulation time is 3.47x, or 6.8x in the case of short simulation duration. This is an example where the lower N sample, Fig. 5.15, performs better, but only in the long duration simulation.

Fig. 5.17 shows the results at the same simulation and impactor conditions as Fig. 5.15 and Fig. 5.16 with the exception of now using a $N = 200$ sample. Fig. 5.17(a) shows the bistable sample, where the maximum KE density transmission at the half sample was 87.74 J/m^3 at $t = 5.4$ ms. Figure 5.17(b) shows the linear sample, where the maximum KE density transmission at the half sample was 665.27 J/m^3. The KE ratio was 7.58x.

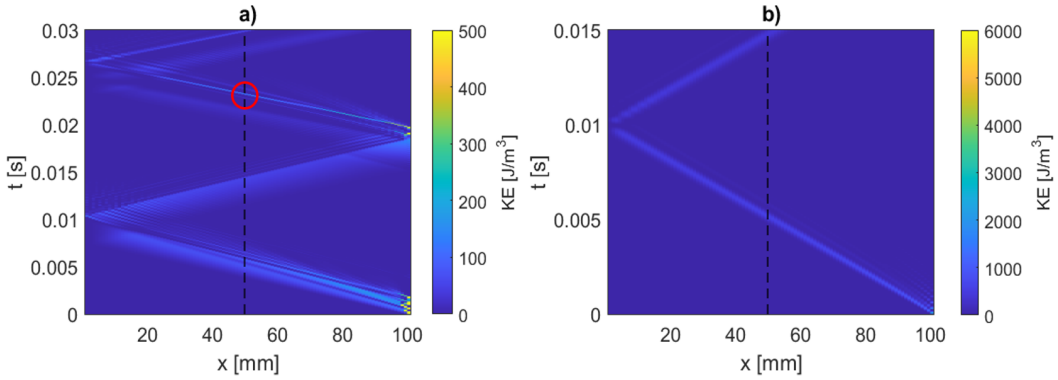

Figure 5.16: The resulting maximum KE density performance ratio is 3.47x. a) Bistable sample. b) Linear sample.

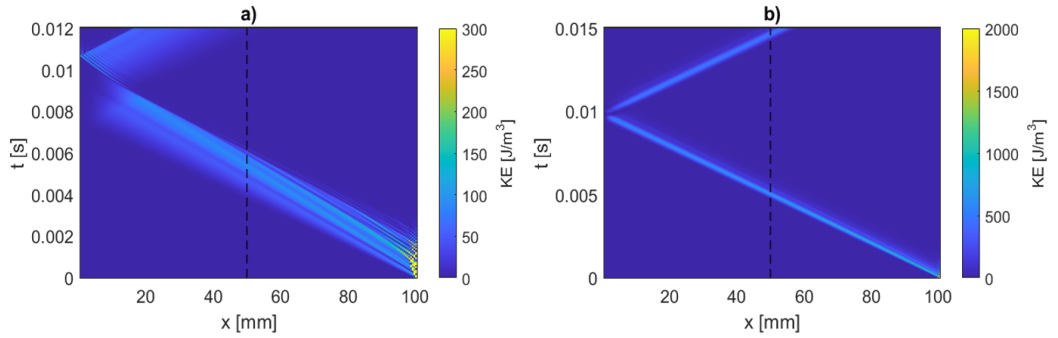

Figure 5.17: The resulting maximum KE density performance ratio is 7.58x. a) Bistable sample. b) Linear sample.

The following broad observations can be made based on a comparison on the nine examples above. First, if we consider only the simulation time up to the first wavefront hitting the floor of the sample, then in all of the shown XT diagrams for the same impactor conditions, the higher N case always results in higher KE ratio. For instance, at the impactor conditions of best performance for the $N = 50$ sample, the $N = 100$ and $N = 200$ lattice still performed better, even-though the best performance for $N = 100$ and $N = 200$ occurred at different impact conditions. If we consider simulation time beyond the initial wavefront, this observation still holds true with the one exception of impact conditions $M/M_0 = 10^{-0.375}$ and $V/V_0 = 10^{-0.25}$, where the $N = 50$ lattice with a 4.78x ratio outperforms the $N = 100$ case's 3.47x ratio.

Combining the results of the N vs Max KE ratio sweeps, the KE ratio difference plots, as well as the XT diagrams comparing for the best KE ratio impact conditions of the three sampled lattices, a strong correlation between: higher N number and higher maximum performance, and higher N number and better minimum performance is indicated.

5.1 Strain limited updates to simulations investigating the effect of increased layers on maximum KE ratio performance

This section highlights differences from the previous section that occur when results are limited only to the simulations where the maximum layer strain is less than one. Figure 5.18 shows the results from sweeps of the same conditions described for the Fig. 5.1 sweeps in the proceeding section, with the following two exceptions. First, only maximum KE ratio values were plotted for cases where the maximum layer strain in the simulation was less than one. Second, the simulation duration was 0.03 s ($T_s \approx 3$). This allowed for shorter simulation runs and was assessed to be adequate since the majority of the maximum values in the damped simulation at the same conditions occurred during the first 1 ms.

The data in Fig. 5.18 still shows a significant increase in maximum KE ratio performance with more layers, at least within the range of 50 to 150 layers. However, the maximum KE ratio values are much lower in the maximum strain limited sweeps. The maximum KE ratio value also appears to either saturate or decrease after approximately 150 layers, although further analysis of this observation was left for future work.

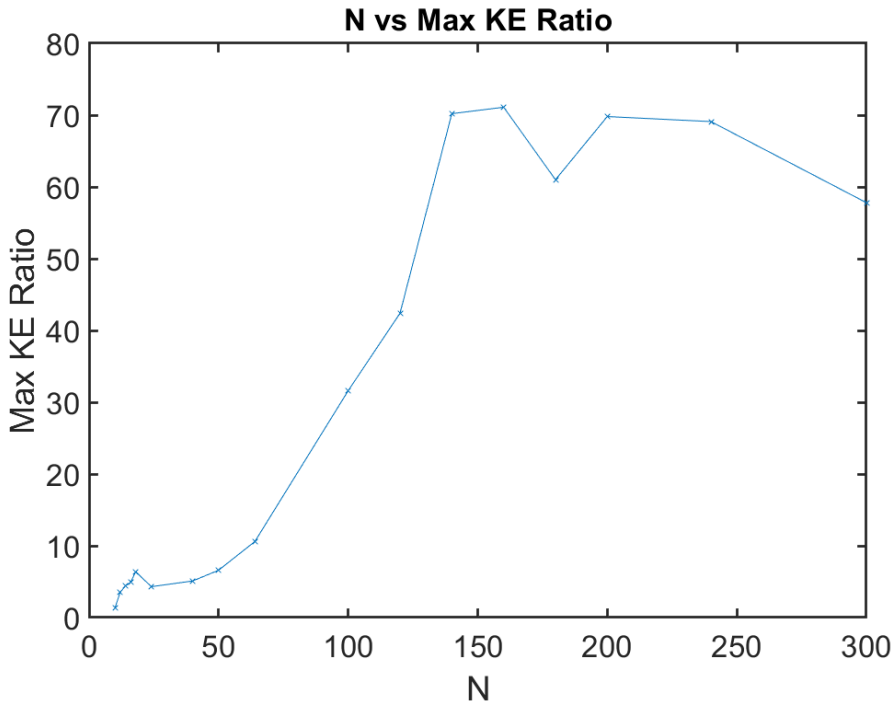

Figure 5.18: Each discreet point represents the maximum KE ratio achieved from a sweep of plus and minus one order of magnitude from nominal impactor mass and plus and minus one-half order of magnitude from nominal impactor velocity for the given N value, with the maximum unit cell strain limited to one for all cases. The sample damping value was 0.00164 Ns/m.

Figure 5.19(a) shows the maximum KE ratio performance for the $N = 200$, 0.00164 Ns/m sample damping, 0.015 s simulation duration sweep. Figure 5.19(b) displays the impact conditions where maximum layer strain values equal to or greater than one occur. The best performance that occurs below the strain threshold is 69.8x at $M/M_0 = 10^{-0.25}$ and $V/V_0 = 10^{0.375}$.

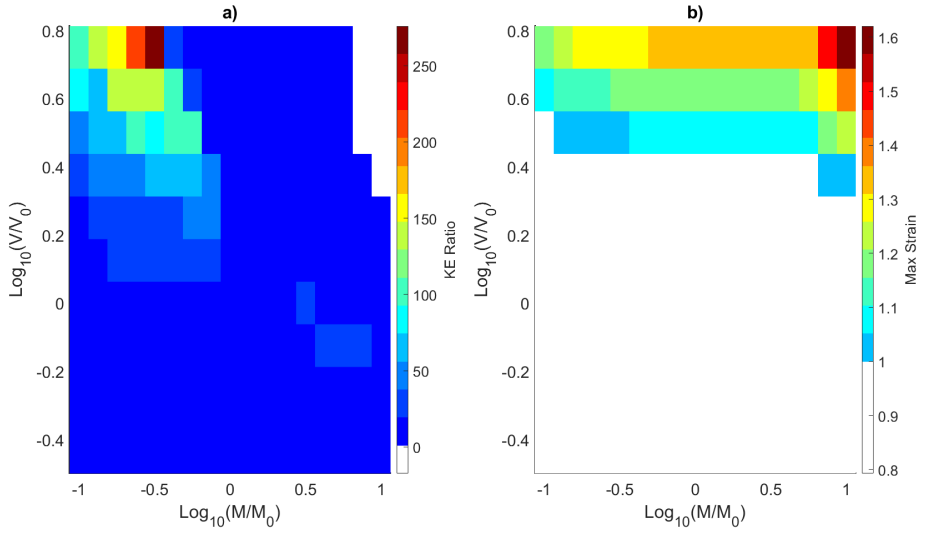

Figure 5.19: a) Maximum KE ratio for a given combination of impactor mass and velocity. b) Maximum layer strain that occurred for a given combination of impactor conditions. The minimum value in a) was 0.82 although the plot colorbar scale was reduced in order to show the transition between white and blue at a value of 1.

Figure 5.20 shows the maximum KE ratio performance for the $N = 100$, 0.00164 Ns/m sample damping, 0.03 s simulation duration sweep, as well as the maximum layer strain experienced during that sweep. The maximum KE ratio in this sweep was 31.6x at impactor conditions $M/M_0 = 10^{-0.125}$ and $V/V_0 = 10^{0.25}$, resulting in a maximum layer strain value of 0.94. Of note, in Fig. 5.20, maximum layer strain values greater than one occurred at impactor conditions which resulted in poor KE ratio performance, thus the strain limit did not affect the maximum KE ratio value in this sweep.

Figure 5.21 shows the maximum KE ratio performance for the $N = 50$, 0.00164 Ns/m sample damping, 0.06 s simulation duration sweep, as well as the maximum layer strain experienced during that sweep. The maximum KE ratio in this sweep

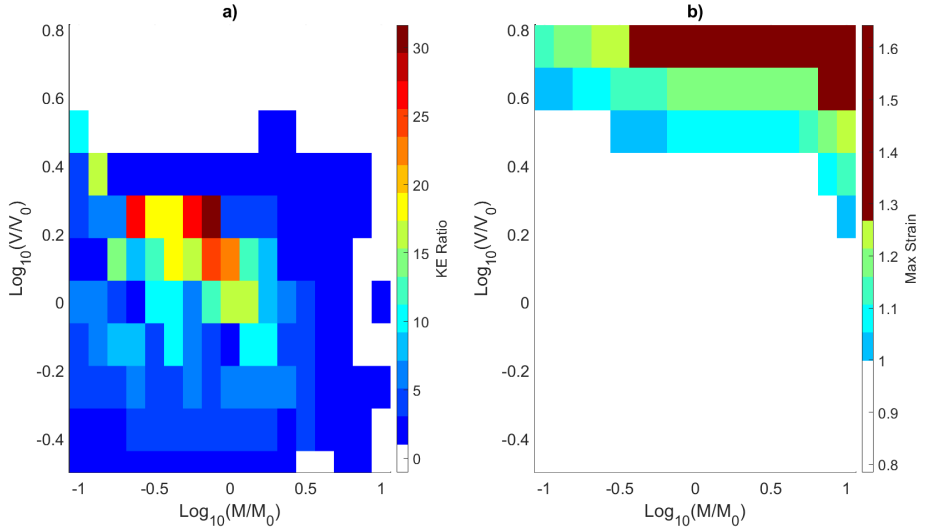

Figure 5.20: a) Maximum KE ratio for a given combination of impactor mass and velocity. b) Maximum layer strain that occurred for a given combination of impactor conditions.

was $6.41x$ at impactor conditions $M/M_0 = 10^{-0.625}$ and $V/V_0 = 10^{0.375}$, which occurred at a maximum strain value of 0.85. Similar to the $N = 100$ sweep in Fig. 5.20, maximum layer strain values greater than one occurred at impactor conditions which resulted in poor KE ratio performance, thus the strain limit did not affect the maximum KE ratio value in this sweep either.

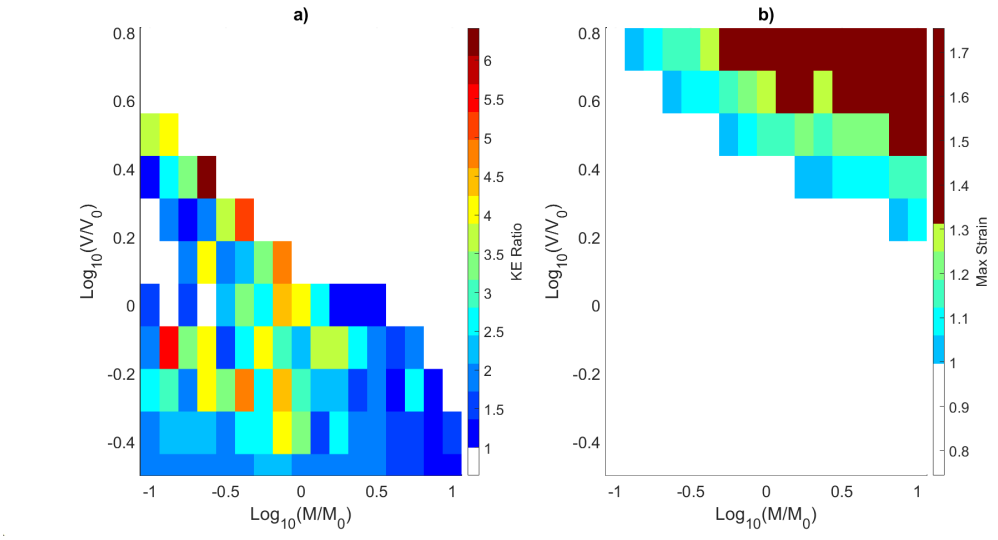

Figure 5.21: a) Maximum KE ratio for a given combination of impactor mass and velocity. b) Maximum layer strain that occurred for a given combination of impactor conditions.

The $N = 200$ sweep was the only example from the three sweeps above where the maximum KE ratio value decreased significantly with the imposition of the strain limit. For this reason, the impact conditions corresponding to the best KE ratio performance in the $N = 200$ (where layer strain is less than one) example are compared with the same impact conditions for the $N = 100$ and $N = 50$ samples. Thus XT diagrams at impactor conditions $M/M_0 = 10^{-0.25}$ and $V/V_0 = 10^{0.375}$ for $N = 200$, $N = 100$, and $N = 50$ samples were analyzed.

Figure 5.22 shows the results of the best performing case of the $N = 200$ sweep, at impactor conditions $M/M_0 = 10^{-0.25}$ and $V/V_0 = 10^{0.375}$, with a KE ratio of 69.8x. Figure 5.22(a) and (c) shows the KE density and spring stretch of the bistable sample, and Fig. 5.22(b) and (d) shows the same information for the linear sample. In Fig. 5.22(a) the maximum KE density crossing the half-sample point is 196.6 J/m^3, and in Fig. 5.22(c) significant "permanent" (for the duration of the simulation) spring stretch is seen for approximately the top 20 percent of the sample. Figure 5.22(b) reveals 13.73 kJ/m^3 of KE density crossing the half sample.

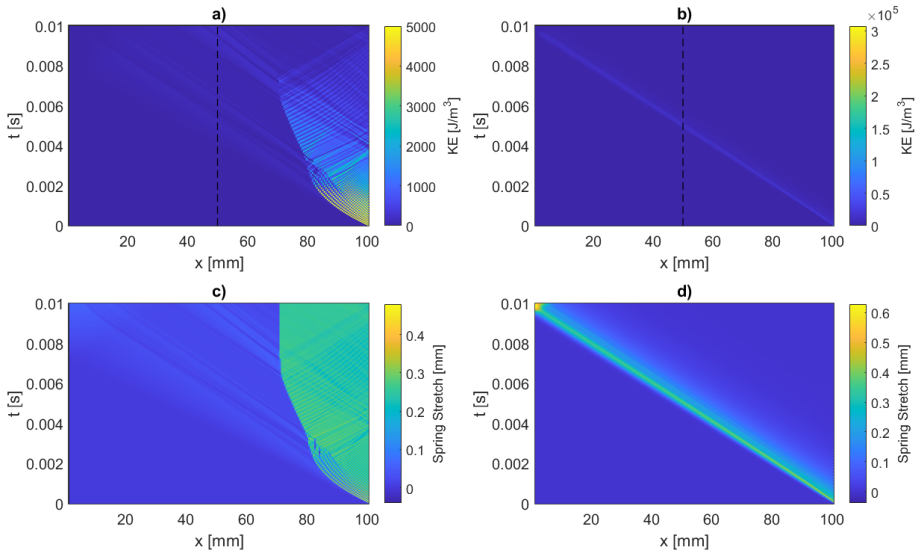

Figure 5.22: KE density plots for impactor conditions $M/M_0 = 10^{-0.25}$ and $V/V_0 = 10^{0.375}$, simulation duration 0.015s, using η_s in the amount of 0.00164 Ns/m for an $N = 200$ sample. a,c) Bistable sample. b,d) Linear sample. The KE ratio was 69.8x.

Figure 5.23 shows the results at the same simulation and impactor conditions as Fig. 5.22 with the exception of now using a $N = 100$ sample and the simulation duration changing to 0.03s. Figure 5.23(a) and (c) shows the KE density and spring stretch of the bistable sample, and Fig. 5.23(b) and (d) shows the same information for the linear sample. In Fig. 5.23(a), the maximum KE density crossing the half sample point was 9475.38 J/m^3, and solitary wave propagation is seen which crosses the half sample point, which is the reason for high value.

In Fig. 5.23(b) the maximum KE density crossing the half sample point was 12501 J/m^3. The KE ratio was 1.32x.

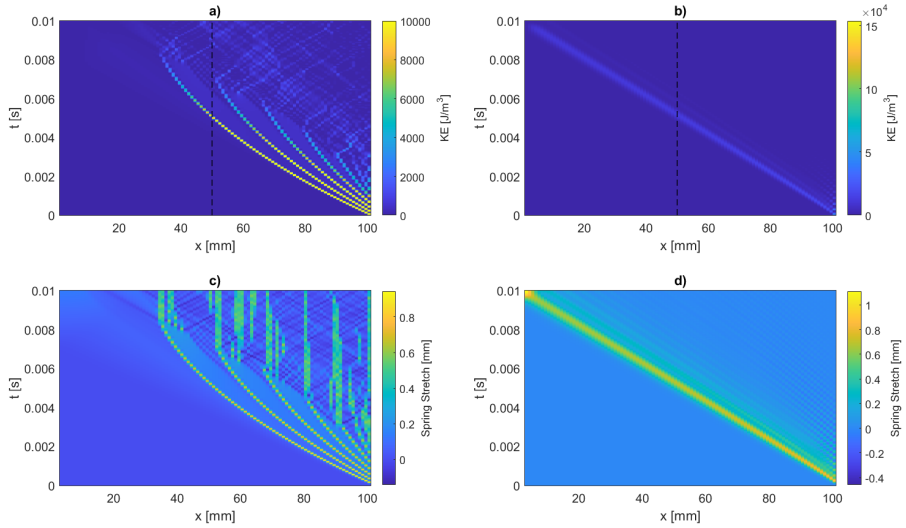

Figure 5.23: KE density plots for impactor conditions $M/M_0 = 10^{-0.25}$ and $V/V_0 = 10^{0.375}$, simulation duration 0.03s, using η_s in the amount of 0.00164 Ns/m for an $N = 100$ sample. (a,c) Bistable sample. (b,d) Linear sample. The KE ratio was 1.32x.

Figure 5.24 shows the results at the same simulation and impactor conditions as Fig. 5.22 and Fig. 5.23 with the exception of now using a $N = 50$ sample and the simulation duration changing to 0.06s. Figure 5.24(a) and (c) shows the KE density and spring stretch of the bistable sample, and Fig. 5.24(b) and (d) shows the same information for the linear sample. In Fig. 5.24(a), the maximum KE density crossing the half sample point was 30.89 kJ/m^3, and in Fig. 5.24(b) the maximum KE density was 9.36 kJ/m^3 in the linear sample. In Fig. 5.24(a) solitary

wave propagation is seen which crosses the half sample point, which is the reason for the low performance ratio.

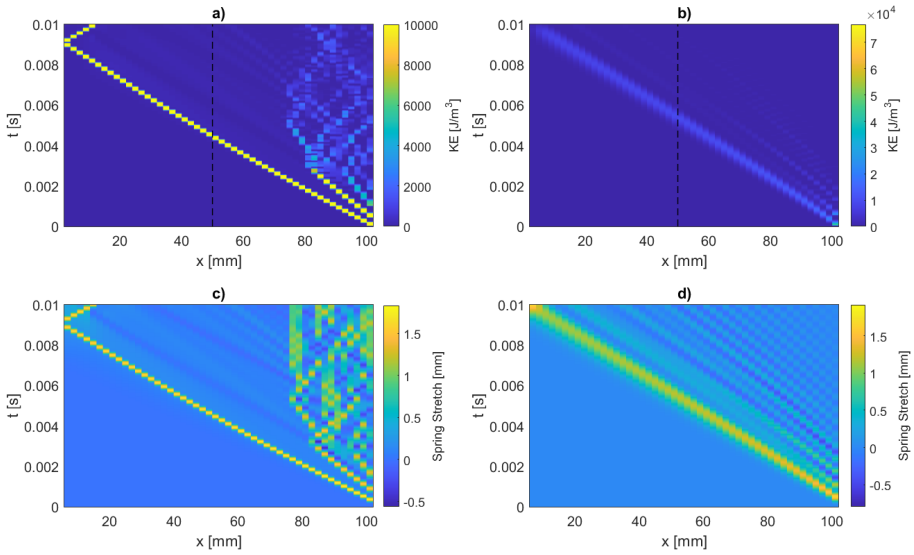

Figure 5.24: KE density plots for impactor conditions $M/M_0 = 10^{-0.25}$ and $V/V_0 = 10^{0.375}$, simulation duration 0.06s, using η_s in the amount of 0.00164 Ns/m for an $N = 50$ sample. (a,c) Bistable sample. (b,d) Linear sample. The KE ratio was 0.30x.

When the model is constrained to maximum bistable sample unit cell strain values less than one, the maximum attainable energy in impact conditions is less, and the maximum attainable KE density performance ratios are also less. Despite this, the KE density ratio performance still increases substantially with more unit cells (layers) in a given sample size, and the qualitative mechanisms appear similar. Of note, the maximum layer strain limit, significantly decreases the maximum KE ratio of the $N = 200$ example, although it does not limit the $N = 100$ and $N = 50$ examples. This warrants further investigation.

Chapter 6

Damping analysis

Although it was understood that damping would play a critical role in system performance, the most effective way to model the damping, or methods in which material damping would interact with bistable effects remained to be determined. First, a simple analytical method using onsite damping was completed. Next, intersite damping was analyzed, in order to more realistically model the physics of the system. Then, DEM simulations were run in order to verify the ability to input a damping value into the system ODEs, then recover a similar value by analyzing the decay rate of the particle velocity. Finally, dynamic mechanical analysis (DMA) was completed with Tango Black Plus, the rubber simulant used for the beam material 3D printed experimental samples, in order to analyze its bulk damping properties, as well as the properties for the unit cell.

6.1 Analytics for onsite damping

Figure 6.1 shows the model for onsite damping, based on the model for a string on a viscous base from Ref. [123]. This model consists of a system of uniform linear springs k, masses m, linear dampers η, spacing a, displacement u_i, with i representing the mass number in the chain. The dampers connect each mass to a fixed base.

Figure 6.1, discreet in space but continuous in time, is described by the ODE:

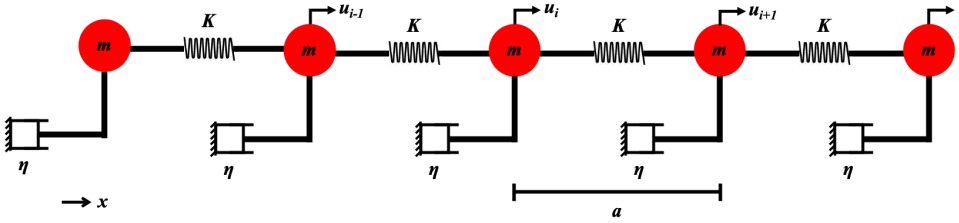

Figure 6.1: Onsite damping mass and spring model.

$$m\ddot{u}_i = k(u_{i+1} - 2u_i + u_{i-1}) - \eta\dot{u}_i. \tag{6.1}$$

The second order finite difference formula was used to convert Eq. 6.1 to the partial differential equation (PDE) described by:

$$m\frac{\partial^2 u}{\partial t^2} = ka^2\frac{\partial^2 u}{\partial x^2} - \eta\frac{\partial u}{\partial t}. \tag{6.2}$$

Equation 6.2 was solved by assuming the wave solution:

$$y = Ae^{i(\gamma x - \omega t)}, \tag{6.3}$$

where γ is the wavenumber and ω the angular frequency. Substituting Eq. 6.3 into Eq. 6.2 yields the dispersion relation:

$$\gamma^2 = \frac{\eta i\omega}{a^2 k} + \frac{\omega^2}{{c_0}^2}, \tag{6.4}$$

with roots:

$$\gamma = \sqrt{Q}e^{i\left(\frac{\phi}{2} + n\pi\right)}, \tag{6.5}$$

where $n = \{0, 1\}$, phase

$$\phi = \arctan\left[\frac{\eta}{m\omega}\right], \tag{6.6}$$

and magnitude

$$Q = \frac{1}{ka}\sqrt{\left(\frac{\eta}{a}\right)^2\omega^2 + \left(\frac{m}{a}\right)^2\omega^4}. \tag{6.7}$$

Expanding roots γ we obtain:

$$\gamma = \pm \left(\sqrt{Q} \cos\left(\frac{\phi}{2}\right) + i\sqrt{Q} \sin\left(\frac{\phi}{2}\right) \right), \tag{6.8}$$

corresponding to right (+) and leftward (−) propagating waves, respectively. Defining γ_r and α as the real and imaginary parts of Eq. 6.8, respectively, and substituting into Eq. 6.3 yields:

$$y = Ae^{-\alpha x} e^{i(\gamma_r x - \omega t)} \tag{6.9}$$

for the rightward propagating solution. To find the relationship between the decay rate α and damping coefficient η, we substitute Eq. 6.6 and Eq. 6.7 into α, which results in (using trigonometric identities):

$$\alpha = \sqrt{\frac{\sqrt{\frac{\omega^2(\eta^2+m^2\omega^2)}{a^2}}}{2ak} \left(1 - \frac{1}{\sqrt{1+\frac{\eta^2\omega^2}{m^2}}} \right)}. \tag{6.10}$$

In order to check Eq. 6.10, a DEM simulation describing Eq. 6.1 was run with a large chain length (in order to preclude reflections), and with the top particle excited by a Gaussian modulated sine pulse with center frequency ω. An arbitrary value for η was input into simulation. Then, the α coefficient was determined by fitting the simulated velocity decay rate to an exponential fit along the top portion of the chain after excitation. The value for α from simulation was compared with the value from Eq. 6.10 using the same system parameters, which resulted in good agreement. Thus, this method of estimating damping for the more simple cases was deemed accurate, and built upon for more complex cases, discussed below.

Additionally, it was useful to derive a relationship for damped wavespeed, since changing wave velocities were noted multiple times in the previous sections. Defining the damped phase velocity $c_d = \omega/\gamma_r$, we obtain:

$$c_d = \sqrt{\frac{ka\omega \left(1 + \frac{1}{\sqrt{1+(\frac{\eta}{m\omega})^2}} \right)}{2\sqrt{(\frac{\eta}{a})^2 + (\frac{m}{a})^2\omega^2}}}. \tag{6.11}$$

As a check, if η is set to zero, the undamped phase velocity $c = \sqrt{\frac{k}{m}}a$, is recovered.

6.2 Analytics for intersite damping

Figure 6.2 shows the model for intersite damping. The difference between this system and the previous system was the connection of the dampers, which were now connected from mass to mass, as opposed to from mass to a fixed boundary. This more accurately captured the desired system physics, although it also increased the complexity. Our aim was still to measure the decay rate from experiments so as to inform our DEM.

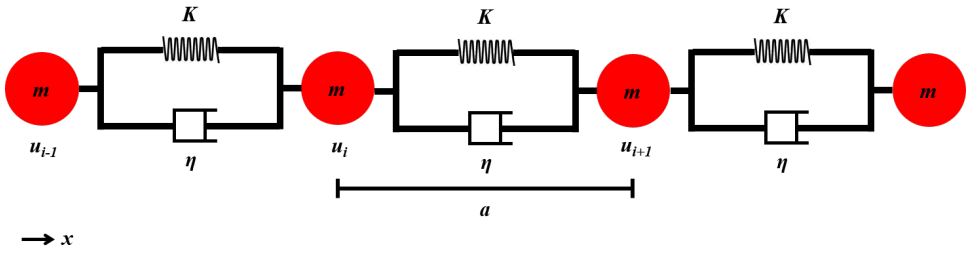

Figure 6.2: Intersite damping mass and spring model.

This system was described by the ODE below:

$$m\ddot{u}_i = k(u_{i+1} - 2u_i + u_{i-1}) + \eta(u_{i+1} - 2u_i + u_{i-1}). \tag{6.12}$$

As in the previous section, the second order finite difference formula was used to convert Eq. 6.12 to the following PDE:

$$m\frac{\partial^2 u}{\partial t^2} = a^2\frac{\partial^2}{\partial x^2}(ku + \eta\frac{\partial u}{\partial t}). \tag{6.13}$$

The following wave ansatz was applied:

$$u(x,t) = Ae^{i(\gamma_r + i\alpha)x - \omega t)}. \tag{6.14}$$

Substituting Eq. 6.14 into Eq. 6.13 resulted in:

$$m\omega^2 + a^2(\alpha - i\gamma_r)^2(k - i\eta\omega) = 0. \tag{6.15}$$

Eq. 6.15 was broken into real (Eq. 6.16) and imaginary parts (Eq. 6.17) and set equal to zero, resulting in:

$$a^2k\alpha^2 - a^2k\gamma_r^2 - 2a^2\alpha\gamma_r\eta\omega + m\omega^2 = 0 \tag{6.16}$$

and

$$-2a^2k\alpha\gamma_r - a^2\alpha^2\eta\omega + a^2{\gamma_r}^2\eta\omega = 0. \tag{6.17}$$

Solving Eq. 6.17 for γ_r resulted in two possible solutions:

$$\gamma_r = \frac{k\alpha \pm \sqrt{k^2\alpha^2 + \alpha^2\eta^2\omega^2}}{\eta\omega}. \tag{6.18}$$

The two solutions for γ_r from Eq. 6.18 were then substituted into Eq. 6.16. This resulted in four possible solutions for each value of γ_r used, for a total of eight possible solutions. However, only one, Eq. 6.19, resulted in real and positive values when real, positive trial values for η, k, ω, a, and m were input.

$$\alpha = \sqrt{\frac{-a^2km\omega^2(k^2+\eta^2\omega^2) + \sqrt{a^4m^2\omega^4(k^2+\eta^2\omega^2)^3}}{2a^4(k^2+\eta^2\omega^2)^2}}. \tag{6.19}$$

Solving Eq. 6.19 for η, resulting in four possible solutions as a result of the two plus/minus terms accompanying the radicals:

$$\eta = \pm\frac{\sqrt{-\frac{4km}{a^2\alpha^2} - \frac{8k^2}{\omega^2} + \frac{m^2\omega^2}{a^4\alpha^4} \pm \frac{\sqrt{-m^3\omega^{10}(8a^2\alpha^2k - m\omega^2)}}{a^4\alpha^4\omega^4}}}{2\sqrt{2}} \tag{6.20}$$

From inspection, two solutions could be discarded due to being negative, which left two possible solutions. Since it was necessary to find a single value for damping, further analysis was required. Thus, η was now solved in terms of γ_r, following the derivation of the same system from Kolsky [124]:

$$\eta = \pm\frac{\sqrt{\frac{4km}{a^2{\gamma_r}^2} - \frac{8k^2}{\omega^2} + \frac{m^2\omega^2}{a^4{\gamma_r}^4} + \frac{\frac{m}{a^2}^{\frac{3}{2}}\omega\sqrt{8{\gamma_r}^2k + \frac{m\omega^2}{a^2}}}{\gamma_r^4}}}{2\sqrt{2}} \tag{6.21}$$

From Eq.6.21, one value could be discarded due to being negative, resulting in the one remaining solution confirming which of the two solutions from Eq.6.20 was correct for the system. While this method was useful when exact parameters were known for the system (particularly the selection of a single value for ω),

it did not work well experimentally for confirmation of the correct η value from broadband impact. Thus additional methods were necessary to quantify damping from experimental broadband impact.

6.3 Dynamic mechanical analysis for damping determination

Based on the challenges in extracting damping from experiment and simulation (i.e. getting γ_r and α in order to find η), DMA was also used as a second source of information. It was necessary to derive a relationship between the outputs from DMA: storage modulus E', and loss modulus E'', with the damping value η, which was previously discussed.

First, we'll assume we have a mass-less chunk of elastic material used as a spring that is attached to a lumped mass, of some arbitrary dimensions: height H, depth d_1 and width d_2, where the system is shown by Fig. 6.3 and the equations of motion are:

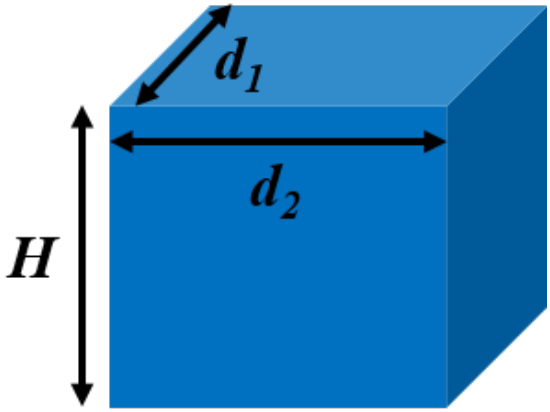

Figure 6.3: Massless chunk of elastic material with no inertial effects.

$$m\ddot{x} + kx = 0. \tag{6.22}$$

In Eq. 6.22, the stiffness term k can be related to the the dynamic modulus E^*

according to:

$$k = \frac{E^* d_2 d_1}{H}. \tag{6.23}$$

The dynamic modulus, used to describe a viscoelastic material in text [37], is made up of the storage modulus, E', and the loss modulus, E'' and is related by:

$$E^* = E' + iE''. \tag{6.24}$$

Substituting Eq. 6.23 and Eq. 6.24 into Eq. 6.22, results in:

$$m\ddot{x} = -(E' + iE'')(\frac{d_2 d_1}{H})x. \tag{6.25}$$

Now, we define $\tan(\delta)$ [37]:

$$\tan(\delta) = \frac{E''}{E'}. \tag{6.26}$$

Substituting Eq. 6.26 into Eq. 6.25 yields:

$$m\ddot{x} = -E'(\frac{d_2 d_1}{H})x - iE' tan(\delta)\frac{(d_2 d_1}{H})x. \tag{6.27}$$

Substituting the periodic loading condition $x = Ae^{i\omega t}$ (where A denotes an arbitrary amplitude) in into Eq.6.27 results in:

$$-m(\omega^2)x = -E'(\frac{d_2 d_1}{H})x - iE''(\frac{d_2 d_1}{H})x. \tag{6.28}$$

Now, we'll set aside Eq. 6.28 momentarily in order to describe a system for comparison. Thus, let's separately assume our system acts according to a Kelvin-Voigt model, as depicted in Fig. 6.4, and described by:

$$m\ddot{x} = -kx - \eta\dot{x}. \tag{6.29}$$

Assuming periodic motion, as before, yields:

$$m\omega^2 x = -kx - \eta i\omega x \tag{6.30}$$

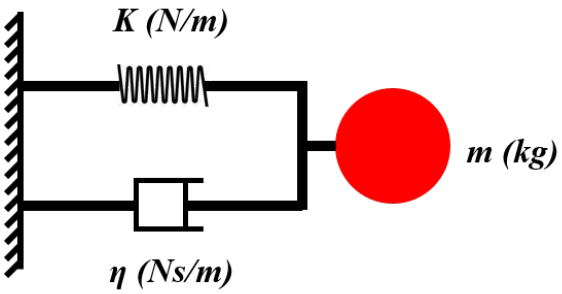

Figure 6.4: Kelvin-Voigt Model.

from Eq. 6.29. Comparing the final equations of the two systems, (Eq. 6.28 and Eq. 6.30), reveals similar forms which allows for the derivation of the following relationships that relate k and E' and η and E'':

$$k = E'(\frac{d_2 d_1}{H}), \tag{6.31}$$

and

$$\eta = \frac{E''}{\omega}(\frac{d_2 d_1}{H}). \tag{6.32}$$

Substituting Eq.6.31 and Eq. 6.32 into Eq. 6.26 yields:

$$\tan\delta = \frac{\eta\omega}{k}. \tag{6.33}$$

Equation 6.33 provides a method to relate $\tan\delta$ and η, which is useful for finding materials most suitable to high KE ratio performance in bistable materials, and also part of providing an additional method to estimate damping.

6.4 Recovering damping values from simulation

The following describes the method and an example of estimating damping from a simulated broadband impact, using the theory in Sec. 6.2 in combination with a Fourier transform and nonlinear exponential fitting of the decay rate of the velocity magnitude through the top portion of the sample. Equation 6.20 and Eq. 6.21 were used to estimate the η value after all other variables were input from

simulation. The only variable in these equations not known beforehand was α. An η value of 10 Ns/m was input for the equations of motion of the DEM, and the goal was to accurately estimate this value from the simulation output.

Figure 6.5 shows an example of this method of analysis for a simulated broadband impact by an 1.8 g impactor at 1.2 m/s impact velocity, which corresponded to $M/M_0 = 10^{-1}$ and $V/V_0 = 10^{-0.5}$. Set A parameters from Table 2.1 were used for an $N = 10$ sample. A velocity well below that estimated to cause negative stiffness as a result of dynamic impact was chosen in this example in order to minimize nonlinear effects. This chosen low velocity was based on the author's physical understanding that in a linear system the amplitude of a particular frequency would decay as it propagated through the damped material, without concern for the frequency conversion characteristic of nonlinear systems. The simulation time was set to 6.7 ms. The simulation time was set intentionally short in order to minimize interference in the measurement as a result of reflections and other interactions.

Figure 6.5(a) shows the velocity magnitude of the top layer (blue, layer 10) and the seventh layer (red), analyzed for the time shortly after impact. Layer selection was dependent on the amount of layers in the sample, and was a trade-off between obtaining enough sample points for a good fit of the decay rate, versus keeping the window of analysis small enough that reflections post impact would not interfere with the measurement. As a side note, the shape difference of the pulse between the top and bottom is one indication of how substantially the velocity pulse shape changes as it propagates through the material.

Figure 6.5(b) shows the amplitude of each frequency resulting from the fast Fourier transform (FFT) of the data in Fig. 6.5(a). The magenta star indicates the frequency that was chosen for further analysis. This frequency was chosen where there was less than an order of magnitude of amplitude decay from the maximum amplitude. Of note, the ratio of wavelength/sample height at this frequency is 0.93.

Figure 6.6 shows the decay of the amplitude of the chosen frequency from Fig. 6.5(b), as this frequency propagates from the top selected layer to the bottom. The amplitude is plotted on a logarithmic scale. This decay was fit to α from Eq. 6.14,

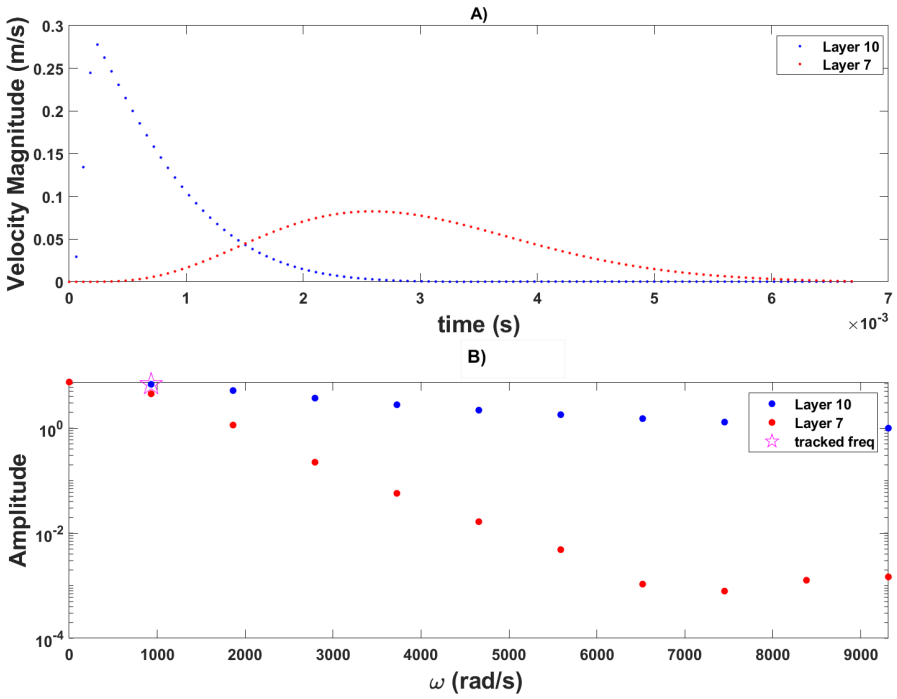

Figure 6.5: Diagram of chosen top layer (tenth layer) and seventh layer velocity pulse. a) Magnitude of the velocity pulse of the tenth and seventh layer, and b) the FFT information for those pulses.

then the "raw data" as well as the fit are plotted. The α from this fit was input into Eq. 6.20, which resulted in four values for η: ± 11.3 and ± 257.6. The negative values were eliminated since they did not match the physics of the system, leaving two possible values. The value for α was then input into Eq. 6.21, although as described previously, this equation was extremely sensitive to an accurate fit, and ostensibly for this reason it resulted in imaginary estimates for η, and was not useful.

The method shown above allowed the author to estimate the likely value of damping, although clearly this method was imperfect. In this example, the possible estimates for an input η of 10 Ns/m were 11.3 Ns/m and 257.6 Ns/m. While one estimate was quite close, the other clearly was not. Further analysis was thus necessary in order to down select from the remaining two possibilities: one method was through comparison with experimental DMA data, then the other

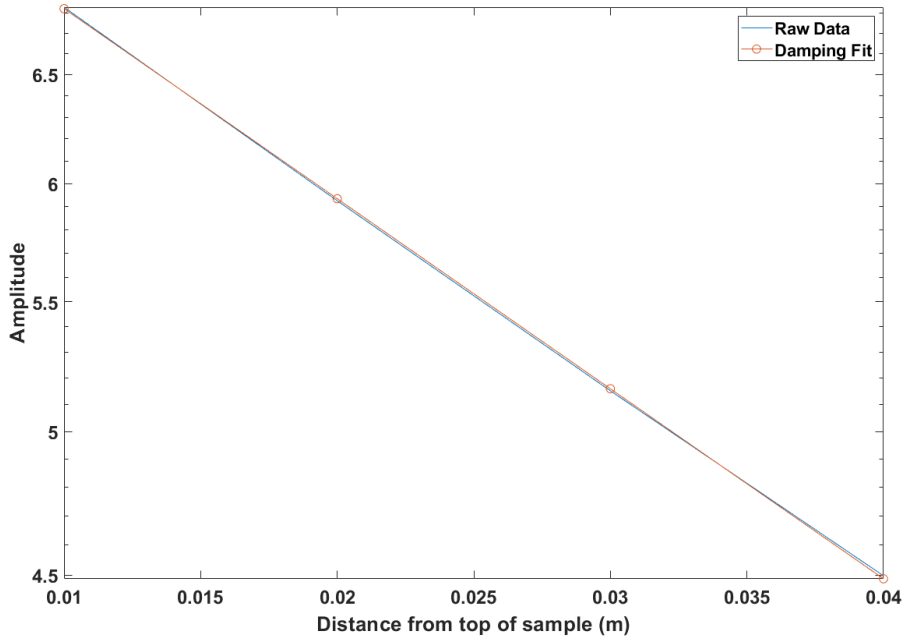

Figure 6.6: Decay of chosen frequency of FFT amplitude from the top picked layer to the bottom.

involved a qualitative comparison of XT diagrams. To a limited extent, this is further discussed with experimental results later in the manuscript, although precise, experimental determination of damping has been an extraordinary challenge to the author, and further analysis is left for future work.

6.5 Performance of the bistable system as a function of damping

The relationship between maximum KE ratio and damping was non-monotonic. Figure 6.7 shows maximum performance as a function of η values in a $N = 10$ layer sample, which indicated an optimum layer value of 3.34 Ns/m for the $N = 10$ sample. Using an η value less than this and the performance ratio declined steeply, while increasing past this value (to the maximum simulated η of 1000 Ns/m), resulted in a decline in performance as well. The simulation duration was 0.2409 s

($T_s \approx 24$, where linear wave transit time was taken from $\eta = 3.34$). The impactor mass was adjusted from $M/M_0 = 10^{-1.6}$ to $M/M_0 = 10^{0.4}$ using an exponential interval of 0.125, resulting in 17 values for M. The impactor velocity was adjusted from V_0 to $V/V_0 = 10^2$ using an exponential interval of 0.125, resulting in 17 values for V. This combination of M and V was different from any previous sweeps, and was chosen as a result of preliminary simulations in order to ensure the maximum KE ratio in a sweep was not at the top or bottom of the chosen impactor mass or velocity range for the sweep (e.g. Velocity: $V/V_0 = 1$ to $V/V_0 = 10^2$, or Mass: $M/M_0 = 10^{-1.6}$ to $M/M_0 = 10^{0.4}$). Of note, the maximum strain value in a layer was not considered in these simulations. The parameter $D_R = \eta V/k_L\varepsilon_2 a$ was defined to give a measure of damping in comparison to stiffness.

Figure 6.7(a) shows the maximum KE ratio values for 50 sweeps (each sweep is 289 simulated impacts) of impactor mass and velocity, as a function of η. The horizontal axis (showing η) is truncated at $\eta = 500$ Ns/m, because the maximum KE ratio stabilizes near $\eta = 1.5$ and does not significantly change as the value is increased further. Figure 6.7(a) indicates that maximum KE ratio performance is achieved at η values less than 50, which motivated further simulation at lower η values, shown in Fig. 6.7(b). Figure 6.7(b) shows the results where the η value was evenly spaced from $0.01 - 10$ Ns/m. This region was chosen because the maximum from the sweep shown in Fig. 6.7(a) occurred within this range. It is important to note that since each data point represented the maximum performance within a sweep of 289 different impact conditions, the mass and the velocity of impact associated with each of the data points was not the same. The case which resulted in the maximum KE ratio, (13.09x), occurred at impactor conditions $M/M_0 = 10^{-0.6}$ and $V/V_0 = 10^{0.75}$, and the η was 3.34 Ns/m.

In order to simplify the analysis, XT diagrams only at impactor conditions $M/M_0 = 10^{-0.6}$ and $V/V_0 = 10^{0.75}$ will be studied in this section, and η will be adjusted from the η shown to result in the maximum performance in order to observe the difference in system spatiotemporal behavior. The simulation duration for XT diagram analysis was reduced to 0.015 s, ($T_s \approx 1.5$, where linear wave transit time was taken from $\eta = 3.34$) because the KE maximums were occurring

within this simulation duration.

Figure 6.8 shows the results of $\eta = 3.34$ Ns/m ($D_R = 0.66$), with the impactor conditions $M/M_0 = 10^{-0.6}$ and $V/V_0 = 10^{0.75}$ (the optimal damping for these impactor conditions). Panels a) and c) show the bistable sample, while b) and d) show the linear sample. The KE ratio of the bistable sample is 13.09x. While resolution of the $N = 10$ case is less than that of the $N = 100$ cases previously studied, this amount of layers is directly relatable to the experimental samples (discussed later), and the following observations are noteworthy. In Panel a) we see kinetic energy that concentrates between the top of the sample for approximately the first 40 mm after impact. Additionally, from spring stretch (Fig. 6.8(c)) we see layer snapping (and remaining closed) in the same vicinity.

Figure 6.9 shows the results for the same conditions described for Fig. 6.8, except with decreased damping ($\eta = 2.23$ Ns/m, $D_R = 0.44$). The KE ratio was 6.27x. In contrast to Fig. 6.8(a), in Fig. 6.9(a) at least one unit cell in the region that was previously completely snapped shut, unsnaps. One indication of the snapping and unsnapping occurs at the bottom right corner of panel a), where an initial wave pulse is seen in yellow, moving from right to left, with several "offshoots" of this pulse moving off the original pulse in light blue from left to right.

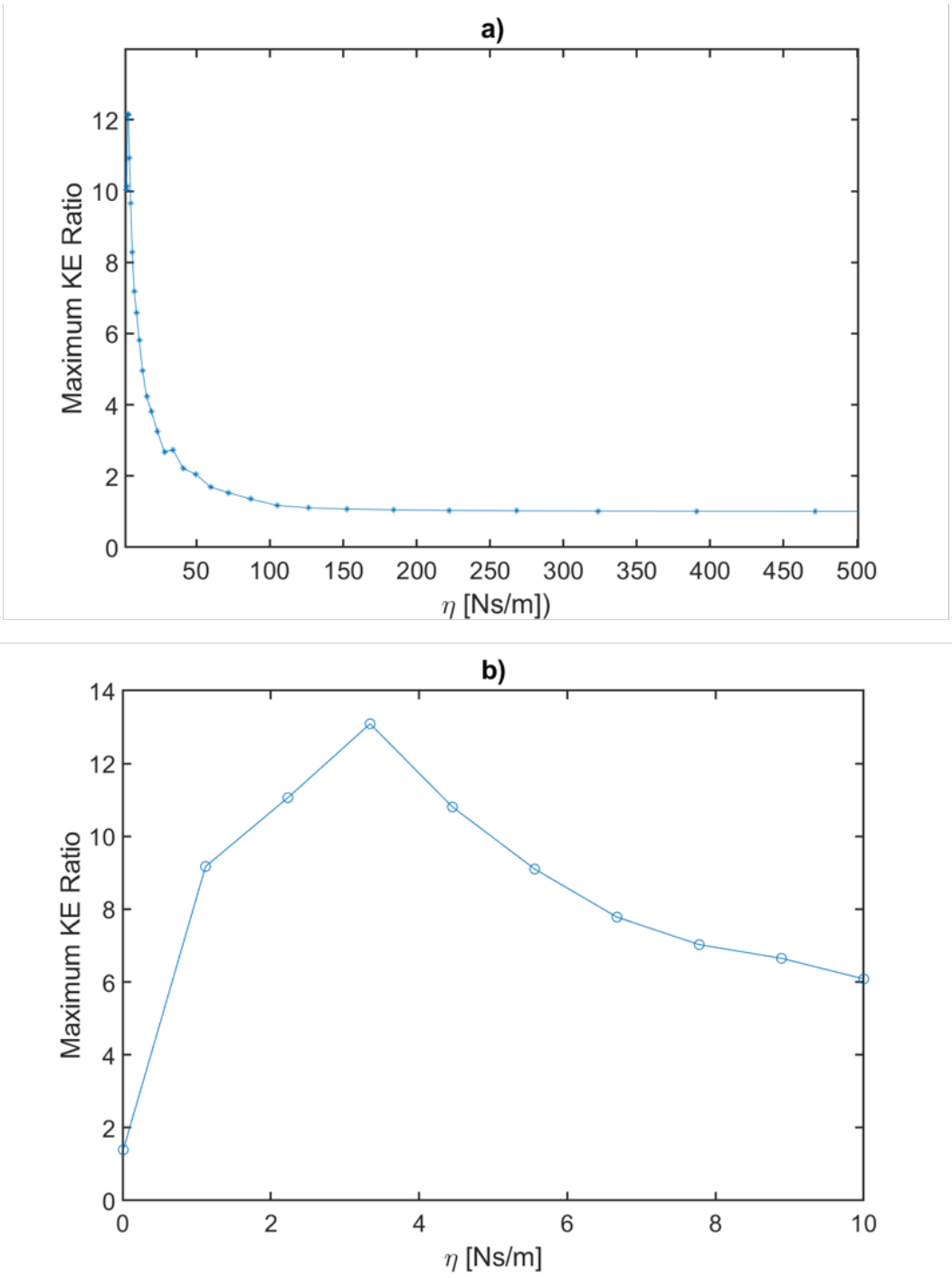

Figure 6.7: The impactor conditions were: $M/M_0 = 10^{-1.6}$ to $M/M_0 = 10^{0.4}$, and $V = V_0$ to $V/V_0 = 10^2$. The simulation duration was 0.2409 s ($T_s \approx 24$). Panel a) shows a broader range sweep of η values, while b) shows a separate sweep focused near where maximum KE ratios were seen in the previous sweep. In b), the η value of 3.34 Ns/m is where maximum KE ratio performance of 13.09x was observed.

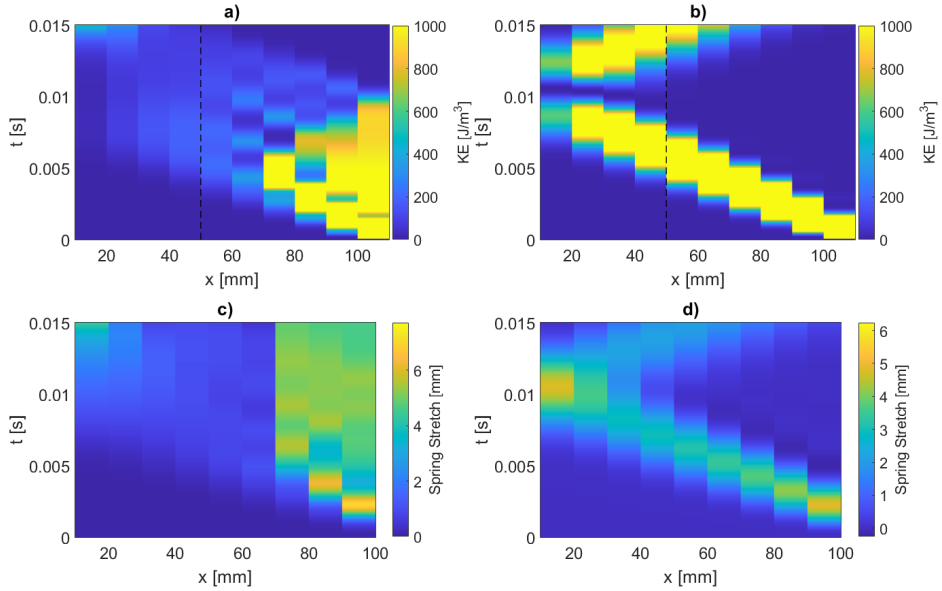

Figure 6.8: , $\eta = 3.34$ Ns/m ($D_R = 0.66$), $T_s \approx 1.5$. The KE ratio was $13.09x$. The maximum KE value in the colorbar in (a,c) was divided by 38.6.

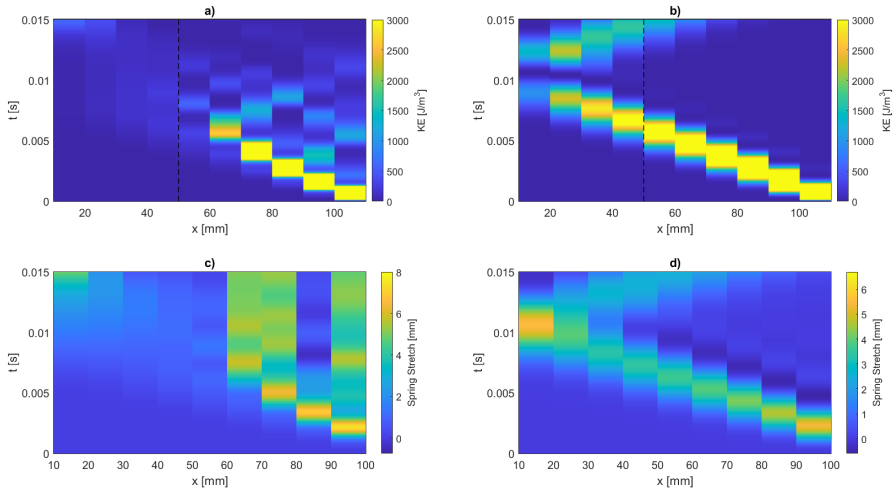

Figure 6.9: The KE ratio was 6.27x. The maximum KE value in the colorbar in panel a) and c) was divided by 12.9.

Figure 6.10 shows the results if the damping value is reduced again from the previous value, to a damping value of $\eta = 1.12$ Ns/m ($D_R = 0.22$). Unlike the previous two examples, in Fig. 6.10(a), a high amount of KE propagates through the half sample point, resulting in a low KE ratio of $0.7x$. One explanation for this low ratio is shown in Fig. 6.10(c) where, unlike the previous two examples, the spring stretch plot in this example does not indicate permanent or semi-permanent snapping of the layers prior to the half sample point. Instead, the layer snaps, then unsnaps as the adjacent layer snaps and again unsnaps, forming a transition solitary wave.

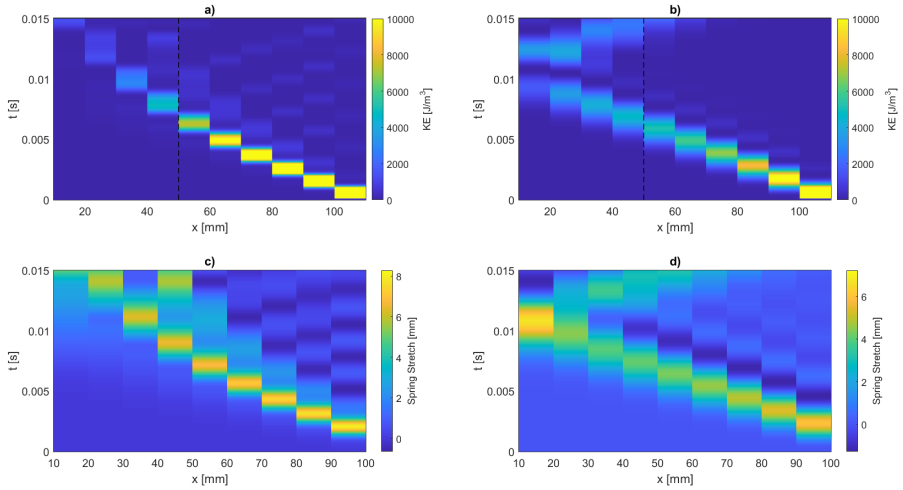

Figure 6.10: The KE ratio was $0.7x$. The maximum KE value in the colorbar in (a,c) was divided by 3.86.

Figure 6.11 shows the results when $\eta = 0.1$ Ns/m ($D_R = 0.02$). In comparison to Fig. 6.10(a), in Fig. 6.11(a) a more clear solitary wave type propagation is seen. Comparing the bistable spring stretch plots (panel c) in both figures), shows a more abrupt region where the layers snap, then unsnap in the example with less damping. This is particularly clear in Fig. 6.11(c), where for the duration of the initial pulse, a compression of approximately eight mm is seen, followed by an abrupt rebound of approximately four mm in tension. The "tensile rebound" was not seen in the previous examples in this section, and appears to indicate sub-optimal damping for the performance conditions sought by the author. The

KE ratio was 0.29x.

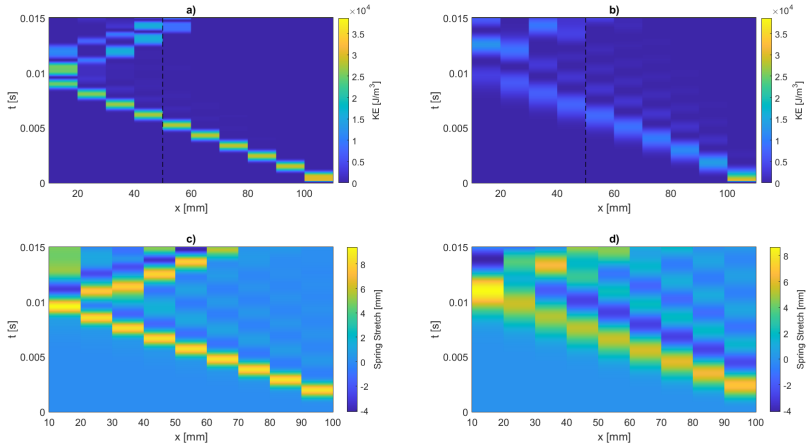

Figure 6.11: Kinetic energy and spring stretch of $N = 10$ bistable (a,c) and linear (b,d) samples at impactor conditions $M/M_0 = 10^{-0.6}$ and $V/V_0 = 10^{0.75}$ for $\eta = 0.01$ Ns/m ($D_R = 0.02$). The KE performance ratio (linear/bistable) is $0.29x$.

The next figures show the results when η is increased above 3.34 Ns/m. Of note, damping values were incrementally increased above $\eta = 3.34$, with values of $4.45 - 10$ simulated ($D_R = 0.88$ to 1.98). Qualitatively, these damping values resulted in similar bistable sample behavior as was seen in Fig. 6.8, in that an initial KE wavefront decayed prior to the half sample, then spring stretch indicating "permanent" snapping (for the time period shown) for several initial layers of the lattice. However, observed permanent spring stretch appeared to decrease with increasing damping value, although the observed values were greater than ε_2. Likewise, while KE ratio was above one in all cases, the KE ratios decreased with increasing damping: $9.26 - 4.49x$ for all η values. It was chosen to show Fig. 6.12 as one example of this behavior.

Figure 6.13 shows the results when η is increased to 100 Ns/m ($D_R = 19.8$). Most notably, comparison of bistable (Fig. 6.13(a,c)) and linear (Fig. 6.13(b,d)) reveals both samples are extremely similar, including the KE ratio of $1x$.

Clearly the magnitude of damping for a given set of impactor conditions strongly influences KE ratio performance. It appears that near "optimum" damping, (e.g. Fig. 6.8, with the highest KE ratio), the damping value is low enough that some

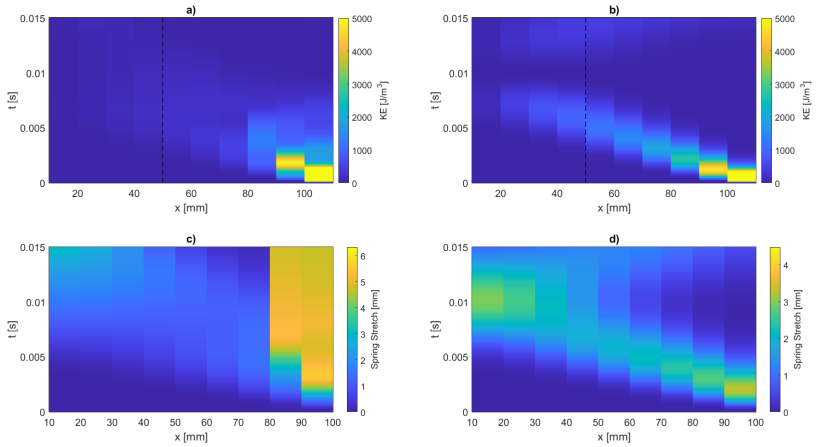

Figure 6.12: The KE ratio was 4.49x. The maximum KE value in the colorbar in (a,c) was divided by 7.72.

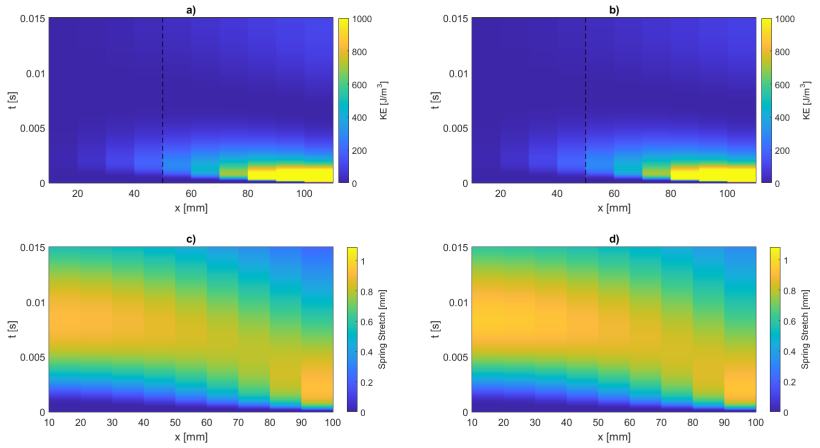

Figure 6.13: The KE performance ratio (linear/bistable) is $1x$. The maximum KE value in the colorbar in (a,c) was divided by 38.6.

(or many) of the top layers of the bistable sample are able to snap to their second stable state. However, the damping is also high enough that there is resistance to these layers "snapping" back, and re-releasing energy. This "optimum" damping occurs at $D_R = 0.66$. When damping is sub-optimally low, (e.g. Fig. 6.11), while layers snap to their secondary state, they appear to forcefully unsnap (as indicated by $\varepsilon_L \approx .4$ in tension), and the resulting solitary wave transmits a high level of KE density, resulting in the worst performance ($D_R = 0.02$ in the worst perfor-

mance case). When the damping is sub-optimally high (e.g. Fig. 6.13), the spring stretch is distributed fairly evenly across the bistable sample and the maximum layer strain in any bistable layer is not sufficient for any "snapping" to occur. In these sub-optimally high damping cases, the KE ratio ≈ 1, and D_R is much greater than one.

6.6 Damping: Ashby chart and relations back to theory for damping values

The highest performance occurred in the $N = 10$ sample in the previous section when $\eta = 3.34$. It was useful to relate this back to $\tan\delta$ (defined in Eq.6.33) in order to better understand materials that can be used to make the lattice that will maximize the performance of the bistable design. Since the impacts are broadband, Eq. 6.33 was only useful if a "dominant" frequency was estimated. This estimation was done by estimating the time of the initial velocity pulse at impact T_p, then using the equation $\omega = 2\pi/T_p$ to estimate frequency. For the $N = 10$ sample at the 8th layer (chosen near the top to avoid reflection interference, but not the top to minimize boundary effects), $T_p \approx 4$ ms at impact conditions for maximum KE ratio: $M/M_0 = 10^{-0.6}$ and $V/V_0 = 10^{0.75}$, and $T_p \approx 3.7$ ms at impact conditions to avoid nonlinear effects M_0 and $V/V_0 = 10^{-0.5}$. Inputting $k_L = 2.26e4$ N/m into Eq.6.33 resulted in $\tan\delta \approx 0.23$ at impact conditions: $M/M_0 = 10^{-0.6}$ and $V/V_0 = 10^{0.75}$ and $\tan\delta \approx 0.25$ at the lower energy impact conditions: M_0 and $V/V_0 = 10^{-0.5}$.

An "Ashby chart" gives some idea of materials with similar $\tan\delta$ properties. The Lakes viscoelastic materials textbook will plot materials in two dimensional space with Young's Modulus (E) on the vertical axis and $\tan\delta$ on the horizontal axis [37]. Materials in the bottom right of the plot have high damping values, and include gels, foam rubber, and rubber [37]. In the top left of the plot are very low damping, high strength materials like ceramic single crystals. In the upper and middle portions of the plot are materials with medium damping values and high to medium strength, such as structural metals, soft metals, and polymers [37].

The $\tan\delta \approx 0.25$ corresponds to materials such as rubbers, foam rubber, and polymers [37], indicating these materials may be a good choice for an $N = 10$ production sample. It is important to note however that this value largely depends on the estimate of "dominant" frequency, as described above, which inherently has error.

As a limited comparison with the $N = 10$ example and its associated $\tan\delta$ estimate, a simulation of the $N = 100$ sample was checked at impact conditions that corresponded to "good" performance: $M/M_0 = 10^{-0.625}$ and $V/V_0 = 10^{0.25}$ (shown in Fig. 3.16). Here $T_p \approx 4.2$ ms at impact conditions: $M/M_0 = 10^{-0.625}$ and $V/V_0 = 10^{0.25}$, or $T_p \approx 3.7$ ms if impact conditions M_0 and $V/V_0 = 10^{-0.5}$ were used (the 98th of 100 layers was tracked for velocity). Using values $k_L = 2.26e5$ N/m and $\eta = 0.164$ Ns/m resulted in $\tan\delta \approx 0.0011$ at impact conditions: $M/M_0 = 10^{-0.625}$ and $V/V_0 = 10^{0.25}$ and $\tan\delta \approx 0.0012$ at the lower energy impact conditions: M_0 and $V/V_0 = 10^{-0.5}$. Referencing again an Ashby chart, materials such as soft metals and structural metals have $\tan\delta \approx 10^{-3}$

While a far more rigorous amount of simulation varying η was completed for the $N = 10$ layer examples than the $N = 100$ sample, it appears that when N differs, the optimum $\tan\delta$ for that N likely differs as well. Now, given some basic understanding of how $\tan\delta$ relates to the performance of the lattices under study, the following discussion is noteworthy, as it potentially indicates a fundamental challenge which may be overcome by the use of bistable materials. For example, it is understood that for a given geometry, increasing the elastic modulus will increase the elastic strain energy trapping potential. It is also understood that in terms of suitability to impact, a tough material is desired. It was also shown in Sec. 6.5 that the performance of the bistable system in simulation is dependent upon damping, and particularly in the case of "high N", the samples appear to perform well at lower damping values. Thinking in terms of an Ashby plot, the tough, high modulus materials tend to lie on the left side of the chart, where we have a low loss tangent, indicative of low material damping. Thus, the potential benefit of bi-stability in terms of impact mitigation becomes more clear: it allows for the utilization of medium to high toughness, medium to high modulus struc-

tural materials (with low to medium $\tan\delta$ values), and augments these properties with energy trapping through the mechanism of structural bi-stability to offset the lower intrinsic material damping properties. However, this bistable mechanism ostensibly has the limitation that the materials used for its construction need to be "tuned" such that their damping yields optimum performance. This is particularly challenging task, since it appears that performance is dependent upon both damping and N, and the "optimum" damping for one N value is not the same as the optimum damping for another N value.

Chapter 7

Effect of post buckled stiffness on performance

Motivated by previous research from Katz and Givli [107], there was potential benefit in terms of energy trapping by engineering the force displacement response of a layer such that the post-buckled stiffness was less than the pre-buckled stiffness. Through numerical and theoretical analysis of a reduced order system, Katz and Givli showed through a tri-linear piecewise model, that systems composed of post-buckled springs which were stiffer had a tendency to propagate solitary waves, while systems with softer postbuckled springs had a tendency to capture the energy through oscillations within the first approximately 40% of the lattice [107]. Expanding this idea further by fitting the quasi static force versus displacement curve to a continuous polynomial model, an investigation was made into the KE ratio performance effects at varying impactor V and M combinations through simulation when the force versus displacement response of a DEM layer was altered such that the post-buckled stiffness was less than the pre-buckled stiffness.

The current unit cell design (Fig. 2.2) showed higher post-buckled stiffness than pre-buckled stiffness (Fig. 2.4). One major contributing factor to this is that after the cell transitions to its second stable state, the monolithic parts of the unit cell come into contact with each-other, drastically increasing the stiffness. Addressing this challenge of altering the current unit cell design is left for future work. Instead, the strain energy versus displacement curve from the $\theta = 60$ degree beam displaced

through FEM (shown in Sec. 2.7) was used as a baseline, then differentiated with respect to displacement in order to get force versus displacement (Set C in Table 2.1 contains the coefficients describing this "unsoftened" data fit to a 3rd order polynomial). Now, referencing compression, beginning at the point this curve went into its secondary positive stiffness regime, the original data was replaced by scaled force data of lower magnitude, and a vertical intercept value was used to match up the original and scaled data. The original data and secondary stiffness data was combined, then this piecewise function was fit to a continuous fifth order polynomial as described in Sec. 2, with the resulting coefficients described by set D in Table 2.1. A comparison of the resulting force versus displacement curves from set C and set D data is shown in Fig. 7.1.

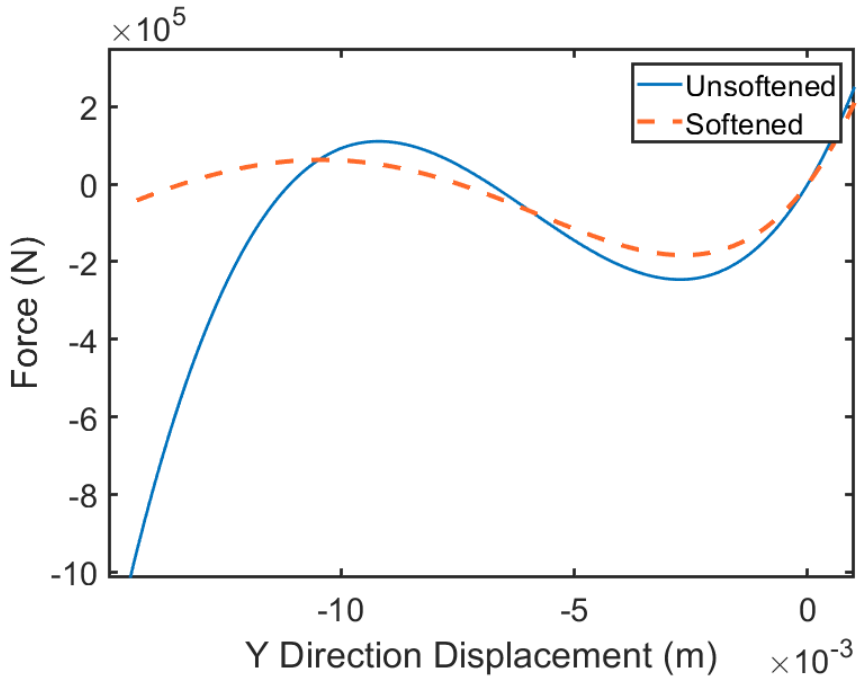

Figure 7.1: Force versus displacement curve describing a single 8 mm beam from FEM fit to a polynomial function using set C coefficients (blue) and set D coefficients (softened post-buckled stiffness) in dashed red.

A fifth order polynomial function (no zeroth order term, as before) was chosen because it resulted in a post buckled stiffness which was less than the pre-buckled stiffness. This fifth order curve also maintained a positive stiffness value at higher

strain in compression, which was the desired physics to model. Kinetic energy ratio results from simulations using set D coefficients were compared to results using set C data in order to compare the KE ratio performance between the two systems. Of note, since ε_0 affected V_0 and ε_2 affected M_0 and the curve fits for set C and set D data had slightly different ε_0 and ε_2; this resulted in a comparison of different nominal impact conditions for each of the two sweeps conducted (Set D: $V_0 = 564.5$ m/s, $M_0 = 34.1$ g, Set C: $V_0 = 628.8$ m/s, $M_0 = 30.7$ g). However, both curves were bistable at zero load, and the control (Set C) curve had higher predicted quasi-static strain energy trapping than the softened curve (5.42 kJ vs 6.08 kJ). Furthermore, the KE ratio performance of set C data was poor a high velocity impact conditions (Fig. 7.2) while set D still performed well (Fig. 7.3). Thus the fit differences and difference in nominal impact conditions were deemed adequate for a comparative analysis.

Figure 7.2 shows the sweep of maximum KE performance using set C coefficients for the force displacement response. The simulation duration was 24.9 μs ($T_s \approx 6.2$), and $N = 100$. Since set C and set D data resulted in different linear stiffness values, damping was set by matching the layer quality factor damping value to $Q = 100$. The maximum KE ratio was 30.9x, at impactor conditions: $M/M_0 = 10^{-0.25}$ and $V/V_0 = 10^{0.25}$.

Figure 7.3 shows the sweep of maximum KE performance using set D (softened) coefficients for the force displacement response. The simulation duration was 24.9 μs ($T_s \approx 6.2$), $N = 100$, and $Q = 100$. The maximum KE ratio was 75.75x, at impactor conditions: $M/M_0 = 10^{-0.375}$ and $V/V_0 = 10^{0.5}$. The maximum KE ratio of the sweep using the softened coefficients was 2.45x higher than the maximum KE ratio in the unsoftened sweep.

Further analysis looked at individual XT diagrams from cases of particular interest. The maximum performance case from Set D (softened) data was at impactor conditions: $M/M_0 = 10^{-0.375}$ and $V/V_0 = 10^{0.5}$, and is shown below in Fig. 7.4. Note that while maximum layer strain was not limited in this simulation, post processing revealed the maximum strain in the bistable sample did exceed one for these impactor conditions.

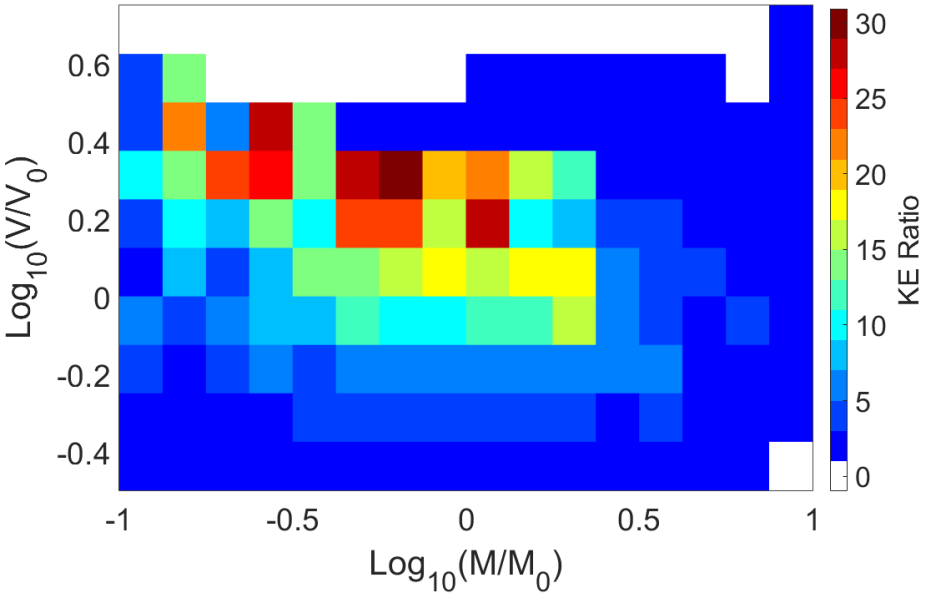

Figure 7.2: The maximum KE ratio was 30.9x, at impactor conditions: $M/M_0 = 10^{-0.25}$ and $V/V_0 = 10^{0.25}$.

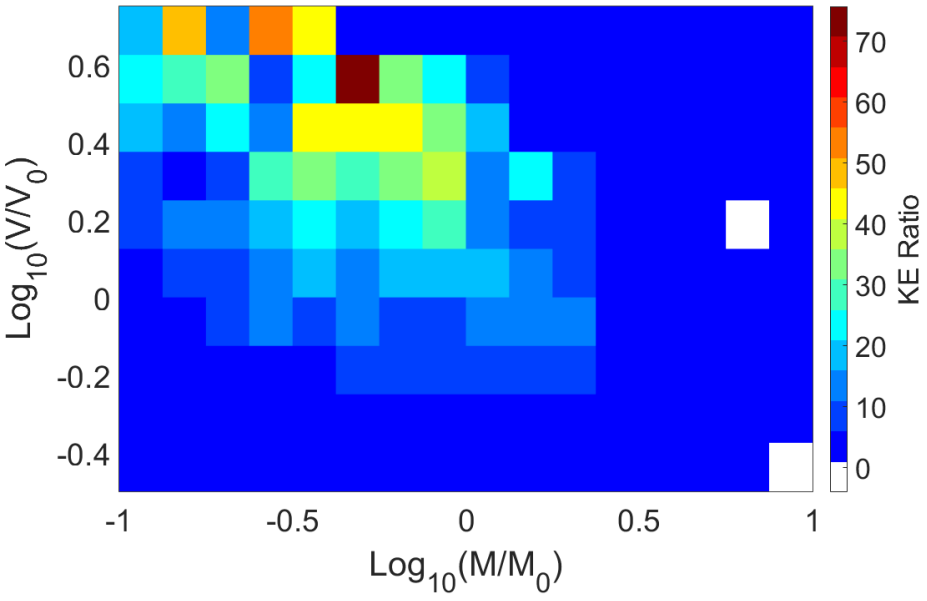

Figure 7.3: The maximum KE ratio was 75.75x, at impactor conditions: $M/M_0 = 10^{-0.375}$ and $V/V_0 = 10^{0.5}$.

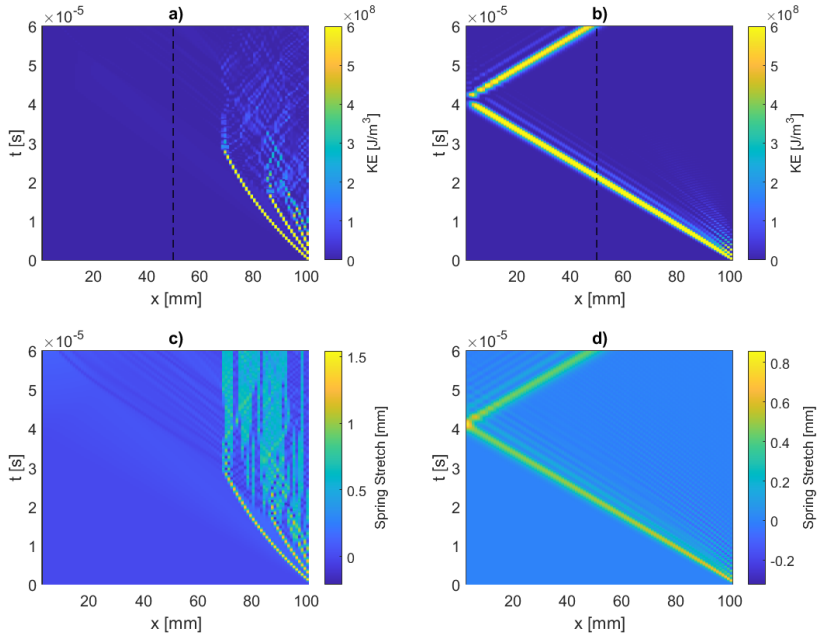

Figure 7.4: Kinetic energy density XT diagram for $N = 100$ sample, with $Q = 100$ damping, using set D (softened) data at impact conditions: $M/M_0 = 10^{-0.375}$ and $V/V_0 = 10^{0.5}$. The maximum KE ratio was 75.75x. a,c) Bistable sample. b,d) Linear sample.

Figure 7.4(a,b) show KE density and spring stretch for the bistable sample, and panel b) and D show the same information for the comparative sample. As has been seen previously in examples exhibiting high KE ratio performance, in panel a) we see a wave-train of multiple solitary waves, which initially propagate while slowing (ostensibly the slowing is a result of the effects of damping), then transition to the oscillatory phase prior to the half sample (KE ratio measurement) point. The spring stretch diagram in Fig. 7.4(c) shows a large amount of "permanent" (i.e. for the duration of the time shown in the diagram) spring stretch, indicative of layers that stay snapped, which is also associated with good performance. Of note, the kinetic energy ratio of 75.75x is based on a wave that crosses the half-sample point at time $9.82E-5$ s, well past the initial wavefront (and not shown in the diagram). If only the time from $T_s = 0$ to $T_s \approx 1$ is considered, the KE ratio is 102.2x. This is shown in Fig. 7.5.

Figure 7.6 shows the XT diagram using the set C (unsoftened) data at impactor

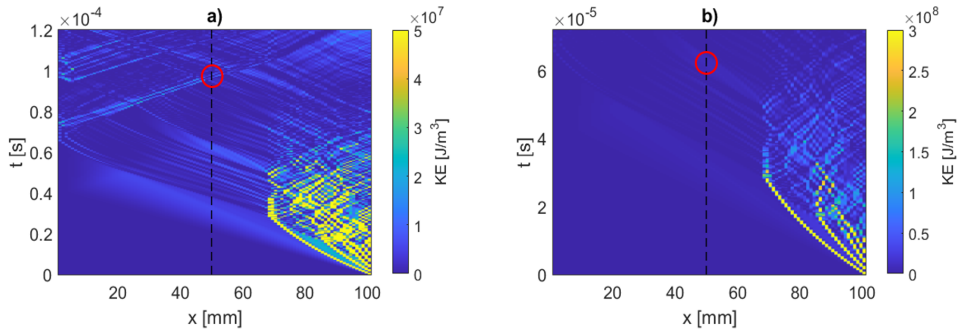

Figure 7.5: In b) the time axis is adjusted to show the "local" KE density maxima if only the time from $T_s = 0$ to $T_s \approx 1$ is considered, which results in a KE ratio of 102.2x. a) shows the KE density maxima if the whole simulation duration is considered ($T_s \approx 6.2$), resulting in the KE ratio of 75.75x, previously noted in Fig. 7.4(a). The red circles indicate the point of maximum KE density collection at the half-sample.

conditions: $M/M_0 = 10^{-0.375}$ and $V/V_0 = 10^{0.5}$, for comparison with Figures 7.4 and 7.5). The remaining conditions: $N = 100$ sample, $Q = 100$ damping, $T_s \approx 6.2$, are the same as the previous example showing the softened data. Figure 7.6(a,c) shows the KE density and spring stretch for the bistable sample, and panel b) and D shows the same information for the linear sample. In Fig. 7.6(c), despite showing some "permanent" (i.e. for the duration of time shown in the figure) layer snapping prior to the collection point, Fig. 7.6(a) shows the trespass of the initial kinetic energy solitary wave across the half point of the sample, which results in the low KE ratio of 0.8072x.

Thus, it appears that tailoring unit cell response such that post-buckled stiffness is lower than pre-buckled stiffness is correlated to potentially substantial performance improvement, as indicated by the over 2x improvement in maximum KE ratio performance from the softened design. However there are significant challenges and considerations necessitating further study. For instance, the softer post buckled stiffness relationship of the softened design doesn't match well with the stiffening from unit cell self contact. In order to avoid self contact, the range of V would likely be reduced significantly, which would make performance of the softened design less advantageous, or even worse than the unsoftened in many instances. Additionally, the limited comparison performed herein only considered

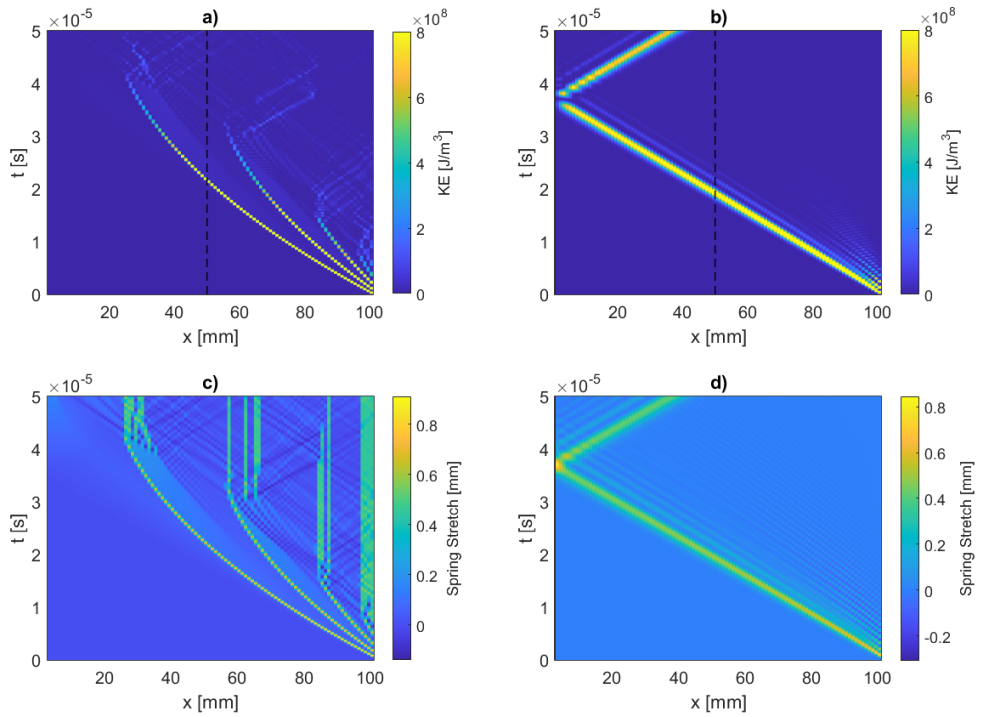

Figure 7.6: Kinetic energy density XT diagram for $N = 100$ sample, with $Q = 100$ damping, using set C (unsoftened) data at impact conditions: $M/M_0 = 10^{-0.375}$ and $V/V_0 = 10^{0.5}$. The maximum KE ratio was 0.8072x. a,c) Bistable sample. b,d) Linear sample.

one Q factor damping value; it is possible that "tuning" the performance of both the softened and unsoftened systems to optimum damping for each system would result in a substantially different results. Finally, only the results of a single softened curve (set D) were used– further refinement of post buckled stiffness within the "softened" post buckled stiffness regime could also yield different results.

Chapter 8

Use of kinetic energy as the comparative metric

The variables used in this chapter apply to this chapter only. In wavelike motion within a conservative (i.e undamped) linear system, one would expect a tradeoff of kinetic and potential energy to occur such that for a given point in space, the energy density computed due to KE and PE would be the same. As an example of this, the equations for energy density within an un-damped string from text [123] are referenced. Here, if we describe a system where we have a rightward propagating, one dimensional wave (that does not distort), and assuming small deflections of the string we can describe the KE in segment x_1 to x_2 by:

$$K(t) = \frac{1}{2}\int_{x_1}^{x_2} \rho \dot{y}^2 dx. \tag{8.1}$$

In Eq. 8.1, t denotes time, $K(t)$ kinetic energy, ρ linear density (mass per unit length), and y displacement of the string. Similarly, we can describe the energy density k of this one dimensional system by:

$$k(x,t) = \frac{1}{2}\rho \dot{y}^2. \tag{8.2}$$

Through a similar derivation in Ref. [123], the PE of the same segment is described by:

$$V(t) = \frac{1}{2}\int_{x_1}^{x_2} T(\frac{\partial y}{\partial x})^2 dx, \tag{8.3}$$

where T is the string tension. The PE density is described by:

$$v(x,t) = \frac{T}{2}(\frac{\partial y}{\partial x})^2. \tag{8.4}$$

If we now proceed with the derivation only in terms of energy density, we can describe TE density:

$$\epsilon(x,t) = \frac{1}{2}\rho\dot{y}^2 + \frac{T}{2}(\frac{\partial y}{\partial x})^2. \tag{8.5}$$

If we assume the wave is only rightward propagating, the D'Alembert solution describing the displacement of the propagating wave is given by:

$$y(x,t) = f(x - c_0 t), \tag{8.6}$$

where c_0 is the wavespeed. Thus, if we input Eq. 8.6 into Eq. 8.2 and Eq. 8.4, we yield:

$$k(x,t) = \frac{1}{2}\rho c_0^2 f'(x - c_0 t)^2, \tag{8.7}$$

representing KE density, and:

$$v(x,t) = \frac{1}{2}T f'(x - c_0 t)^2, \tag{8.8}$$

representing TE density. Now, using the known relationship between linear wavespeed, tension, and density ($c_0 = \sqrt{T/\rho}$), Eq. 8.7 and Eq. 8.8 are equal.

Based on the the theoretical framework described above, it was initially expected that ratios of either the maximum PE (linear/bistable), KE (linear/bistable), or TE (linear/bistable) should all yield the same results. However, this expectation was demonstrated to not be correct. For instance, Fig. 8.1 shows the results of the same sweep, where Fig. 8.1(a) shows the TE ratio, and Fig. 8.1(b) shows the KE ratio. Simulation parameters used were: Set A from Table 2.1, $N = 100$, $\eta = 0.164$ Ns/m, and simulation duration 0.03s ($T_s \approx 3$). While qualitatively the

areas where the bistable beam outperforms the linear beam are described similarly, the ratios are clearly different, thus warranting further investigation.

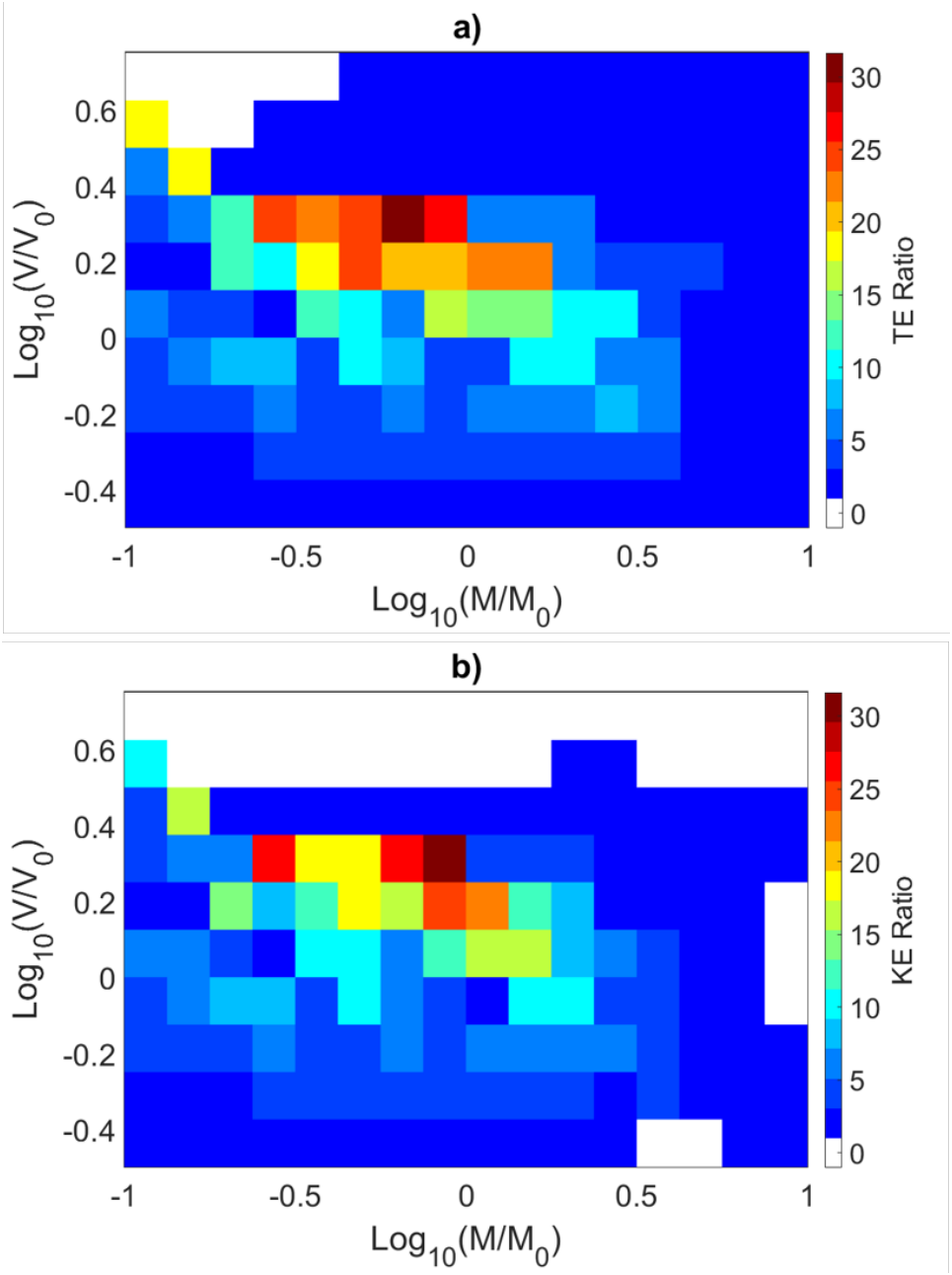

Figure 8.1: (a) Differences in TE ratio and (b) KE ratio from the same sweep.

Thus a nonlinear wave explanation was sought. We begin with the Korteweg-de Vries (KdV) equation, used to describe nonlinear waves. As derived in text [111],

for water waves in a shallow channel, using a moving reference frame, and variables: ϕ, the surface height above the equilibrium level divided by the depth of the fluid, ξ, a non-dimensional spatial variable, and τ, the non-dimensional time variable:

$$\frac{\partial \phi}{\partial \tau} + 6\phi \frac{\partial \phi}{\partial \xi} + \frac{\partial^3 \phi}{\partial \xi^3} = 0. \tag{8.9}$$

One solution to this differential equation is:

$$\phi = A \operatorname{sech}\left[\sqrt{\frac{A}{2}}(\xi - 2A\tau)\right]^2. \tag{8.10}$$

Assuming $A = 1$, then deriving Eq. 8.10 into PE density yields

$$pe(x,t) = T \operatorname{sech}\left(\frac{-2\tau + \xi}{\sqrt{2}}\right)^4 \tanh\left(\frac{-2\tau + \xi}{\sqrt{2}}\right)^2, \tag{8.11}$$

and deriving Eq. 8.10 into KE density yields

$$ke(x,t) = 4\rho \operatorname{sech}\left(\frac{-2\tau + \xi}{\sqrt{2}}\right)^4 \tanh\left(\frac{-2\tau + \xi}{\sqrt{2}}\right)^2. \tag{8.12}$$

Equation (8.11) and Eq. (8.12) are identical, with the exception of their magnitude. Thus it appears the linear wave derived understanding of the equality between potential and kinetic energy densities does not hold in the nonlinear case described by the KdV equation and the spatially localized solution.

Kinetic energy (density) was chosen as the metric, based on the explanation above, because: 1) it was easily measurable and comparable between simulation and experiment (digital image correlation measured the deformation and rate of deformation) and also because the dissipation of kinetic energy was cited as an important function of ballistic and damage prevention, and thus it is particularly relevant [30, 54, 125].

Chapter 9

Impact experiments

The majority of effort in this work was related to simulation. However, limited experimentation was done through the use of a constructed "flyer-plate" impact testing device. An additional goal was to pave the way for future experimental work using lattices of smaller unit cell sizes and different materials in order to validate the results from simulation. This section will discuss this experimental work, as well as information the author hopes is useful for improvements to the lattice for additional experimental testing. The experimental section will be arranged in order to first discuss the experimental methodology, as well as the flyer-plate design used for experimentation. Then, the production of the designed bistable sample and comparison sample, as well as the experimental results will be discussed. Finally, several methods to alter the stiffness between the monolithic and portions of the unit cell designed to bend will be discussed; this section is useful for future work in order to produce a single material lattice of similar design which would allow for more production options, and the production of lattices with smaller unit cells.

9.1 Experimental setup for impact

Multiple tests were conducted using a custom built flyer-plate impact tower (Fig. 9.1), wherein the sample and flyer were recorded using a high-speed camera ($100 - 200$ KHz tested frame rate) and analyzed through digital image correlation (DIC).

Figure 9.1 shows the test rig, modified by the author for bistable impact testing. This impact system was composed of a thick, polycarbonate plunger attached to two linear bearings, guided by two guide rods. Springs were affixed to the rods such that when a winch was actuated the plunger was pulled upwards to compress springs mounted co-axially around the guide rods. A system of cable ties were used to provide an attachment point for a winch to the plunger (Fig. 9.1(b), cable ties are black and form a triangle), where a navy clasp was used to provide a severable link between the cable ties and winch. Once the plunger was tensioned appropriately, an electromechanical switch triggered an additional pulley that triggered the navy clasp release, sending the plunger down towards the sample below. At the bottom of the plunger, an aluminum flyer-plate (of impact contact area d^2) was affixed weakly with hot melt adhesive (HMA). Just prior to sample impact, the flyer-plate broke a LASER beam, which sent the trigger signal to the high speed camera. Figure 9.1(a) shows an overview of the camera, tower, and high intensity broadband light system. Figure 9.1(right panel) shows a closeup of the impact area.

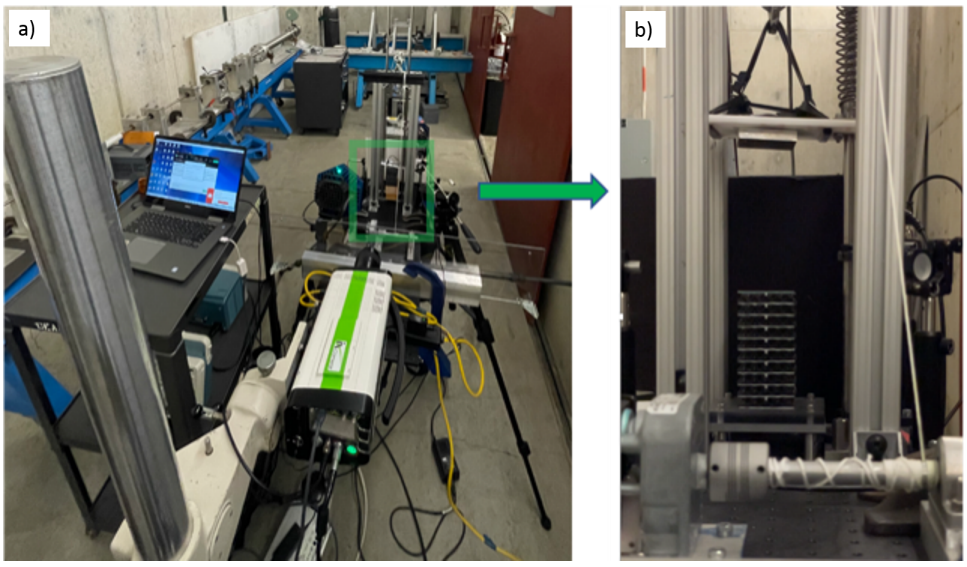

Figure 9.1: Custom built flyer-plate impact tower and high speed camera setup. a) shows a overview of the camera, tower, and high intensity broadband light system. b) shows a closeup of the impact area with a test sample loaded.

In order to control the energy imparted to the sample in a precise and easily

measurable manner, special care was taken to avoid resonance of the impactor. For instance, in early iterations of the impactor design, a polycarbonate impactor was used instead of the aluminum design. When using the polycarbonate impactor, the first bending resonance of the plate was activated, manifesting itself as an apparent increase in total energy into the system (assuming the flyer-plate had kinetic energy based on it's rigid body velocity) even after initial contact between the flyer-plate and sample, as the plate cyclically pushed on the sample. The current impactor design avoided this conflict using a first bending mode analysis, beginning with equation [126]:

$$\omega = (bl^2)\sqrt{\frac{EI}{\rho A l^4}}. \tag{9.1}$$

where l is beam length, E is Young's Modulus, I is the moment of inertia, A is impactor area, and ρ is density. For the first mode shape, with free-free beam end conditions, the value of $b = 4.73$. Upon inputting the relevant impact plate parameters, the impactor was chosen such that the period of its first bending mode was not on the same order of the impact timescale (on the order of 1 ms for the displacement wave to hit the bottom of the sample after impact, using Set A parameters from Table 2.1, or shown later experimentally in Fig. 9.6). The aluminum flyer-plate design had a first mode vibrational period of 49 ms which was much much shorter than the studied impact timescale, and thus not conflicting.

Figure 9.2 shows the impact tower with a focus on the flyer-plate. Figure 9.2(a) shows a side view of the flyer-plate impactor, with the spring loaded polycarbonate plunger plate shown next to the blue arrow. Locking collars (used as stoppers) were placed on the guide rods to stop the plunger a short distance from impacting the sample; the stopper is shown with the red arrow. Figure 9.2(b) shows a "straight on" view of the sample with the plunger plate cocked and impactor mass (boxed in blue and green) "loaded" to the plunger plate using the adhesive. The aluminum flyer-plate projectile was sent into free flight towards the sample after the plunger was stopped by the locking collars. Figure 9.2(c) shows the impactor (boxed in blue and green) as it first strikes the sample.

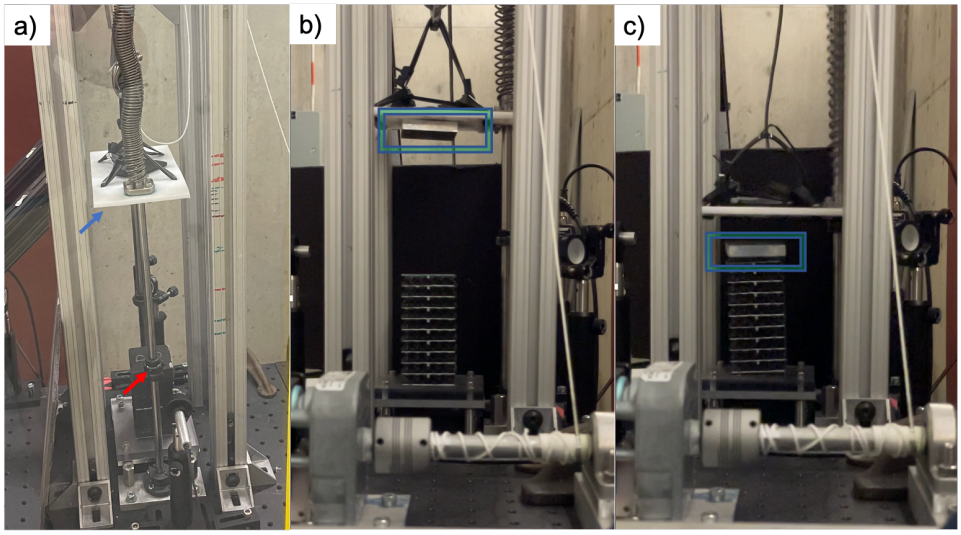

Figure 9.2: a) Side view of the flyer-plate impactor, with the spring loaded polycarbonate plunger plate shown next to the blue arrow, and the plunger plate stopper shown with the red arrow. b) Straight on view of the sample with the plunger plate boxed in blue and green. c) Impactor (boxed in blue and green) as it first strikes the sample.

9.2 Manufactured bistable and control samples for impact testing

Samples were manufactured for dynamic testing. While better performance was predicted with smaller unit cell sizing, due to available printing resource resolution limitations (and the dual material design), samples of $N = 10$ layers were produced. As discussed in Sec. 2.2, a dual material design (Tango Black Plus and Veroclear) was used for the bistable lattice. The lattice relative density (total mass/outer volume) was 477 kg/m^3, and the lattice linear sound speed was 13.7 m/s. The corresponding parameters for the curve fit of a single beam from this lattice are "set A" from Table 2.1.

Three additional sample types were compared against the bistable lattice: a "gum foam" sample (composed of glued and stacked layers of the foam), a "T_{2T}" sample, and a "T_{3T}" sample. Figure 9.3 shows these three samples, in addition to the bistable sample. The T_{2T} and T_{3T} samples were made of the same material combination (TangoBlack Plus and Veroclear) and were designed to have near iden-

tical lattice relative densities as the bistable sample, without exhibiting bistable effects (thus acting as a "control" against which to differentiate the contribution of bistability to impact absorption). Thus the beam portion of the unit cell was doubled (for T_{2T}), or tripled (for T_{3T}) in thickness, then small rectangular cutouts from the monolithic portion were made to offset the additional beam mass. The density from the measured mass of the tested samples were: 476.4 kg/m^3 for T_{2T}, and 489.8 kg/m^3 for T_{3T}. The gum foam sample was selected based on its closely matching density of 480 kg/m^3. Silver paint was marked on at the layer points of all of the sample in order to track layers during DIC.

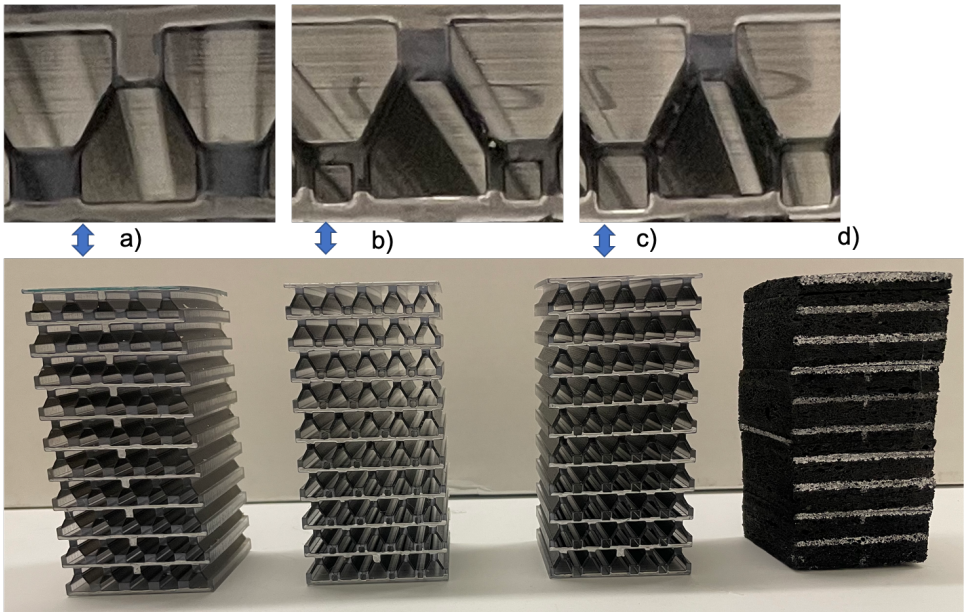

Figure 9.3: a) Full $N = 10$ dual material bistable lattice on the bottom, then an enlargement showing a single unit cell on the top. b) The T_{2T} lattice. c) The T_{3T} lattice. d) Gum foam sample. Silver paint was marked at the 1$[cm]$ point on each of the samples for DIC tracking of layers.

9.3 Image processing methodology for impact testing

A DIC algorithm was developed in order to track the displacement of the layers of the sample after experimental impact, in order to subsequently determine the velocity of the layers and kinetic energy transmission. High intensity white light was used to front light the samples, then color or grayscale video of the desired impacts was captured and downloaded. The sample layers were marked with silver paint in order to track them more easily. The videos were split up into individual images, then converted to binary. The algorithm tracked the lightest part of the imagery, which corresponded to the layers within the material. Based on the information from the first frame, the spatial resolution, and set tolerance values, the at-rest position of the remaining material layers were identified. After each layer position was identified, a tolerance value which applied above and below the layer was set, which restricted the identification of the layer within these boundaries in order to prevent spurious jumping of the layers as a result of image artifacts. The layer tracking and tolerance gates are shown in Fig. 9.4(c) with green denoting layer identification and red marking the tolerance gates, respectively.

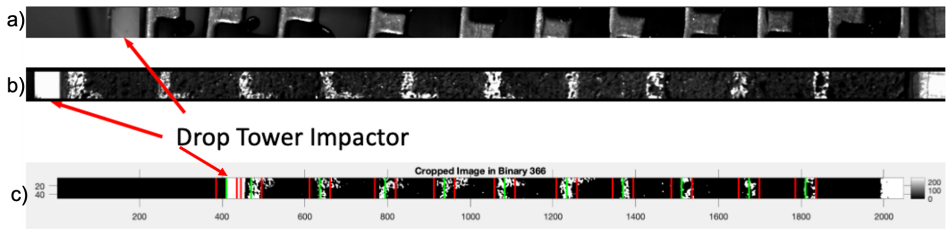

Figure 9.4: a) Impactor hitting the bistable material. b) Impactor impacting the comparative foam material. c) One image from the DIC code. The green lines track the "most white" part of the sample within the gated range defined by the red gates in order to track the layer displacement in the sample. Only a small sample width is captured in the imagery due to camera resolution limits at high frame rate.

The frame of impact is determined when the width of the impactor reaches a threshold distance from the top layer of the sample. After impact, for subsequent

layers, the distance between the location of that layer at the current frame, and that from the previous frame is tracked, in order to determine the pixels, and eventually spatial distance, traveled by each layer. The displacement and time information (based on the camera acquisition frame rate) for all of these layers is then used to get velocity information, which is subsequently used in a similar manner as the displacement and velocity information from ODE45 in simulation in order to get the post-processed results, resulting in a complete spatiotemporal diagram, similar to those from simulation.

9.4 Experimental results and limited comparison with simulation

Figure 9.5 shows the results of experimental impact. Samples were struck from the top by an aluminum flyer-plate, and in Fig. 9.5(a), KE at the half sample point was measured. In Fig. 9.5(b), the KE ratio (comparative material/bistable) was shown for each of the three comparison materials. For instance, the data with the legend marked T_{2T} in Fig. 9.5(b) shows the KE ratio of the T_{2T} sample in comparison with the bistable sample at the same impactor mass and similar impactor velocity (i.e the bistable impact velocity was shown at the marker points. Of note, the bistable velocity was up to 1 m/s higher but never less than the impact velocity into the comparative material.). Impactor M_0 and V_0 were 3.6 m/s and 18 g, respectively. Impactor mass was: $M = 64$g ($M/M_0 = 10^{0.55}$), which was limited by the smallest impactor produced by the author at the time of experimentation. Twelve impacts were shown (three each for the bistable, T_{2T}, T_{3T}, and foam). The lowest tested velocity was $V/V_0 = 10^{0.25}$ and highest was $V/V_0 = 10^{0.65}$. The bistable sample outperformed the foam sample in all tested cases (KE ratio of: 3.8x, 5.7x and 6.7x better, listed in order from high to low V). The KE ratio using the T_{2T} sample for comparison was 0.67*x, 1.89x and 2.61x. Of note, for the 0.67x ratio, the bistable sample was impacted at higher velocity than the T_{2T} sample (7 m/s vs 6 m/s for T_{2T}), thus the initial energy imparted was less in the T_{2T} sample (input energy linear/input energy bistable ≈ 0.73), meaning this

ratio, when adjusted was approximately one. Thus the bistable sample performed similarly or better than the T_{2T} sample. The KE ratios using the T_{3T} samples for comparison were 0.29x, 1.92x and 2.48x. Thus, the bistable sample under performed at the lowest tested impact velocity, although performed well for the higher two comparisons. Given the high damping of the Tango Black Plus material used for the beams of the bistable material, low $N = 10$ layer value, and high M, the bistable sample performed well, as indicated by superior performance in ten of twelve comparisons, and only substantially worse performance in one.

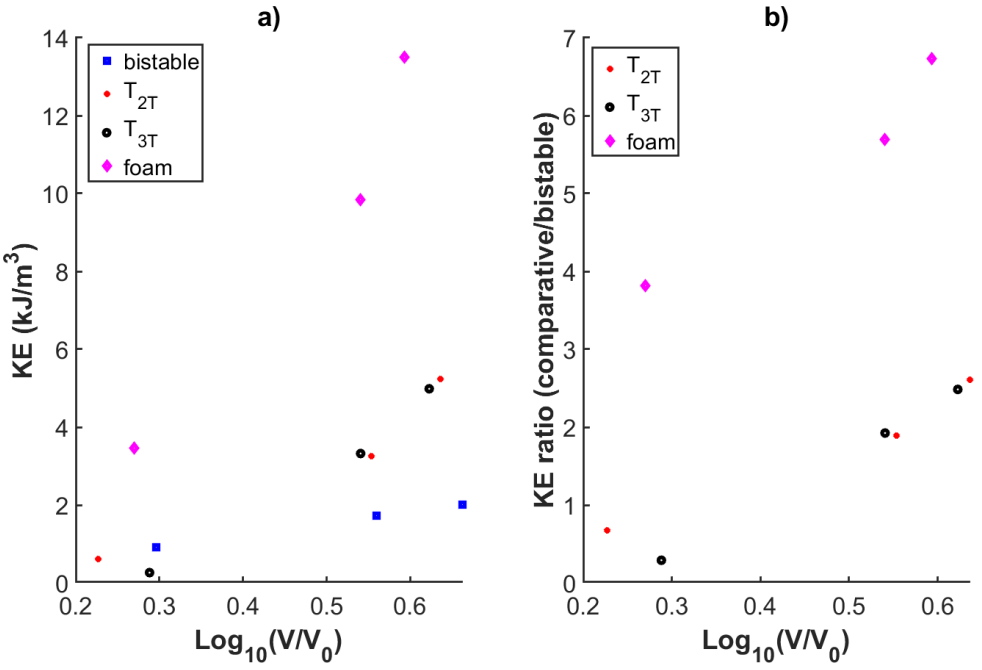

Figure 9.5: a) The KE density transmission. b) The KE ratios. Legend: Bistable sample (blue, a) only), T_{2T} (red), T_{3T} (black), foam (pink).

Fig. 9.6 shows an example XT diagram from the experimental results after completing DIC.

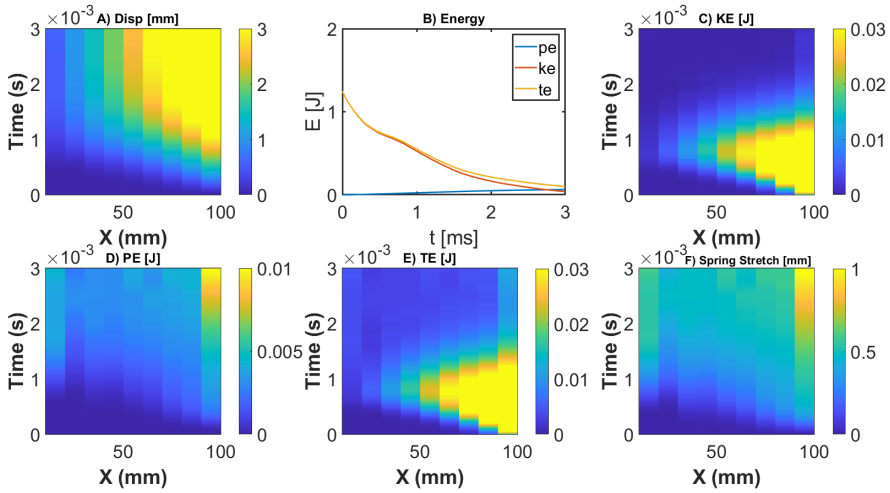

Figure 9.6: Different metrics are shown in terms of: (A) particle displacement, (C) kinetic energy density, (D) potential energy density, (E) total energy density, and (F) spring stretch. (B) shows kinetic, potential, and total energy density over the whole lattice.

Figure. 9.7 shows an example XT diagram from simulation attempting to match the experimental diagram in Fig. 9.6. The matching effort was focused on the initial wavefront, and not the additional rebounds or bounces shown in the KE and TE portions of the diagram. An η value of 370 Ns/m was chosen and $C_1 = -586.55$ (as noted in Sec. 2.6), was set. The η value was chosen by following the methodology described in Chapter 6. The possible η values from the three experimental impacts shown in Fig.9.5(a) were averaged, resulting in a high value (370 Ns/m), and a low value (7.8 Ns/m). The low value was subsequently eliminated after inputting both η values back into simulation, then comparing the resulting cumulative total energy loss (TE at 2 ms)/(TE at 0ms) between the candidate η values. The value $\eta = 370$ Ns/m, resulted in a ratio of 0.16, which was close to the experimental ratio of 0.18, thus 370 was chosen. Use of DMA was also a method attempted to verify these results, although the maximum tested frequency of DMA data for Tango Black plus was well below the "dominant frequency" estimate of impact, and thus it was not used for the analysis.

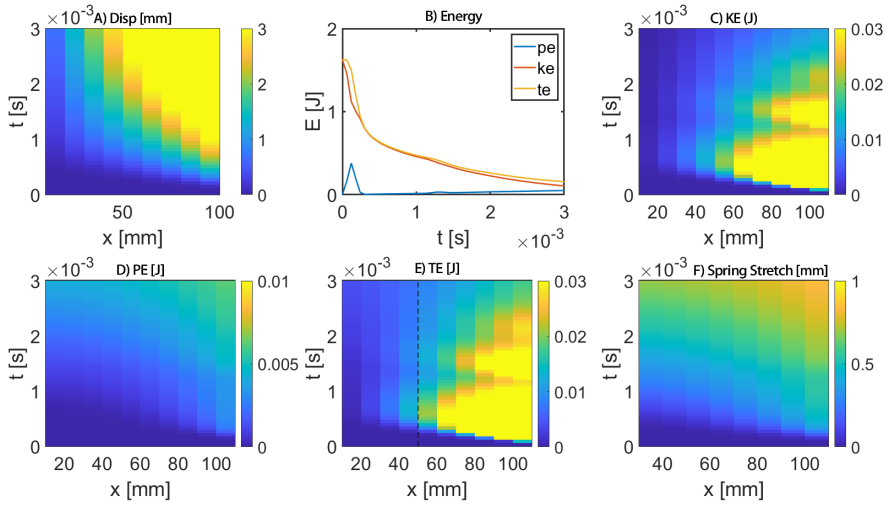

Figure 9.7: Different metrics are shown in terms of: (A) particle displacement, (C) kinetic energy density, (D) potential energy density, (E) total energy density, and (F) spring stretch. (B) shows kinetic, potential, and total energy density over the whole lattice.

As indicated by the estimated η of 370 Ns/m ($D_R \approx 25$) from the impact shown in Fig 9.6, in comparison with the "optimum" value of 3.34 Ns/m ($D_R = 0.66$) from

Sec. 6.5 indicates the experimental sample has far higher damping than optimum, which limits its performance benefits.

Chapter 10

Ideas for future single material bistable lattices iterations

10.1 40 vs 60 Degree Case

As discussed in Sec. 2.3, an option to prevent unwanted bending of the monolithic portion of the unit cell was a dual material design. However, the dual material design complicated sample manufacturing techniques and generally resulted in higher minimum feature size, as well as less unit cells for a given sample size (in comparison to a single material lattice). Another option, as mentioned in Sec. 10, was the reduction of the beam angle θ from 60 degrees to a lower value, which resulted in lower linear stiffness of the beam, which in turn relaxed the stiffness requirement for the monolithic portion of the unit cell. However, this reduces the amount of energy that can be trapped under quasi-static compression. Preliminary quasi-static experimental test using a single material lattice with a $theta = 40$ degree beam angle showed a bistable force versus displacement curve was still possible with a lower θ value than 60 degrees. As such, this section details the results of a limited comparative analysis between the simulated dynamic performance of a 60 degree and a 40 degree beam design in order to see if KE ratio benefits are still observed during impacts of varying V and M.

COMSOL FEM simulations (settings as per Sec. 2.2) were re-run in order

to yield a force versus displacement curve for a beam with $\theta = 40$ degrees, and $\theta = 60$ degrees. The fitting parameters for $\theta = 40$ degrees are from set E and $\theta = 60$ degrees are from set F in Table 2.1. While in Sec. 3.4, an η_s value was picked, in this case, since the $\theta = 40$ degree and $\theta = 60$ degree cases had significantly different linear stiffness values, a similar layer quality factor damping value was used for comparison of results. This calculation resulted in $Q = 145.04$ for $\theta = 60$ degrees, and $Q = 145.07$ for $\theta = 40$ degrees.

The quasi-static elastic energy trapping potential of the two beams followed Sec. 2.4, where the limit of integration was controlled by the chosen end strain value, ε_2. The 40 degree beam would trap 0.0383 J while the 60 degree beam would trap 0.0879 J by quasi-static calculations. Of note, as a simplification, the $\theta = 40$ degree case retained the same unit cell geometry and mass as the $\theta = 60$ degree case.

Figure 10.1 shows the results for the sweep using the $\theta = 40$ degree beam. The sweep was plus and minus one order of magnitude from nominal impactor mass and plus and minus one-half order of magnitude from nominal impactor velocity for the $N = 100$ layers, simulation duration 0.058s ($T_s \approx 4.5$), $Q = 145.07$ sweep. The maximum KE ratio of 19.92x occurred at impactor conditions: $M/M_0 = 10^{0.25}$ and V_0.

Figure 10.2 shows the results for the sweep using the $\theta = 60$ degree beam. The sweep was plus and minus one order of magnitude from nominal impactor mass and plus and minus one-half order of magnitude from nominal impactor velocity for the $N = 100$ layers, simulation duration 0.058s ($T_s \approx 4.5$), $Q = 145.04$ sweep. The maximum KE ratio of 18.62x occurred at impactor conditions: $M/M_0 = 10^{-0.125}$ and V_0.

The best performing case from the sweep using a kinetic energy ratio comparison between Fig. 10.1 and Fig. 10.2, for a value of 19.92x actually occurred as a result of the $\theta = 40$ degree geometry, despite the lower quasi static energy trapping predictions. However, despite the higher maximum value occurring in the 40 degree sweep case, the 60 degree case's maximum value was close (18.62x), and the $\theta = 60$ geometry had a higher number of ratios above 10x, as indicated

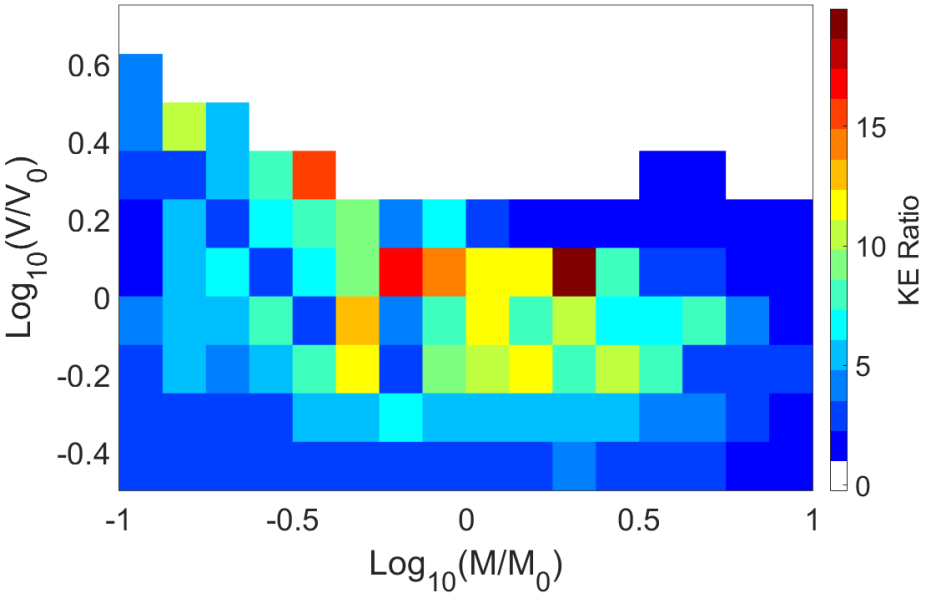

Figure 10.1: KE ratio performance sweep for $\theta = 40$ degree beam. The maximum KE ratio of 19.92x occurred at impact conditions: $M/M_0 = 10^{0.25}$ and V_0. Of note, performance ratio values less than one are shown in this plot.

by a comparison of Fig. 10.1 with Fig. 10.2 (note the colorbar in Fig. 10.2 is adjusted for comparison.) For a brief comparison, the XT diagrams for the impactor conditions which resulted in the best performance in the $\theta = 60$ degree case were shown.

The $\theta = 60$ degree geometry is shown in Fig. 10.3. Impact conditions were: $M/M_0 = 10^{-0.125}$ and V_0, $Q = 145.04$, and KE ratio was 18.62x. Figure 10.3(a,c) show the bistable KE and spring stretch, respectively, and panel b) and D shows the same information for the linear sample.

The $\theta = 40$ degree geometry is shown in Fig. 10.4. Impact conditions were: $M/M_0 = 10^{-0.125}$ and V_0, $Q = 145.07$, and KE ratio was 14.49x. Figure 10.4(a,c) show the bistable KE and spring stretch, respectively, and panel b) and d) shows the same information for the linear sample.

A comparison between Fig. 10.3 and Fig. 10.4 reveals the following. In Fig. 10.3(a), the first solitary wave emission transitions to the "oscillatory" phase sooner ($\approx$ 5ms) than the first solitary wave emission in Fig. 10.4(b) ($\approx$ 9 ms). Addition-

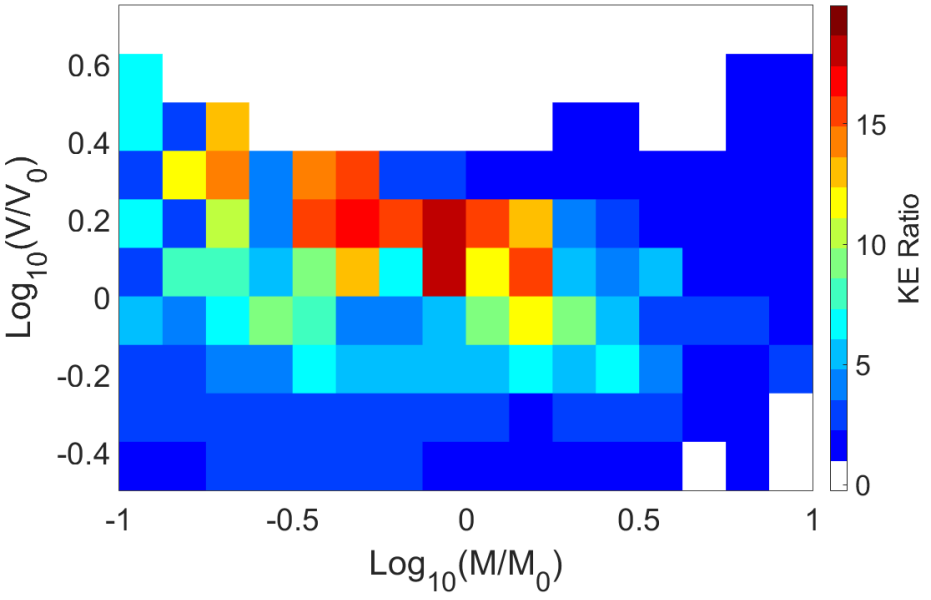

Figure 10.2: Of note, performance ratio values < 1 are shown in this plot. The colorbar was adjusted from the default setting (Min = 0.16, Max = 18.6) to match the default colorbar settings in Fig.10.1 (Min = 0.14, Max = 19.92) for purposes of comparison.

ally, Fig. 10.3(c) shows more permanent spring stretch (permanent bounded within the timeframe shown), as indicated by ≈ 10 layers showing ≈ 5 mm or more for the 0.02s time duration shown in the plot. For comparison, Fig 10.4(c) shows $2-3$ layers where $\approx$ 5mm of spring stretch is achieved for the same duration. Despite these differences, both samples, as indicated by their ratio values of 14.49x and 18.62x, perform well. The qualitative physics (i.e. multiple solitary waves followed by oscillatory region, and regions of "permanent" spring stretch) of both compared cases also appear similar.

Additionally, it is noteworthy that while the quasi-static estimate predicts far better performance (2.3x) from the $\theta = 60$ degree geometry in comparison to the $\theta = 40$ degree geometry, the performance difference in the dynamic comparison is less clear. In many cases the $\theta = 40$ degree beam outperforms the $\theta = 60$ geometry in dynamic simulation, and the $\theta = 40$ geometry has the highest KE ratio in the simulated sweep. Thus, it appears from these results that altering geometry to a lower beam angle (which is supportive of a single material design) is a viable

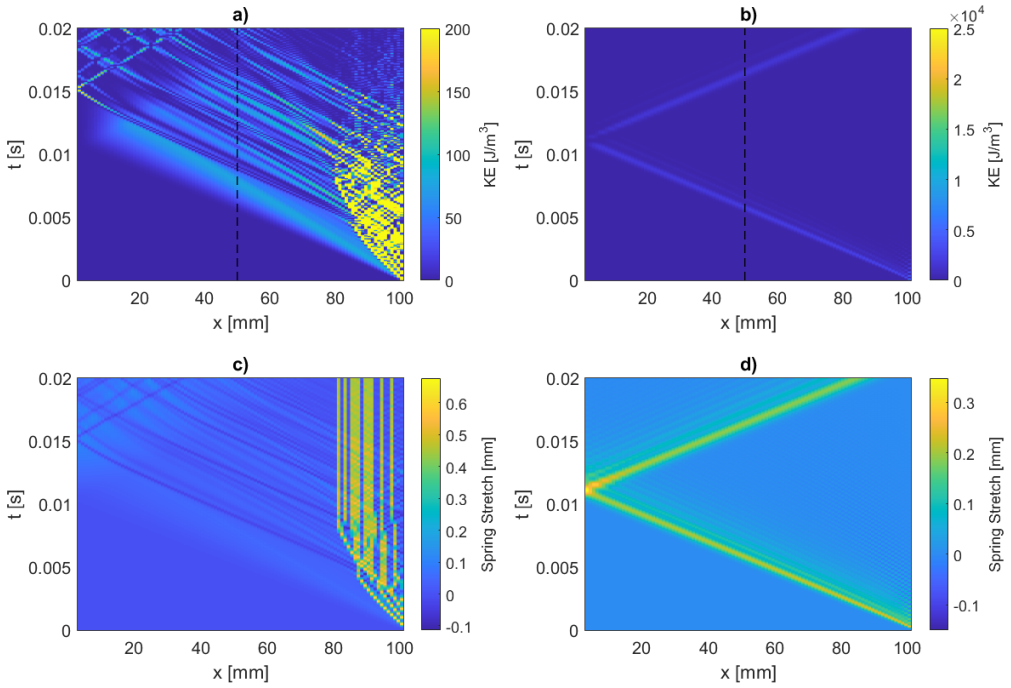

Figure 10.3: The KE performance ratio (linear/bistable) is $18.62x$. Note the colorbar maximum in a) was reduced to show interactions immediately after impact more clearly.

method to pursue further towards the aim of producing bistable unit cells from a single material lattice.

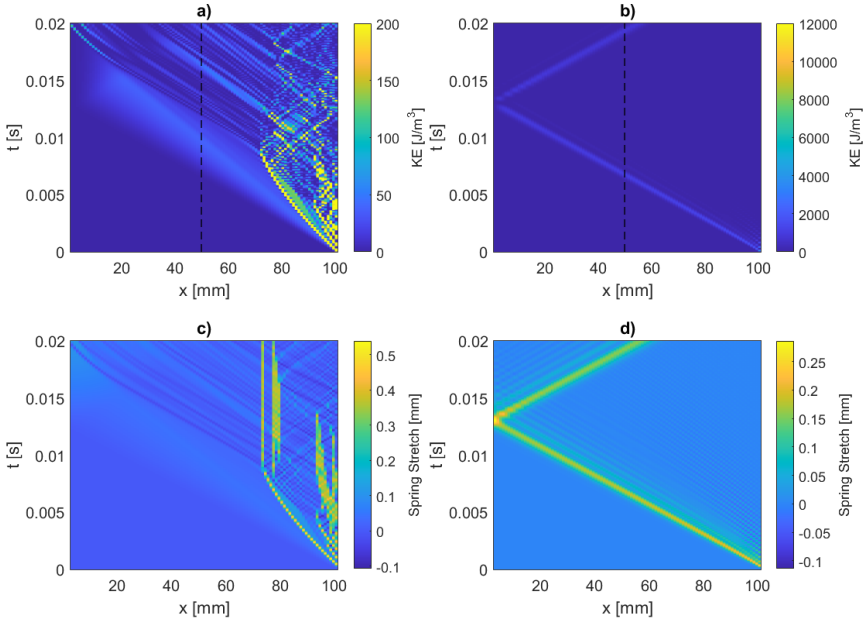

Figure 10.4: The KE performance ratio (linear/bistable) is $14.49x$. Note the colorbar maximum in a) was reduced to show interactions immediately after impact more clearly.

10.2 Beam depth ratio reduction and impactor velocity scaling

Another potential method to achieve bistable affects with a single material lattice with minimal change to the initial design was to reduce the depth of the spring portion for the same lattice depth, thus reducing the stiffness of the spring without changing the beam angle, as shown in Fig. 10.5.

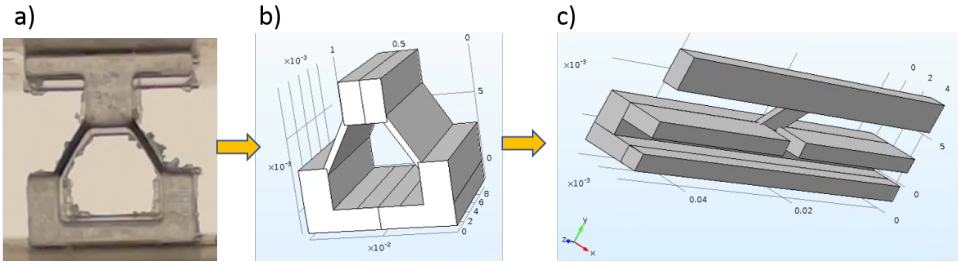

Figure 10.5: a) Printed unit cell of the current design. b) A CAD representation of this same design, with the view adjusted to show the beam is extruded into the depth. c) Modified cell design, where the beam portion is reduced from the original size to approximately $\frac{1}{20}th$ in order to reduce stiffness (in this example $Z = 20$). A "middle support" in c) is also shown, although not accounted for in the analysis.

Figure 10.5(a) shows a picture of one unit cell, then Figure 10.5(b) shows a CAD rendering of the same unit cell, allowing the reader to see the buckling "non-monolithic" portion of the beam going through the entire depth of the unit cell. While maximizing the depth of the buckling portion of the beam maximized the simulated quasi-static strain energy trapping of the beam for the given unit cell design, it also required the monolithic portion to be made of a stiffer material, as previously discussed. Figure 10.5(c) shows another alternative: completed by modifying the unit cell design such that the buckling portion of the beam was reduced "into the depth" of the material, as shown. This resulted in a lower beam stiffness value, and allowed for desired beam buckling to happen, while minimizing unwanted bending within the monolithic portion. Note the addition of a "stiffening" horizontal member in Fig. 10.5(c), which is not accounted for in this analysis.

Section 10 noted (through FEM) a minimum "modulus ratio" of 5.8x (monolithic/beam) for the unit cell geometry (per Sec. 2.5 with $\theta = 60$). The author

notes here that reducing the depth of the beam to 5.8x its original depth (while keeping the depth of the monolithic portion the same) would have the same effect. This presents another production option to achieve bistability from a single-material unit cell, although it is worthwhile to note that this method presents additional challenges, particularly in terms of printing a small scale 3D structure with feature differences into the depth. This is left for future work.

Should this method be chosen for future work, it is important to understand the effects on the predicted nominal impactor mass and velocity conditions. Thus, the previous scaling relations from Sec. 2.7 and Sec. 2.8 were expanded upon in order to understand the changes to V_0 and M_0, given a unit cell design where the beams were altered into the depth. For this example, we'll assume the new beam depth is reduced to $1/Z$ of the original, achieving the noted 5.8x minimum "modulus ratio", and an ample pad. Equation 2.7 from Sec. 2.4 describes the stress, thus understanding this equation to scale linearly as a result of changing to $1/Z$th of the original beam depth results in:

$$\sigma = \frac{2}{Zd}(\beta_3 H_C^2 \varepsilon^3 + \beta_2 H_C \varepsilon^2 + \beta_1 \varepsilon), \tag{10.1}$$

describing stress in the unit cell for the adjusted depth. The resulting linear stiffness value, used to estimate the long wavelength linear sound speed of the material, is described by:

$$k_L = \frac{2N}{Z}\beta_1. \tag{10.2}$$

Assuming that the monolithic portion of the unit cell is much, much larger than the beam portion, there is negligible change to the unit cell (or layer mass), thus it remains $m_L = \rho a d^2$. Wavespeed is now calculated, where C_0 represents the wavespeed of the full depth unit cell and C_{RD} represents the wavespeed of the reduced depth cell:

$$C_{RD} = \sqrt{\frac{1}{Z}} C_0. \tag{10.3}$$

Referencing Eq. 10.4 for dynamic strain [3], the new estimated nominal impactor velocity (V_{0RD}) for a sample made of reduced depth unit cells scales in accordance

with:

$$V_{0RD} = \sqrt{\frac{1}{Z}} V_0. \tag{10.4}$$

Thus by reducing the depth of the beam portion of the unit cell by Z, V_0 scales by $\sqrt{\frac{1}{Z}}$ and there is no change to M_0.

Chapter 11

Conclusions and recommendations for future work

This manuscript is the result of the author's search for answers, primarily regarding a better understanding of if/how performance of a particular bistable mechanical metamaterial changed with respect to changing impactor conditions. As a consequence of this search, several conclusions have been attained, and several avenues for continued work have been identified. The following describes the most salient points.

11.1 Conclusions

The performance of the simulated and tested bistable mechanical metamaterial is in fact highly dependent on the impactor conditions (mass and velocity). This assertion is well supported throughout the manuscript, but as one particularly stark example of the performance differences, in Sec. 5, the performance of a $N = 200$ sample ranged from worse (0.86x) to far superior (204x) in comparison to the control lattice, with the only changing variables being the velocity and the mass of the impactor striking the sample. Two significant implications of this finding are; the bistable mechanism has the potential to yield significant performance benefits in terms of KE abatement if the material and impact conditions are well paired, but if not well paired, the bistable material will likely underperform a more

traditional material, sometimes by a substantial margin.

For a finite sample size, decreasing unit cell (or layer) size tends to increase performance, particularly within the range of 50 to 200 layers in the tested sample. It appears based on the author's research that performance plateaus after a certain minimum layer size (around 250), although testing beyond 300 layers, or in broad ranging η values was not completed to confirm this.

In the 10 layer case, the most rigorously tested in terms of the effect of damping on maximum performance, there is a clear optimum η for maximum KE ratio performance, and performance declines sharply with either an increase or decrease of this value from the optimum. The "optimum" damping needs to be low enough that some (or many) of the top layers of the lattice are not inhibited from snapping to their secondary stable state, but high enough to prevent layers from "snapping back", and re-releasing energy. An essential point is that while increasing damping, by definition, results in additional energy taken away from a system, past the optimum value in this system, more damping spoils the bistable energy trapping, thus resulting in worse performance than a lattice made of a less damped (i.e. lower η) material system. The optimum performance from simulation occurred at $D_R = 0.66$. Values much greater or less than 0.66 resulted in suboptimal performance.

Adaptation of Katz and Givli's [107] piecewise representation of a softer post-buckled spring design into a continuous polynomial force versus displacement function for simulation resulted in up to over 2x improvement in maximum KE ratio performance over the same impactor conditions. This statement is in comparison to a lattice exhibiting a bistable force versus displacement response where the post-buckled stiffness was higher than the pre-buckled. It is important to note however that design of a physical unit cell exhibiting softer post-bucked stiffness was not attempted. Additionally, the softened post-buckled design does not match well with increasing stiffness as a result of self contact, which may greatly limit the utility of this design.

11.2 Recommendations for future work

Production and subsequent testing of samples with layers greater than 10 should be completed in order to validate "higher N" simulations which showed significant maximum performance benefit to increased unit cells (within a finite sample size). Since a limitation to production at smaller scale was the necessity of a dual material design for the chosen geometry, consideration should be given to production of a unit cell design that allows bistability utilizing only a single material. Two possible approaches included in the text were; the reduction in beam angle θ, and the reduction of the ratio of the beam depth relative to the sample depth. However, as freely noted by the author, the focus of this work was primarily better understanding the changes in performance of a somewhat arbitrarily chosen baseline design, thus leaving much room for future optimization of the unit cell design itself, in terms of both KE ratio performance, but also mass density.

Adequately calculating and assessing damping was, and continues to be a challenge. While the 10 layer case was tested rigorously and showed a clear "optimum" damping value, the optimum damping value appeared to change with changing layers. This is likely a result of a lower η_s being required to maintain the same D_R when N is increased, but this should be verified in order to further investigate "optimums" in higher layer cases for a finite sample size. Additionally, since the damping analysis done to date indicated the utilized material for experimental samples was over-damped, new samples of lower material damping should be produced and tested.

Bibliography

[1] W. Schiehlen, "The long history of impact mechanics, rolling contact and multibody system dynamics," *PAMM*, vol. 17, no. 1, pp. 165–166, 2017.

[2] Y. Li, H. Fan, and X.-L. Gao, "Ballistic helmets: Recent advances in materials, protection mechanisms, performance, and head injury mitigation," *Composites Part B: Engineering*, p. 109890, 2022.

[3] M. A. Meyers, *Dynamic behavior of materials*. John wiley & sons, 1994.

[4] C. M. Harris and A. G. Piersol, *Harris' shock and vibration handbook*, vol. 5. McGraw-Hill New York, 2002.

[5] J. M. Gere, "Mechanics of materials. thomson learning," *Inc*, p. 964, 2004.

[6] R. Hibbeler and K. Vijay, "Mechanics of materials, worldwide adaptation edition, si edition," 2014.

[7] F. Beer, E. Johnston, J. DeWolf, and D. Mazurek, "Mechanics of materials. 7th_edition," *New York. MeGraw-Hill Education Ltd*, 2015.

[8] V. Nesterenko, *Dynamics of heterogeneous materials*. Springer Science & Business Media, 2013.

[9] C. A. Brebbia, G. Nurick, and A. Bogdanovich, "Advances in dynamics and impact mechanics," *Appl. Mech. Rev.*, vol. 56, no. 6, pp. B78–B79, 2003.

[10] B. Ralph, "Vibration and impact," *Addison-Kegley Publishig i˜ y, Inc*, vol. 158, p. 166, 1968.

[11] B. BROGLIATO, "Nonsmooth impact mechanics: Models, dynamics and control," *Lecture Notes in Control and Information Science*, vol. 210, 1996.

[12] K. L. Johnson and K. L. Johnson, *Contact mechanics*. Cambridge university press, 1987.

[13] G. M. L. Gladwell, *Contact problems in the classical theory of elasticity*. Springer Science & Business Media, 1980.

[14] H. Hertz, *The principles of mechanics presented in a new form*. Macmillian and Company, Limited, 1899.

[15] I. Y. Shtaerman, "Contact problem of the theory of elasticity," tech. rep., FOREIGN TECHNOLOGY DIV WRIGHT-PATTERSON AFB OH, 1970.

[16] B. Paul and J. Hashemi, "Contact pressures on closely conforming elastic bodies," 1981.

[17] K. P. Singh and B. Paul, "Numerical solution of non-hertzian elastic contact problems," 1974.

[18] W. Woodward and B. Paul, "Contact stresses for closely conforming bodies–application to cylinders and spheres," tech. rep., United States. Dept. of Transportation, 1976.

[19] S. Shan, S. H. Kang, J. R. Raney, P. Wang, L. Fang, F. Candido, J. A. Lewis, and K. Bertoldi, "Multistable architected materials for trapping elastic strain energy," *Advanced Materials*, vol. 27, no. 29, pp. 4296–4301, 2015.

[20] X. Q. Wang, "The failure analysis and the innovative design of hammer head on hammer crusher based on triz theory," in *Applied Mechanics and Materials*, vol. 741, pp. 85–90, Trans Tech Publ, 2015.

[21] L. Wu, X. Xi, B. Li, and J. Zhou, "Multi-stable mechanical structural materials," *Advanced Engineering Materials*, vol. 20, no. 2, p. 1700599, 2018.

[22] J. A. Sherwood and C. C. Frost, "Constitutive modeling and simulation of energy absorbing polyurethane foam under impact loading," *Polymer Engineering & Science*, vol. 32, no. 16, pp. 1138–1146, 1992.

[23] V. I. Babitsky, *Theory of vibro-impact systems and applications*. Springer Science & Business Media, 2013.

[24] W. J. Stronge, *Impact mechanics*. Cambridge university press, 2018.

[25] M. Langseth, O. Hopperstad, and T. Berstad, "Crashworthiness of aluminium extrusions: validation of numerical simulation, effect of mass ratio and impact velocity," *International Journal of Impact Engineering*, vol. 22, no. 9-10, pp. 829–854, 1999.

[26] W. Johnson and A. G. Mamalis, "Crashworthiness of vehicles," tech. rep., 1978.

[27] B. Cerup-Simonsen, W. Abramowicz, and C. Høstgaard-Brene, "Crushing strength of ship structures," in *Vehicle Infrastructure Interaction Conference VI*, 1999.

[28] B. Brogliato, *Impacts in mechanical systems: analysis and modelling*, vol. 551. Springer Science & Business Media, 2000.

[29] J. Reid, "Towards the understanding of material property influence on automotive crash structures," *Thin-walled structures*, vol. 24, no. 4, pp. 285–313, 1996.

[30] N. R. Council, *Opportunities in protection materials science and technology for future army applications*. National Academies Press, 2011.

[31] E. Schneider and A. Stilp, "Micrometeorite impact simulation at emi—a review," *International Journal of Impact Engineering*, vol. 5, no. 1-4, pp. 561–568, 1987.

[32] J. Pabari and P. Bhalodi, "Estimation of micrometeorites and satellite dust flux surrounding mars in the light of maven results," *Icarus*, vol. 288, pp. 1–9, 2017.

[33] R. Destefanis, "Analysis methodologies for assessing micro-meteoroids and orbital debris risk to spacecraft," *Proceedings of the Institution of Mechanical Engineers, Part G: Journal of Aerospace Engineering*, vol. 221, no. 6, pp. 963–968, 2007.

[34] J. L. Hyde, E. L. Christiansen, and D. M. Lear, "Observations of mmod impact damage to the iss," in *International Orbital Debris Conference*, no. JSC-E-DAA-TN75127, 2019.

[35] T. Cesari, "Webb: Engineered to endure micrometeoroid impacts," Jun 2022.

[36] M. Bartels, "Did a micrometeoroid poke a hole in the space station?," Aug 2018.

[37] R. Lakes and R. S. Lakes, *Viscoelastic materials*. Cambridge university press, 2009.

[38] C. R. Siviour and J. L. Jordan, "High strain rate mechanics of polymers: a review," *Journal of Dynamic Behavior of Materials*, vol. 2, no. 1, pp. 15–32, 2016.

[39] T. Tsuda, H. Hayashi, T. Yamamoto, A. Abe, and S. Tanimura, "Dynamic tensile properties of engineering plastics over a wide range of strain rates," *Journal of Solid Mechanics and Materials Engineering*, vol. 6, no. 6, pp. 711–720, 2012.

[40] M. Dawson, G. McKinley, and L. Gibson, "The dynamic compressive response of open-cell foam impregnated with a newtonian fluid," *Journal of applied mechanics*, vol. 75, no. 4, 2008.

[41] R. Bouferra, H. Pron, J.-F. Henry, C. Bissieux, and J. Beaudoin, "Study of the intrinsic dissipation associated to the plastic work induced by a ball impact," *International journal of thermal sciences*, vol. 44, no. 2, pp. 115–119, 2005.

[42] W. Mason and H. McSkimin, "Energy losses of sound waves in metals due to scattering and diffusion," *Journal of Applied Physics*, vol. 19, no. 10, pp. 940–946, 1948.

[43] A. Lagendijk, B. Van Tiggelen, and D. S. Wiersma, "Fifty years of anderson localization," *Phys. today*, vol. 62, no. 8, pp. 24–29, 2009.

[44] B. P. Lawney and S. Luding, "Frequency filtering in disordered granular chains," *Acta mechanica*, vol. 225, no. 8, pp. 2385–2407, 2014.

[45] S. Rotter and S. Gigan, "Light fields in complex media: Mesoscopic scattering meets wave control," *Reviews of Modern Physics*, vol. 89, no. 1, p. 015005, 2017.

[46] L. Papadopoulos, M. A. Porter, K. E. Daniels, and D. S. Bassett, "Network analysis of particles and grains," *Journal of Complex Networks*, vol. 6, no. 4, pp. 485–565, 2018.

[47] S. Hughes, L. Ramunno, J. F. Young, and J. Sipe, "Extrinsic optical scattering loss in photonic crystal waveguides: role of fabrication disorder and photon group velocity," *Physical review letters*, vol. 94, no. 3, p. 033903, 2005.

[48] S. Wen, Y. Xiong, S. Hao, F. Li, and C. Zhang, "Enhanced band-gap properties of an acoustic metamaterial beam with periodically variable cross-sections," *International Journal of Mechanical Sciences*, vol. 166, p. 105229, 2020.

[49] M. Moscatelli, R. Ardito, L. Driemeier, and C. Comi, "Band-gap structure in two-and three-dimensional cellular locally resonant materials," *Journal of Sound and Vibration*, vol. 454, pp. 73–84, 2019.

[50] V. Fokin, M. Ambati, C. Sun, and X. Zhang, "Method for retrieving effective properties of locally resonant acoustic metamaterials," *Physical review B*, vol. 76, no. 14, p. 144302, 2007.

[51] F. Payne and J. Lacey, "A theoretical analysis of scattering loss from planar optical waveguides," *Optical and Quantum Electronics*, vol. 26, no. 10, pp. 977–986, 1994.

[52] T. Frenzel, C. Findeisen, M. Kadic, P. Gumbsch, and M. Wegener, "Tailored buckling microlattices as reusable light-weight shock absorbers," *Advanced Materials*, vol. 28, no. 28, pp. 5865–5870, 2016.

[53] L. Di Landro, G. Sala, and D. Olivieri, "Deformation mechanisms and energy absorption of polystyrene foams for protective helmets," *Polymer testing*, vol. 21, no. 2, pp. 217–228, 2002.

[54] A. Sondén, D. Rocksén, L. Riddez, J. Davidsson, J. K. Persson, D. Gryth, J. Bursell, and U. P. Arborelius, "Trauma attenuating backing improves protection against behind armor blunt trauma," *Journal of Trauma and Acute Care Surgery*, vol. 67, no. 6, pp. 1191–1199, 2009.

[55] M. Avalle, G. Belingardi, and R. Montanini, "Characterization of polymeric structural foams under compressive impact loading by means of energy-absorption diagram," *International journal of impact engineering*, vol. 25, no. 5, pp. 455–472, 2001.

[56] T. A. Schaedler and W. B. Carter, "Architected cellular materials," *Annual Review of Materials Research*, vol. 46, pp. 187–210, 2016.

[57] A. C. Merkle, E. E. Ward, J. V. O'Connor, and J. C. Roberts, "Assessing behind armor blunt trauma (babt) under nij standard-0101.04 conditions using human torso models," *Journal of Trauma and Acute Care Surgery*, vol. 64, no. 6, pp. 1555–1561, 2008.

[58] P. Forquin and J.-L. Zinszner, "A pulse-shaping technique to investigate the behaviour of brittle materials subjected to plate-impact tests," *Philosophical Transactions of the Royal Society A: Mathematical, Physical and Engineering Sciences*, vol. 375, no. 2085, p. 20160333, 2017.

[59] J. Taylor and S. Patek, "Ritualized fighting and biological armor: the impact mechanics of the mantis shrimp's telson," *Journal of Experimental Biology*, vol. 213, no. 20, pp. 3496–3504, 2010.

[60] A. Drake, T. L. H. Donahue, M. Stansloski, K. Fox, B. B. Wheatley, and S. W. Donahue, "Horn and horn core trabecular bone of bighorn sheep rams absorbs impact energy and reduces brain cavity accelerations during high impact ramming of the skull," *Acta biomaterialia*, vol. 44, pp. 41–50, 2016.

[61] P. Qiao, M. Yang, and F. Bobaru, "Impact mechanics and high-energy absorbing materials," *Faculty Publications from the Department of Engineering Mechanics*, p. 62, 2008.

[62] R. F. Gibson, "A review of recent research on mechanics of multifunctional composite materials and structures," *Composite structures*, vol. 92, no. 12, pp. 2793–2810, 2010.

[63] S. Gholizadeh, "A review of non-destructive testing methods of composite materials," *Procedia structural integrity*, vol. 1, pp. 50–57, 2016.

[64] X. Yu, J. Zhou, H. Liang, Z. Jiang, and L. Wu, "Mechanical metamaterials associated with stiffness, rigidity and compressibility: A brief review," *Progress in Materials Science*, vol. 94, pp. 114–173, 2018.

[65] M. Wegener, "Metamaterials beyond optics," *Science*, vol. 342, no. 6161, pp. 939–940, 2013.

[66] M. Kadic, G. W. Milton, M. van Hecke, and M. Wegener, "3d metamaterials," *Nature Reviews Physics*, vol. 1, no. 3, pp. 198–210, 2019.

[67] W. Cai and V. M. Shalaev, *Optical metamaterials*, vol. 10. Springer, 2010.

[68] R. Marqués, F. Martin, and M. Sorolla, *Metamaterials with negative parameters: theory, design, and microwave applications*. John Wiley & Sons, 2011.

[69] R. W. Ziolkowski, "Metamaterials: The early years in the usa," *EPJ Applied Metamaterials*, 2014.

[70] S. Yves, R. Fleury, T. Berthelot, M. Fink, F. Lemoult, and G. Lerosey, "Crystalline metamaterials for topological properties at subwavelength scales," *Nature communications*, vol. 8, no. 1, pp. 1–10, 2017.

[71] S. Yves, G. Lerosey, and F. Lemoult, "Structure-composition correspondence in crystalline metamaterials for acoustic valley-hall effect and unidirectional sound guiding," *EPL (Europhysics Letters)*, vol. 129, no. 4, p. 44001, 2020.

[72] T. J. Cui, D. R. Smith, and R. Liu, *Metamaterials*. Springer, 2010.

[73] M. Maldovan, "Sound and heat revolutions in phononics," *Nature*, vol. 503, no. 7475, pp. 209–217, 2013.

[74] B. Banerjee, *An introduction to metamaterials and waves in composites*. Crc Press, 2011.

[75] F. Dell'Isola, D. Steigmann, and A. Della Corte, "Synthesis of fibrous complex structures: designing microstructure to deliver targeted macroscale response," *Applied Mechanics Reviews*, vol. 67, no. 6, pp. 21–pages, 2016.

[76] J.-H. Lee, J. P. Singer, and E. L. Thomas, "Micro-/nanostructured mechanical metamaterials," *Advanced materials*, vol. 24, no. 36, pp. 4782–4810, 2012.

[77] E. B. Herbold and V. F. Nesterenko, "Propagation of rarefaction pulses in discrete materials with strain-softening behavior," *Physical review letters*, vol. 110, no. 14, p. 144101, 2013.

[78] D. Del Vescovo and I. Giorgio, "Dynamic problems for metamaterials: review of existing models and ideas for further research," *International Journal of Engineering Science*, vol. 80, pp. 153–172, 2014.

[79] E. Barchiesi, M. Spagnuolo, and L. Placidi, "Mechanical metamaterials: a state of the art," *Mathematics and Mechanics of Solids*, vol. 24, no. 1, pp. 212–234, 2019.

[80] J. U. Surjadi, L. Gao, H. Du, X. Li, X. Xiong, N. X. Fang, and Y. Lu, "Mechanical metamaterials and their engineering applications," *Advanced Engineering Materials*, vol. 21, no. 3, p. 1800864, 2019.

[81] J. Li, X. Wen, and P. Sheng, "Acoustic metamaterials," *Journal of Applied Physics*, vol. 129, no. 17, p. 171103, 2021.

[82] Q. Li, Z. He, and E. Li, "Dissipative multi-resonator acoustic metamaterials for impact force mitigation and collision energy absorption," *Acta Mechanica*, vol. 230, no. 8, pp. 2905–2935, 2019.

[83] L. R. Meza, S. Das, and J. R. Greer, "Strong, lightweight, and recoverable three-dimensional ceramic nanolattices," *Science*, vol. 345, no. 6202, pp. 1322–1326, 2014.

[84] T. A. Schaedler, A. J. Jacobsen, A. Torrents, A. E. Sorensen, J. Lian, J. R. Greer, L. Valdevit, and W. B. Carter, "Ultralight metallic microlattices," *Science*, vol. 334, no. 6058, pp. 962–965, 2011.

[85] A. Torrents, T. Schaedler, A. Jacobsen, W. Carter, and L. Valdevit, "Characterization of nickel-based microlattice materials with structural hierarchy from the nanometer to the millimeter scale," *Acta Materialia*, vol. 60, no. 8, pp. 3511–3523, 2012.

[86] G. Lee and B. Hartmann, "Specific damping capacity for arbitrary loss angle," *Journal of sound and vibration*, vol. 211, no. 2, pp. 265–272, 1998.

[87] L. Valdevit, S. W. Godfrey, T. A. Schaedler, A. J. Jacobsen, and W. B. Carter, "Compressive strength of hollow microlattices: Experimental characterization, modeling, and optimal design," *Journal of Materials Research*, vol. 28, no. 17, pp. 2461–2473, 2013.

[88] M. Mieszala, M. Hasegawa, G. Guillonneau, J. Bauer, R. Raghavan, C. Frantz, O. Kraft, S. Mischler, J. Michler, and L. Philippe, "Micromechanics of amorphous metal/polymer hybrid structures with 3d cellular architectures: size effects, buckling behavior, and energy absorption capability," *Small*, vol. 13, no. 8, p. 1602514, 2017.

[89] C. Q. Lai and C. Daraio, "Highly porous microlattices as ultrathin and efficient impact absorbers," *International Journal of Impact Engineering*, vol. 120, pp. 138–149, 2018.

[90] L. R. Meza, A. J. Zelhofer, N. Clarke, A. J. Mateos, D. M. Kochmann, and J. R. Greer, "Resilient 3d hierarchical architected metamaterials," *Proceedings of the National Academy of Sciences*, vol. 112, no. 37, pp. 11502–11507, 2015.

[91] Y. Cao, M. Derakhshani, Y. Fang, G. Huang, and C. Cao, "Bistable structures for advanced functional systems," *Advanced Functional Materials*, vol. 31, no. 45, p. 2106231, 2021.

[92] S. P. Pellegrini, N. Tolou, M. Schenk, and J. L. Herder, "Bistable vibration energy harvesters: a review," *Journal of Intelligent Material Systems and Structures*, vol. 24, no. 11, pp. 1303–1312, 2013.

[93] B. Li, Y.-P. Cao, X.-Q. Feng, and H. Gao, "Mechanics of morphological instabilities and surface wrinkling in soft materials: a review," *Soft Matter*, vol. 8, no. 21, pp. 5728–5745, 2012.

[94] Y. Forterre, J. M. Skotheim, J. Dumais, and L. Mahadevan, "How the venus flytrap snaps," *Nature*, vol. 433, no. 7024, pp. 421–425, 2005.

[95] X. Wang, A. Khara, and C. Chen, "A soft pneumatic bistable reinforced actuator bioinspired by venus flytrap with enhanced grasping capability," *Bioinspiration & Biomimetics*, vol. 15, no. 5, p. 056017, 2020.

[96] S. Timoshenko, "Buckling of flat curved bars and slightly curved plates," 1935.

[97] L. Cedolin, "Stability of structures."

[98] S. Guest and S. Pellegrino, "Analytical models for bistable cylindrical shells," *Proceedings of the Royal Society A: Mathematical, Physical and Engineering Sciences*, vol. 462, no. 2067, pp. 839–854, 2006.

[99] A. Rafsanjani and D. Pasini, "Bistable auxetic mechanical metamaterials inspired by ancient geometric motifs," *Extreme Mechanics Letters*, vol. 9, pp. 291–296, 2016.

[100] A. Pandey, D. E. Moulton, D. Vella, and D. P. Holmes, "Dynamics of snapping beams and jumping poppers," *EPL (Europhysics Letters)*, vol. 105, no. 2, p. 24001, 2014.

[101] A. Fargette, S. Neukirch, and A. Antkowiak, "Elastocapillary snapping: Capillarity induces snap-through instabilities in small elastic beams," *Physical review letters*, vol. 112, no. 13, p. 137802, 2014.

[102] T. Chen, O. R. Bilal, K. Shea, and C. Daraio, "Harnessing bistability for directional propulsion of soft, untethered robots," *Proceedings of the National Academy of Sciences*, vol. 115, no. 22, pp. 5698–5702, 2018.

[103] J. R. Raney, N. Nadkarni, C. Daraio, D. M. Kochmann, J. A. Lewis, and K. Bertoldi, "Stable propagation of mechanical signals in soft media using stored elastic energy," *Proceedings of the National Academy of Sciences*, vol. 113, no. 35, pp. 9722–9727, 2016.

[104] H. Fang, K. Wang, and S. Li, "Asymmetric energy barrier and mechanical diode effect from folding multi-stable stacked-origami," *Extreme Mechanics Letters*, vol. 17, pp. 7–15, 2017.

[105] A. Zembilören, "A study on energy trapping parameters of a multistable elastic beam," Master's thesis, Middle East Technical University, 2018.

[106] C. S. Ha, R. S. Lakes, and M. E. Plesha, "Design, fabrication, and analysis of lattice exhibiting energy absorption via snap-through behavior," *Materials & Design*, vol. 141, pp. 426–437, 2018.

[107] S. Katz and S. Givli, "Solitary waves in a bistable lattice," *Extreme Mechanics Letters*, vol. 22, pp. 106–111, 2018.

[108] S. Katz and S. Givli, "Solitary waves in a nonintegrable chain with double-well potentials," *Physical Review E*, vol. 100, no. 3, p. 032209, 2019.

[109] H. Yasuda, E. G. Charalampidis, P. K. Purohit, P. G. Kevrekidis, and J. R. Raney, "Wave manipulation using a bistable chain with reversible impurities," *Physical Review E*, vol. 104, no. 5, p. 054209, 2021.

[110] J. McCowan, "Vii. on the solitary wave," *The London, Edinburgh, and Dublin Philosophical Magazine and Journal of Science*, vol. 32, no. 194, pp. 45–58, 1891.

[111] T. Dauxois and M. Peyrard, *Physics of solitons*. Cambridge University Press, 2006.

[112] M. Lapine, I. V. Shadrivov, and Y. S. Kivshar, "Colloquium: nonlinear metamaterials," *Reviews of Modern Physics*, vol. 86, no. 3, p. 1093, 2014.

[113] N. J. Zabusky and M. D. Kruskal, "Interaction of" solitons" in a collisionless plasma and the recurrence of initial states," *Physical review letters*, vol. 15, no. 6, p. 240, 1965.

[114] N. Nadkarni, C. Daraio, and D. M. Kochmann, "Dynamics of periodic mechanical structures containing bistable elastic elements: From elastic to solitary wave propagation," *Physical Review E*, vol. 90, no. 2, p. 023204, 2014.

[115] B. Deng, P. Wang, V. Tournat, and K. Bertoldi, "Nonlinear transition waves in free-standing bistable chains," *Journal of the Mechanics and Physics of Solids*, vol. 136, p. 103661, 2020.

[116] N. Nadkarni, A. F. Arrieta, C. Chong, D. M. Kochmann, and C. Daraio, "Unidirectional transition waves in bistable lattices," *Physical review letters*, vol. 116, no. 24, p. 244501, 2016.

[117] D. Khatri, D. Ngo, and C. Daraio, "Highly nonlinear solitary waves in chains of cylindrical particles," *Granular Matter*, vol. 14, no. 1, pp. 63–69, 2012.

[118] C. Chong, M. A. Porter, P. G. Kevrekidis, and C. Daraio, "Nonlinear coherent structures in granular crystals," *Journal of Physics: Condensed Matter*, vol. 29, no. 41, p. 413003, 2017.

[119] F. Fraternali, G. Carpentieri, A. Amendola, R. E. Skelton, and V. F. Nesterenko, "Multiscale tunability of solitary wave dynamics in tensegrity metamaterials," *Applied Physics Letters*, vol. 105, no. 20, p. 201903, 2014.

[120] MATLAB, *version 9.7.0.1216025 (R2019b Update 1)*. Natick, Massachusetts: The MathWorks Inc., 2022.

[121] W. Zhang and J. Xu, "Quantitatively solitary wave tuning strategies based on one-dimensional cylindrical granular chains," *Extreme Mechanics Letters*, vol. 40, p. 100972, 2020.

[122] A. Molinari and C. Daraio, "Stationary shocks in periodic highly nonlinear granular chains," *Physical Review E*, vol. 80, no. 5, p. 056602, 2009.

[123] K. F. Graff, *Wave motion in elastic solids*. Courier Corporation, 2012.

[124] H. Kolsky, *Stress waves in solids*, vol. 1098. Courier Corporation, 1963.

[125] N. Prat, F. Rongieras, J.-C. Sarron, A. Miras, and E. Voiglio, "Contemporary body armor: technical data, injuries, and limits," *European journal of trauma and emergency surgery*, vol. 38, no. 2, pp. 95–105, 2012.

[126] S. R. Singiresu, *Mechanical vibrations*. Addison Wesley Boston, MA, 1995.